Novel Dual-band LTCC Bandpass Filters for Microwave Applications

by

Aref POURZADI

MANUSCRIPT-BASED THESIS PRESENTED TO ÉCOLE DE TECHNOLOGIE SUPÉRIEURE IN PARTIAL FULFILLMENT OF THE DEGREE OF DOCTOR OF PHILOSOPHY
Ph.D.

MONTREAL, "MARCH 29TH, 2020"

ÉCOLE DE TECHNOLOGIE SUPÉRIEURE
UNIVERSITÉ DU QUÉBEC

BOARD OF EXAMINERS

THIS THESIS HAS BEEN EVALUATED

BY THE FOLLOWING BOARD OF EXAMINERS

Prof. Ammar Kouki, Thesis Supervisor
Department of Electrical Engineering, École de technologie superieure

Prof. Nicole Demarquette, President of the Board of Examiners
Department of Mechanical Engineering, École de Technologie Superieure

Prof. Jean-Marc Lina, Member of the jury
Department of Electrical Engineering, École de Technologie Superieure

Prof. Tayeb A.Denidni, External Examiner
Énergie Matériaux Télécommunications Research Centre, Institut National de la Recherche Scientifique

THIS THESIS WAS PRESENTED AND DEFENDED

IN THE PRESENCE OF A BOARD OF EXAMINERS AND THE PUBLIC

ON "FEBRUARY 19^{TH}, 2020"

AT ÉCOLE DE TECHNOLOGIE SUPÉRIEURE

FOREWORD

This thesis is written as completion to Ph.D. in electrical engineering, at École de Technologie Superieure (ÉTS). Author worked on the subject since May 2014 to November 2019. The content is the original work of its author Aref Pourzadi.

ACKNOWLEDGEMENTS

I would like to take this opportunity expressing thank all people who have made this journey memorable.

First and foremost, I would like to express my sincere gratitude to my supervisior Prof. Ammar Kouki for giving me this opportunity. Not only for guiding and teaching me during my study, but also I appreciate him so much for all of his supports in my non-academic life.

Secondly, I would like to thank my Ph.D. committee members, Professors Nicole Demarquette, Jean-Marc Lina, and Tayeb A.Denidni for spending their time to read this thesis and giving me their valuable comments and feedbacks. Next, I am grateful to our technical staff, Normand Gravel, for the uncountable help he has given me on fabrication of my circuits and provided administrative and IT supports.

I also thank my friends and group members at LACIME laboratory: Hossein, Aaghaa Aria, Dorra, Hassan, Moustafa, Cina, Mohsen, Arash, . . . , for the technical discussions and creating such a friendly environment.

I would like to give a special thanks to my wife, Armin, for her endless support, patience and wonderful kindness. Finally, very big thank goes to my family and my brother, for their self-confidence boost and sending their loves from miles away.

FILTRES AVANCÉS À DEUX BANDES PASSANTES EN LTCC POUR LES APPLICATIONS MICRO-ONDES

Aref POURZADI

RÉSUMÉ

L'idée d'utiliser un seul système de communication sans fil pour plusieurs bandes de fréquence simultanément a orienté une partie des recherches sur la communication sans fil vers la conception de composants micro-ondes bi-bandes. Cette double fonctionnalité des composants entraîne une faible consommation d'énergie, une réduction de la taille du système et une diminution efficace des coûts. Cependant, des spécifications telles que le type de circuit, la plate-forme de mise en œuvre, la fréquence, les dimensions, les performances, etc. ont créé des défis sévères dans ce domaine.

Dans plusieurs systèmes de communication bi-bandes, l'un des composants les plus importants est le filtre passe-bande hyperfréquence (BPF : bandpass filters). Les réseaux de filtrage permettent aux signaux de passer entre deux fréquences spécifiques et de bloquer les signaux indésirables ou de les atténuer. Dans notre étude, nous nous concentrons sur la conception, la réalisation physique et la fabrication des filtres à deux bandes passantes de tailles très compactes en utilisant la technologie LTCC (Low Temperature Co-fired Ceramic). Parmi les stratégies normales pour fabrication des filtres, l'éléments localisés est utilisé afin d'avoir les circuits plus petits aux fréquences inférieures à 6 GHz. Dans différentes options pour réalisation l'éléments localisés, la technologie LTCC est fortement recommander grâce à la possibilité d'intégration des circuits avec réduction de la taille et des pertes par l'utilisation des diélectriques à faible perte en multicouches.

Dans un premier temps, nous présentons un nouveau schéma pour un filtre Chebyshev de deuxième ordre à deux bandes passantes en LTCC. En utilisant l'analyse en mode pair et impair, le mécanisme de travail du schéma est complètement décrit mathématiquement et une procédure de synthèse directe est présentée pour calculer les valeurs des éléments localisés correspondants aux fréquences centrales et la largeur de bande a été assignées. Cette procédure de conception s'appuie autant que possible sur les formules analytiques. La nature de la réponse en fréquence du circuit est établie par la combinaison de quatre pôles, quatre zéros et un séquençage spécifique entre eux. Quatre zéros de transmission sont générés pour bloquer les fréquences hors bande et rejeter les signaux parasites. Les limitations du schéma et de la procédure de conception proposés sont complètement discutées, et deux annexes sont fournies pour la procédure de démonstration des formules analytiques. Ensuite, la topologie et la technique de synthèse du filtre sont appliquées à la conception d'un filtre passe-bande à double bande (D-BPF : dualband bandpass filter) fonctionnant dans les bandes de fréquences 0.9 et 2.45 GHz industrielles, scientifiques et médicales (ISM) et fabriqué en technologie LTCC. Les résultats de mesure montrent un excellent accord entre la simulation électromagnétique (EM) et le prototype fabriqué.

En plus, un nouveau schéma d'un filtre à band étroite en LTCC contenant deux pôles et deux transmission zéro est présenter pour l'application band étroite industriel (SNBPF). La réponse fréquentielle de passe-bande est établi par les deux pôles et deux TZ sont désignés des deux côtés de la bande passante pour rejeter les signaux parasites. En raison de la symétrie du réseau, similaire à DBPF, l'analyse en mode pair et impair est utilisé afin d'expliqué le mécanisme de travail. En outre, une procédure de conception est fournie pour appliquer la nouvelle topologie à différentes fréquences du spectre. Puis, nous démontrons que le simple passe-bande est généralisé à une réponse en fréquence à double bande (DNBPF) en manipulant le schéma du filtre SNBPF. Le mécanisme de travail et la méthodologie de conception de DNBPF sont fournis. Pour valider la théorie des schémas proposés, deux exemples de conception sont synthétisés et prototypés en LTCC.

A la fin, nous proposons une technique rapide pour la réalisation de valeurs des éléments localisé dans une layout physique sur LTCC. En fonction du nombre d'éléments, des dimensions du circuit, du couplage mutuel et des effets parasites, le circuit nécessite des optimisations fastidieuses, et cette étape peut être très frustrante pour les concepteurs. Dans cette technique, en utilisation une stratégie de corrélation entre les simulateurs ADS (Advanced Design Simulator) et HFSS (High Frequency Structure Simulator), le temps de traitement de la réalisation physique est considérablement réduit en raison de l'élimination des étapes de réglage. L'utilité de cette technique est démontrée par le biais d'un D-BPF entièrement synthétisé.

Mots clés: filtre à deux bandes passantes, LTCC, éléments localisés, schéma de circuit, DNBPF, SNBPF, ADS, HFSS, masque physique, réalisation de circuit

NOVEL DUAL-BAND LTCC BANDPASS FILTERS FOR MICROWAVE APPLICATIONS

Aref POURZADI

ABSTRACT

The idea of using a single wireless communication system for multiple frequency bands simultaneously, has directed part of wireless communication researches towards the design of dual-band microwave components. This dual functionality of components bring low power consumption, system size reduction and more efficient in cost minimizing. Beside all of these advantages, specifications such as type of circuit, Implementation platform, frequency, dimension, performance and etc. have created stringent challenges in this field.

In many dual-band communication systems, one of the essential components is microwave dual-band bandpass filter (DBPF). Filtering networks allow signals to pass between two specific frequencies whereas block unwanted signals or make attenuation. In our study, we focus on design, physical realization and fabrication of very compact size of dual-band bandpass filters using low temperature co-fired ceramic technology (LTCC). Among commonly used strategies for building filters, lumped-elements are used to reach compact circuit size at frequencies less than 6 GHz. Out of different options for realizing lumped-elements, LTCC technology is highly recommended due to high circuit integration with size and loss reduction through the use of multilayer of low loss dielectrics.

Initially, we present a new schematic for dual-band LTCC second-order Chebyshev bandpass filter. Using even and odd mode analysis, working mechanism of the proposed schematic is fully analyzed mathematically and a direct synthesis procedure is presented to calculate the values of the schematic elements for given center frequencies and bandwidth. This design procedure leverages as much as possible, analytical formulas. The nature of the frequency response of the circuit is established by combination of four poles and four zeros and specific sequencing between them. Four transmission zeros are generated to clean out of band frequencies and reject spurious signals. The limitations on the proposed schematic and design procedure are completely discussed and two appendixes are provided for demonstration process of analytical formulas. Then, the filter topology and synthesis technique are applied for designing of a dual-band bandpass filter (D-BPF) operating in Industrial, scientific and medical (ISM) bands 0.9 and 2.45 GHz and fabricated in LTCC technology. The measurement results show an excellent agreement between the electromagnetic (EM) simulated and fabricated prototype.

Further, a new schematic of LTCC narrow bandpass filter containing two poles and two transmission zeros (TZs) is presented for industrial narrowband applications (SNBPF). The bandpass frequency response is established by the two poles, and two TZs are appointed in the both sides of passband to reject spurious signals. Due to symmetry of the network, similar to D-BPF, even and mode analysis is used to explain working mechanism. Also, a design procedure is provided to apply the new topology in different frequencies of spectrum. Then, we demonstrate that the single bandpass is generalized to a dual-band frequency response (DNBPF) by

manipulating the schematic of SNBPF filter. The working mechanism and design procedure of the DNBPF are provided. To validate the theory of proposed schematics, two design examples are synthesized and prototyped in LTCC.

Finally, we propose a fast technique for realization of lumped-elemet values into 3D physical layout on LTCC. Depending on number of elements, physical dimension, mutual coupling and parasitic effects, the circuits require time consuming optimizations and this stage can be very frustrating for designers. In this technique, using correlation strategy between simulators Advanced Design Simulators (ADS) and High frequency structure simulator (HFSS), processing time of physical realization is reduced significantly because of elimination of tuning steps. The usefulness of this technique is demonstrated through a fully synthesized D-BPF.

Keywords: Dual-band bandpass filter, LTCC, lumped-elements, circuit schematic, DNBPF, SNBPF, ADS, HFSS, Physical layout, Circuit realization

TABLE OF CONTENTS

Page

LIST OF TABLES

LIST OF FIGURES

LIST OF ABREVIATIONS

BPF	Bandpass filter
3D	Three dimentional
LTCC	Low temperature co-fired ceramic technology
D-BPF	Dual-band bandpass filter
SNBPF	Single narrow bandpass filter
DNBPF	Dual narrow bandpass filter
EM	Electromagnetic
ISM	Industrial, scientific and medical
ADS	Advanced Design Simulators
HFSS	High frequency structure simulator
WLAN	wireless local area network
GSM	global system mobile communications
WIMAX	worldwide interoperability for microwave access
RF	Radio frequency
HTC	High temperature superconductor
SRF	Self-resonance frequency
LACIME	Laboratoire de Communications et d'Intgration de la Microlectronique
MMIC	Monolothic Microwave Integrated Circuit
MCM	Multichip modules
Tz	transmission zero

LISTE OF SYMBOLS AND UNITS OF MEASUREMENTS

f_z^e	even zero frequency
f_z^o	odd zero frequency
f_p^e	even pole frequency
f_p^o	odd pole frequency
f_c	center frequencies
BW	bandwidths
RL	return losses
K	coupling coefficient
ω	angular frequency
Q	quality factor
FBW	fractional bandwidth
Q_e	external quality factor
T	group delay
f_z	transmission zero frequency

INTRODUCTION

In recent years, advances in wireless communication systems have continued at a high pace with increasing use of the electromagnetic spectrum. For example, fifth generation (5G) wireless systems will use new frequencies in addition to the legacy ones of the fourth generation (4G) and Long Term Evolution (LTE) systems. Concurrently, wireless devices offer more and more applications that rely on wireless communications thereby increasing data rates and spectrum usage. As these technologies continue to evolve, the need for covering multiple frequency bands in a single device is bound to continue to increase. Already, current wireless devices support wireless local area networks (WLAN) at multiple frequencies, multiple 4G/LTE frequencies, legacy global system mobile communications (GSM) frequencies, worldwide interoperability for microwave access (WiMax) bands, and other industrial, scientific and medical (ISM) bands for near field communication (NFC) and wireless charging. To efficiently accommodate such a wide range of frequencies, high performance dual-band and multi-band microwave devices are needed.

The term dual-band refers to microwave devices that are able to operate simultaneously at two separate frequencies. This approach leads to: (i) increased circuit integration, (ii) size reduction, (iii) cost minimization and (iv) reduced power consumption for wireless systems. As filters are critical microwave components for wireless devices, Dual-band Bandpass filters (D-BPFs) are key enablers for dual-band wireless communication systems. D-BPFs allow two different modulated signals to be extracted simultaneously from other undesired signals and interferers by attenuating out-of-band signals thereby improving the system's signal to noise ratio (SNR). Currently, D-BPFs are the subject of intense and continued research where issues such as improving selectivity, decreasing size, accommodating wide/narrow fractional bandwidths and operating frequency selection are being investigated.

Depending on the target application and the desired performance, D-BPFs can be realized using different topologies and technologies including waveguide, microstrip and other planar structures and lumped-elements. The choice of a given filter fabrication technology is dictated by the desired filtering characteristics as well as size and cost constraints. The key filtering characteristics are center frequency, bandwidth, Q-factor, in-band insertion loss and out-of-band rejection. Conventional waveguide D-BPFs have the lowest insertion loss and offer better power handling. However due to their bulkiness and poor integration capability with other circuit blocks, they are generally not suited for most portable systems particularly those operating at frequencies less than 6 GHz. Compared to waveguide D-BPFs, planar microstrip structures have the advantage of smaller size and easy integration, although they show higher insertion loss and lower power handling capability. Despite being less bulky than waveguides, distributed microstrip filters can still be quite large, particularly at lower frequencies, and may be impractical for many portable mobile devices.

Lumped-elements, which are passive components having all their dimensions smaller than operating wavelength, offer yet another option for filter realization with the possibility of designing very compact size D-BPFs for a wide range of microwave applications. In terms of insertion loss and power handling, lumped elements filters offer similar performance to distributed microstrip ones. It should be noted however that for higher frequencies, the realization lumped-elements becomes more and more difficult because of the required fabrication tolerances and techniques as well as the limitation imposed by the element's self-resonance frequency (SRF). Lumped element D-BPFs can be realized on-chip of off-chip. On-chip realization uses lumped-elements built on the semiconductor substrate and offer the smallest filter size that can be achieved. However, these substrates tend to have relatively high loss which leads to low Q-factor for the elements and, hence limiting the achievable filter performance. Additionally, on-chip lumped element inductors tend to occupy large chip areas, which increases cost. Off-chip lumped element realization can overcome the low Q limitation of the

on-chip technology but with typically larger size components. To achieve both high Q and small size in off-chip lumped element implementations, the use of 3D circuit fabrication technologies, such as Low Temperature Co-fired Ceramic (LTCC), is considered as one of the most viable options.

LTCC is a suitable technology for developing miniaturized advanced filters for applications where low loss, small size, easy integration, temperature stability and high relative permittivity are required. A typical LTCC module consist of several dielectric tapes, or layers, connected by vias and on which good or resistive conductors are printed as well as very high dielectric constant pastes. Resistors, inductors and capacitors can therefore be fabricated using this technology by combining buried and/or surface structures.

Problem Statement

As has been discussed above, D-BPFs handle signal selections in two different frequency passbands concurrently. In this thesis, we seek to address the lack of design methodology that (i) allow for the arbitrary selection of filters' passbands, (ii) achieve the highest size reduction possible and (iii) provide the best out-of-band rejection. Additionally, the sought design methodology must be able to cover both narrow and wideband applications. Finally, we will investigate techniques to address the problem of the lengthy simulation time faced when the physical realization phase of D-BPFs is undertaken by transitioning from circuit representation to 3D structures and using electromagnetic field simulation.

Research Objectives

The overall objective of this research work is to develop an efficient end-to-end solution for the accurate and rapid design and physical realization of compact lumped element D-BPFs

with selectable center frequencies and bandwidths. To reach this objective, the following sub-objectives will be pursued:

- Develop novel, wide, and narrowband lumped circuit element topologies that offer dual band behavior and which can be analytically analyzed.
- Develop design procedures that use the proposed topologies of D-BPFs to synthesize of the filter's elements based on the desired center frequencies, controllable fractional bandwidths (FBW), and placement of transmission zeros.
- Develop an efficient technique to translate a lumped element filter's circuit design into and LTCC physical layouts in the shortest possible.

Methodology

Our methodology is built on the following three main steps with additional sub-steps or iterations as needed:

a. **Designs and simulations:** First, novel lumped-element networks generating concurrent dual-band frequency responses are investigated. The circuit topologies and the working mechanisms are analyzed analytically and through circuit simulation. Second, based on the analytical results, direct design and synthesis procedures are developed to calculate the lumped-elements values for given filtering characteristics. Third, the developed design processes are applied to the practical design of DBPFs for selected applications at the circuit level using Matlab and Advanced Design Systems (ADS). Fourth, the circuit designs are translated into physical layouts in the form of 3D LTCC structures and electromagnetic field simulations are performed to finalize the designs using ANSYS HFSS software.

b. **Fabrication:** The obtained simulation results are validated by fabricating the designed physical layouts on LTCC dielectrics. Several green tapes are prepared and then via punch-

ing and conductors are printed on each tape. In the last stage, all LTCC sheets are stacked under water pressure and the final layout is fired in the oven for 24 hours.

c. **Test and validation:** The fabricated D-BPFs are tested using a vector network analyzer and the measured S-parameters are compared to those obtained by 3D field simulation.

Content and contribution

The remainder of the thesis is presented in the paper-based format of ÉTS dissertation. Thus, each chapter presents one journal paper, which embodies the contributions made. The literature review and the state of the art relevant to each aspect of the research work are included in the introduction of each paper.

- Chapter 1 presents a novel topology of a DPBF as well as a new design methodology design methodology that allows to directly synthesize the filter elements' values based on the desired specification. Both of these contributions are demonstrated and validated through the implementation of compact dual-band LTCC second order Chebyshev bandpass filters. The related paper has been published in the IEEE Transactions on Microwave Theory and Techniques Journal Pourzadi *et al.* (2019).

- Chapter 2 presents a the generalization of the direct synthesis technique to cover both single- and dual- narrow band- pass filters in LTCC. The related paper submitted to IEEE Transactions on Circuits and Systems I: Regular Papers Journal.

- Chapter 3 presents a fast technique for the realization of lumped-element circuit components of given values through 3D LTCC structures that shortens the required 3D electromagnetic field simulation time. The related paper is submitted to IEEE Transactions on Components, Packaging and Manufacturing Technology Journal.

- Chapter 4 summarizes the main contributions presented in this thesis and gives recommendations and suggestions for future work.

CHAPTER 1

DESIGN OF COMPACT DUAL-BAND LTCC SECOND ORDER CHEBYSHEV BANDPASS FILTERS USING A DIRECT SYNTHESIS APPROACH

Aref Pourzadi[1], Aria Isapour[1], Ammar Kouki[1]

[1] Département de Génie Électrique, École de Technologie Supérieure,
1100 Notre-Dame Ouest, Montréal, Québec, Canada H3C 1K3

Manuscript accepted to IEEE Transactions on Microwave Theory and Techniques in March 2019.

Abstract

A new lumped element circuit model suitable for dual-band bandpass filter (D-BPF) response is proposed. Using even/odd mode analysis, analytical equations are developed and used for the development of a direct synthesis design procedure. The proposed procedure is applied to the design and realization of a D-BPF prototype in LTCC technology covering two ISM bands of 0.9 and 2.45 GHz. This filter has been successfully measured with an insertion loss of less than 2 dB, return loss better than 18 dB for both bands and out of band attenuation higher than 20 dB.

Introduction

Most current wireless devices that support more than one frequency band do so using multiple single-band microwave components. This leads to increased part-count, cost and size which can be addressed through dual-band, and eventually multi-band structures. Over the last couple of decades, an important research effort has been deployed towards the development of dual-band microwave devices using different types of resonators Miyake *et al.* (1997); Liu *et al.* (2010); Rezaee & Attari (2014); Avrillon *et al.* (2003); Zheng *et al.* (2014); Mousavi & Kouki (2014); Schindler & Tajima (1989); Cao *et al.* (2014); Liu *et al.* (2015). The three commonly used strategies for building resonators include: cavities Liu *et al.* (2010);

Rezaee & Attari (2014), distributed coupled-line or split ring resonators in planar microstrip technology Avrillon *et al.* (2003); Zheng *et al.* (2014) and lumped-elements in Monolothic Microwave Integrated Circuit (MMIC) or Low Temperature Co-fired Ceramic (LTCC) technologies Mousavi & Kouki (2014); Schindler & Tajima (1989). At lower frequencies, the major drawback of cativities and distributed microstrip printed structures is their relatively large size which limits integration and circuit size reduction. Lumped element resonators offer significantly smaller size become a desirable option at these frequencies and can be the solution of choice if their losses can be minimized. Out of the two options for realizing lumped elements, MMIC and LTCC, the latter is more attractive. Indeed, LTCC technology offers the potential for high circuit integration with size and loss reduction through the use of multi-layers of low-loss dielectrics and high conductivity metals such as silver and gold Imanaka (2005).

Several works have been reported (D-BPFs) in LTCC technology, see for example Chen *et al.* (2009); Wang *et al.* (2013); Chin *et al.* (2010); Dai *et al.* (2013); Oshima *et al.* (2010); Zhou *et al.* (2011); Tang *et al.* (2006); Tang & You (2006); Lin *et al.* (2006); Joshi & Chappell (2006); TAMURA *et al.* (2010). All of these works report compact 3D D-BPFs with various degrees of performance and size reduction. Out of these, the D-BPFs in Chen *et al.* (2009); Wang *et al.* (2013) are designed based on cavity structures, not lumped LC elements, and are therefore limited to very high frequencies, such as mm-wave frequencies. In Chin *et al.* (2010); Dai *et al.* (2013) the desired filter response cannot be precisely specified due to the lack of a suitable theoretical methodology with closed-form expressions. In Oshima *et al.* (2010); Zhou *et al.* (2011) the design techniques proposed and used are suitable for ultra-wideband applications and cannot be readily applied to narrow BPFs. In Tang *et al.* (2006); Tang & You (2006); Lin *et al.* (2006); Joshi & Chappell (2006); TAMURA *et al.* (2010) the limited number of out of band transmission zeros leads to poor rejection of spurious signals. In Lin *et al.* (2014); Xu *et al.* (2016c), out of band transmission zeros are added however the design procedure leads to have high capacitance and inductance values in some cases, which in turn results in fabrication challenges as well as reduced self-resonance frequency (SRF).

In this paper, we propose a new D-BPF based on a lumped-element network containing four poles and four zeros. We show, through an even/odd mode analysis of the proposed network, that this network has an intrinsic dual-band frequency response. We also propose a synthesis technique that uses closed-form expressions to control the placement of poles and zeros, and therefore control the dual band response of the network. The resulting synthesis procedure yields an initial D-BPF filter design that is finalized through minor turning. By adding a parallel capacitor, the configuration of D-BPF is modified for improving the out of band rejection. The use of the proposed synthesis technique and modified configuration is illustrated through the design of a 3D D-BPF with four transmission zeros covering two ISM bands.

The rest of this paper is organized as follows: Section 1.1 introduces the main core of proposed D-BPF and describes its working mechanism. Section 1.2 presents the design process and details the synthesis technique for calculating circuit element values for a D-BPF. Section 1.3 illustrates the use of the proposed network in the design of a prototype of D-BPF. Section 1.4 presents the modified configuration of proposed D-BPF with improved stopband rejection. Simulation and fabrication results are described in section 1.5. Concluding remarks are presented in Section 1.6.

1.1 Proposed Network and Working Mechanism

Fig. 1.1 shows the schematic of the proposed D-BPF which consists of five major sections: (i) a pair of shunt LC resonators $[C_1, L_1]$, (ii) inductive coupling between this pair of parallel resonators $[Lm_1]$, (iii) a pair of series LC resonators $[C_2, L_2]$, (iv) inductive coupling between this pair of series resonators $[Lm_2]$ and (v) coupling capacitors $[C_c]$. According to network theory Jia Sheng Hong (1996), the complex schematic in Fig. 1.1 can be simplified to the alternative form shown in Fig. 1.2. The properties of both configurations are the same however the second, because of symmetry, is more convenient for even/odd mode analysis. Under even/odd excitations, Fig. 1.2 can be decomposed into two hybrid resonators (Fig. 1.3. a, b) Yang *et al.* (2010); Tamura *et al.* (2011) which have the same circuit topology but different inductance values.

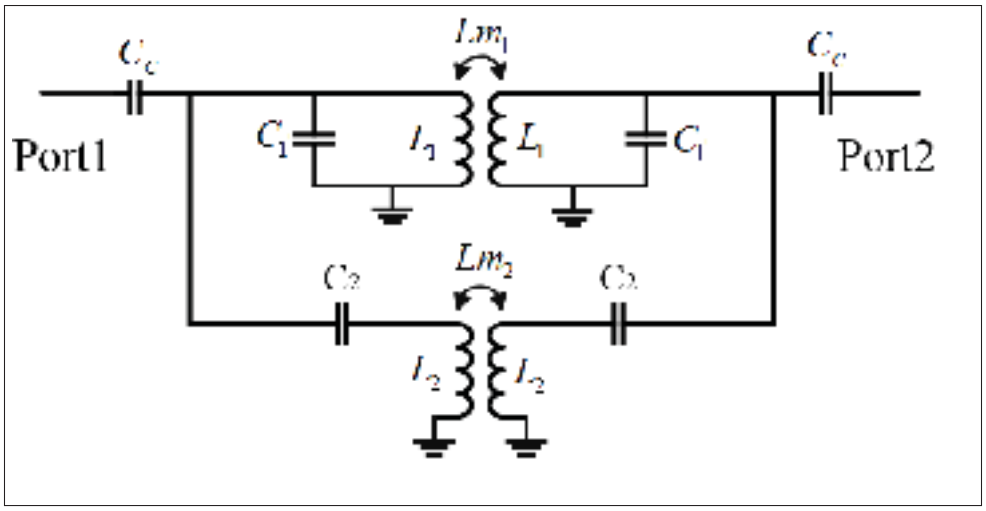

Figure 1.1 Schematic of the proposed D-BPF

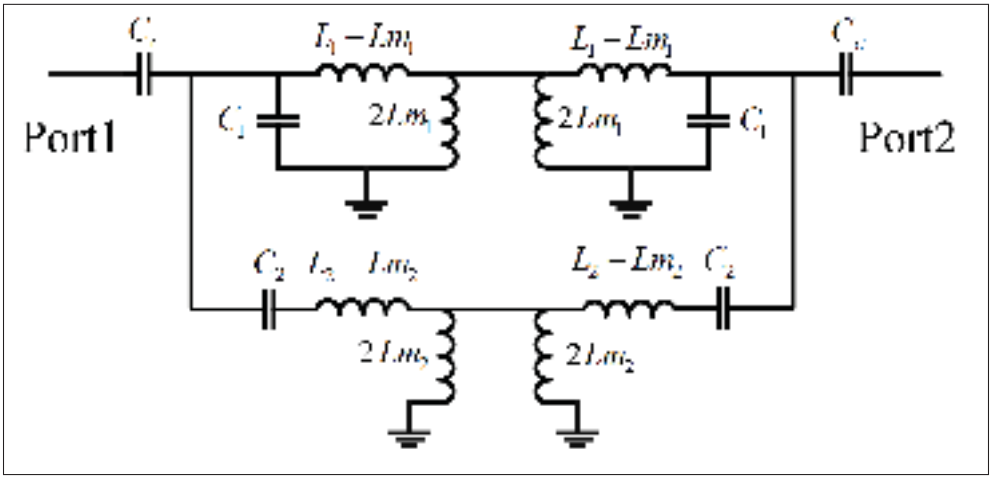

Figure 1.2 An alternative form of the proposed D-BPF

Calculating the input admittance under odd excitation, i.e., the circuit of Fig. 1.3.a, gives:

$$Y_{in}^{o} = \frac{j\omega C_C[\omega^4 X^o - \omega^2 Y^o + 1]}{\omega^4[X^o + C_C C_2 L_1^o L_2^o] - \omega^2[Y^o + C_C L_1^o] + 1} \tag{1.1}$$

Where $X^o = C_1 C_2 L_1^o L_2^o$, $Y^o = C_2 L_2^o + C_1 L_1^o + C_2 L_1^o$, $L_2^o = L_2 - Lm_2$ and $L_1^o = L_1 - Lm_1$. Equating (1.1) to zero reveals the existence of four zeros and four poles among which only the two

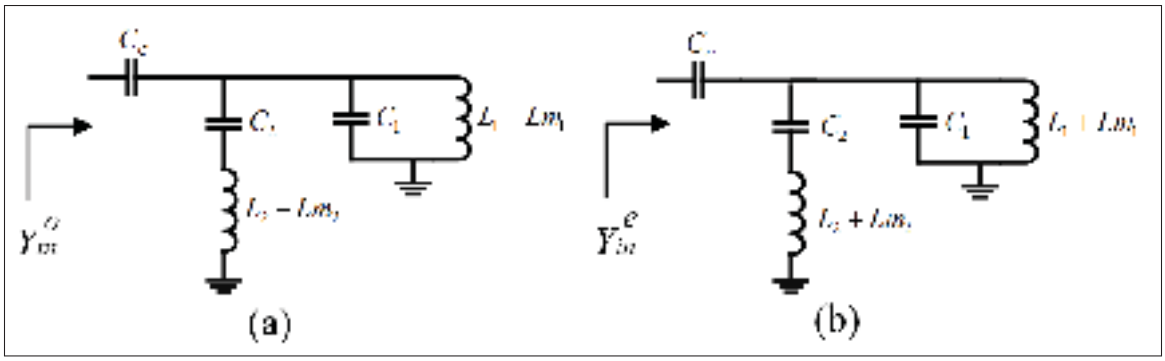

Figure 1.3 a) Odd mode circuit model, and b) even mode circuit model

positive zeros and two positive poles are of interest and will be considered. The zeros, $\omega^o_{z,+}$, $\omega^o_{z,-}$, are given by (1.2), while the two poles are given by (1.3) $\omega^o_{p,+}$, $\omega^o_{p,-}$, below of this page.

The subscripts 'z' and 'p' indicate zeros and poles respectively, and '+' and '-' refer to the sign inside the square roots in (1.2) and (1.3). Repeating the above analysis under even excitation, i.e., the circuit of Fig. 1.3.b, the input admittance is found to be:

$$\begin{cases} \omega^o_{z,+} = 2\pi f^o_{z,+} = \sqrt{\dfrac{C_2L_2^o+C_1L_1^o+C_2L_1^o+\sqrt{(C_2L_2^o+C_1L_1^o+C_2L_1^o)^2-4C_1C_2L_1^oL_2^o}}{2C_1C_2L_1^oL_2^o}} \\ \omega^o_{z,-} = 2\pi f^o_{z,-} = \sqrt{\dfrac{C_2L_2^o+C_1L_1^o+C_2L_1^o-\sqrt{(C_2L_2^o+C_1L_1^o+C_2L_1^o)^2-4C_1C_2L_1^oL_2^o}}{2C_1C_2L_1^oL_2^o}} \end{cases} \tag{1.2}$$

$$\begin{cases} \omega^o_{p,+} = 2\pi f^o_{p,+} = \sqrt{\dfrac{C_2L_2^o+(C_1+C_C)L_1^o+C_2L_1^o+\sqrt{(C_2L_2^o+(C_1+C_C)L_1^o+C_2L_1^o)^2-4(C_1+C_C)C_2L_1^oL_2^o}}{2(C_1+C_C)C_2L_1^oL_2^o}} \\ \omega^o_{p,-} = 2\pi f^o_{p,-} = \sqrt{\dfrac{C_2L_2^o+(C_1+C_C)L_1^o+C_2L_1^o-\sqrt{(C_2L_2^o+(C_1+C_C)L_1^o+C_2L_1^o)^2-4(C_1+C_C)C_2L_1^oL_2^o}}{2(C_1+C_C)C_2L_1^oL_2^o}} \end{cases} \tag{1.3}$$

where $X^e = C_1C_2L_1^eL_2^e$, $Y^e = C_2L_2^e + C_1L_1^e + C_2L_1^e$, $L_2^e = L_2 + Lm_2$, and $L_1^e = L_1 + Lm_1$. Similarly, (1.4) has four zeros and four poles among which the positive zeros and the positive poles are of

interest. The zeros, $\omega^e_{z,+}$, $\omega^e_{z,+}$, are given by (1.5), while the two poles are given by (1.6) $\omega^e_{p,+}$, $\omega^e_{p,+}$.

$$Y^e_{in} = \frac{j\omega C_C[\omega^4 X^e - \omega^2 Y^e + 1]}{\omega^4[X^e + C_C C_2 L^e_1 L^e_2] - \omega^2[Y^e + C_C L^e_1] + 1} \tag{1.4}$$

$$\begin{cases} \omega^e_{z,+} = 2\pi f^e_{z,+} = \sqrt{\frac{C_2L^e_2+C_1L^e_1+C_2L^e_1+\sqrt{(C_2L^e_2+C_1L^e_1+C_2L^e_1)^2-4C_1C_2L^e_1L^e_2}}{2C_1C_2L^e_1L^e_2}} \\ \omega^e_{z,-} = 2\pi f^e_{z,-} = \sqrt{\frac{C_2L^e_2+C_1L^e_1+C_2L^e_1-\sqrt{(C_2L^e_2+C_1L^e_1+C_2L^e_1)^2-4C_1C_2L^e_1L^e_2}}{2C_1C_2L^e_1L^e_2}} \end{cases} \tag{1.5}$$

$$\begin{cases} \omega^e_{p,+} = 2\pi f^e_{p,+} = \sqrt{\frac{C_2L^e_2+(C_1+C_C)L^e_1+C_2L^e_1+\sqrt{(C_2L^e_2+(C_1+C_C)L^e_1+C_2L^e_1)^2-4(C_1+C_C)C_2L^e_1L^e_2}}{2(C_1+C_C)C_2L^e_1L^e_2}} \\ \omega^e_{p,-} = 2\pi f^e_{p,-} = \sqrt{\frac{C_2L^e_2+(C_1+C_C)L^e_1+C_2L^e_1-\sqrt{(C_2L^e_2+(C_1+C_C)L^e_1+C_2L^e_1)^2-4(C_1+C_C)C_2L^e_1L^e_2}}{2(C_1+C_C)C_2L^e_1L^e_2}} \end{cases} \tag{1.6}$$

In total, we have four zero frequencies, $f^e_{z,-}$, $f^o_{z,-}$, $f^e_{z,+}$, and $f^o_{z,+}$, and four pole frequencies, $f^e_{p,-}$, $f^o_{p,-}$, $f^e_{p,+}$, and $f^o_{p,+}$. These frequencies will determine the nature of the frequency response of the circuit of Fig. 1.2 depending on their sequencing and the spacing between them. The exact order of these frequencies will be determined by the various element values of the circuit. Mathematically, this means that here exist 8! possible sequences for these frequencies. However, irrespective of element values, we prove in Appendix A that the following conditions must always hold:$f^o_{p,-} < f^o_{z,-} < f^o_{p,+} < f^o_{z,+}$, $f^e_{p,-} < f^e_{z,-} < f^e_{p,+} < f^e_{z,+}$, $f^e_{p,-} < f^o_{p,-}$, $f^e_{p,+} < f^o_{p,+}$, $f^e_{z,-} < f^o_{z,-}$, and $f^e_{z,+} < f^o_{z,+}$. Consequently, the number of different possible sequences reduces to only 576 states. Furthermore, by excluding those sequences that poles are placed between zeros, only one leads to a frequency response suitable for D-BPF application which is:

$$f^e_{p,-} < f^o_{p,-} < f^e_{z,-} < f^o_{z,-} < f^e_{p,+} < f^o_{p,+} < f^e_{z,+} < f^o_{z,+} \tag{1.7}$$

Fig.1.4 shows, the admittance curves are plotted by typical element values to show how the selected sequence creates a dual-band response. As illustrated in this figure, the bandwidth and frequency ratios of the proposed D-BPF can be independently controlled by proper selection of the pairs of frequency zeros, namely, $(f^e_{z,-}, f^o_{z,-})$, and $(f^e_{z,+}, f^o_{z,+})$, provided with realizable lumped element values. The return loss level can be independently controlled for only one of the two passbands. In the next section a design procedure is proposed to explain how each of these four zero frequencies can be positioned independently which leads to a dual-band bandpass filter with the desired frequency response.

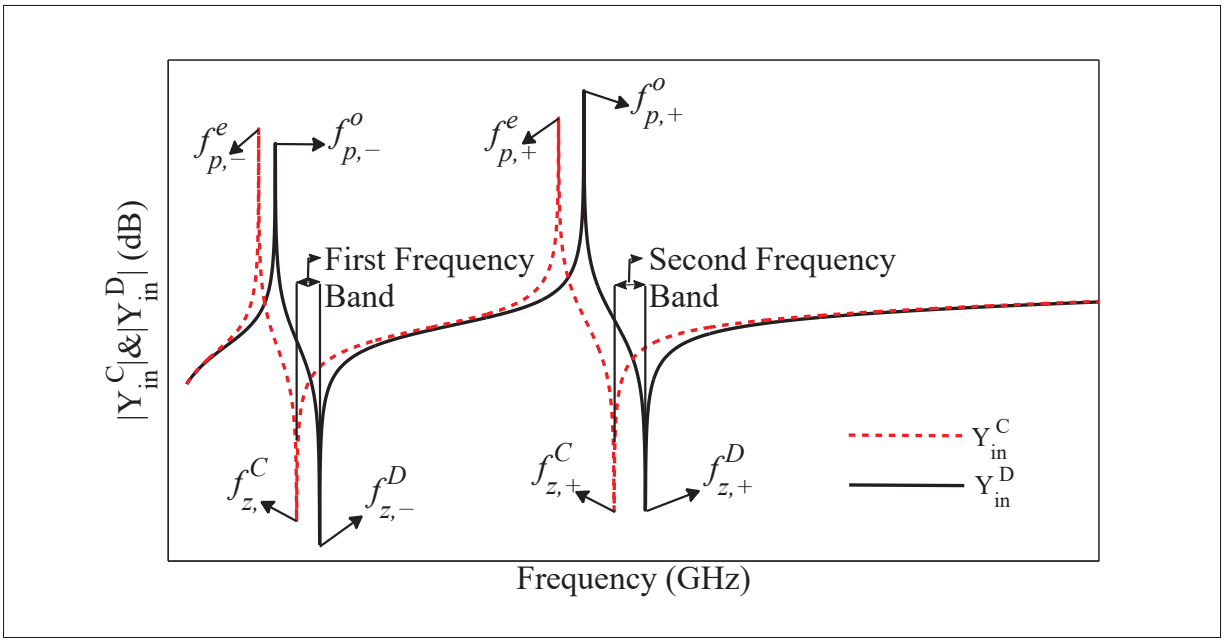

Figure 1.4 Illustrates typical admittance curves versus frequency for the selected sequence and shows clearly the placement of poles and zeros

1.2 D-BPF Synthesis Procedure

With the topology fixed and the proper frequency sequence identified, we now proceed with the synthesis procedure. The design procedure contains three steps consisting of finding the zero frequencies, the pole frequencies and the elements values as follows.

a. In the first step, the frequencies of the four zeros $f^e_{z,-}$, $f^o_{z,-}$, $f^e_{z,+}$, and$f^o_{z,+}$ are calculated based on the chebyshev response which is outlined in Dancila & Huynen (2011). We start with the assigned center frequencies(f_{c1}, f_{c2}), the desired bandwidths (BW_1, BW_2) and in-band return losses (RL_1, RL_2). Since only one of the retun loss levels can be independently set to the desired value, in this case RL_1, an initial value is assigned to RL_2 and it is final value is dependent on RL_1. f_{C1} and f_{C2} can be approximated by averaging the zero frequencies as

$$f_{C1} \approx \frac{f^e_{z,-} + f^o_{z,-}}{2} \tag{1.8}$$

$$f_{C2} \approx \frac{f^e_{z,+} + f^o_{z,+}}{2} \tag{1.9}$$

and the coupling coefficients are calculated by the following equations

$$K_1 \approx \frac{(f^o_{z,-})^2 - (f^e_{z,-})^2}{(f^o_{z,-})^2 + (f^e_{z,-})^2} \tag{1.10}$$

$$K_2 \approx \frac{(f^o_{z,+})^2 - (f^e_{z,+})^2}{(f^o_{z,+})^2 + (f^e_{z,+})^2} \tag{1.11}$$

where K_i is corresponded to BW_i , fc_i and g elements, see (1.12) Dancila & Huynen (2011):

$$K_i = \frac{BW_i}{f_{ci}} \sqrt{\frac{1}{g_1 g_2}} \tag{1.12}$$

i indicate number of passbands. Using a nonlinear optimization technique for solving (1.10) and (1.11) subject to the constraints of (1.8) and (1.9) leads to the optimal values of $f^e_{z,-}$, $f^o_{z,-}$, $f^e_{z,+}$, and $f^o_{z,+}$.

b. In the second step, the frequencies of the four poles $f^e_{p,-}$, $f^o_{p,-}$, $f^e_{p,+}$, $f^o_{p,+}$ are calculated. Using the obtained zero frequencies in the first step, we generate a set of additional equations as detailed in Appendix B where the even pole frequencies $f^e_{p,-}$ and $f^e_{p,+}$ can be

determined in terms of zero frequencies and the two odd pole frequencies $f^o_{p,-}$ and $f^o_{p,+}$. Therefore, $f^o_{p,-}$ and $f^o_{p,+}$ constitute degrees of freedom in our synthesis procedure.

The selection of $f^o_{p,-}$ and $f^o_{p,+}$, must respect $f^o_{p,-} < f^e_{z,-}$ and $f^o_{z,-} < f^o_{p,+} < f^e_{z,+}$ in order to satisfy (1.7). By choosing $f^o_{p,-}$ and $f^o_{p,+}$, the terms $\gamma, (\omega^o_s)^2, (\omega^o_h)^2, (\omega^o_R)^2$ and Ω are calculated from equations (1.13)-(1.17), respectively:

$$\gamma = \frac{(\omega^o_{z,+}\omega^o_{z,-})^2}{(\omega^o_{p,+}\omega^o_{p,-})^2} - 1 \tag{1.13}$$

$$(\omega^o_s)^2 = \frac{T}{\gamma} \tag{1.14}$$

where

$$T = (1+\gamma)[(\omega^o_{p,+})^2 + (\omega^o_{p,-})^2] - (\omega^o_{z,+})^2 - (\omega^o_{z,-})^2$$

$$(\omega^o_h)^2 = \frac{(\omega^o_{z,+}\omega^o_{z,-})^2}{(\omega^o_s)^2} \tag{1.15}$$

$$(\omega^o_R)^2 = (\omega^o_{z,+})^2 + (\omega^o_{z,-})^2 - (\omega^o_h)^2 - (\omega^o_s)^2 \tag{1.16}$$

$$\psi = \frac{(\omega^o_s)^2}{(\omega^o_R)^2} \tag{1.17}$$

The value of ω^e_s is obtained by solving the below fourth order equation as demonstrated in Appendix B:

$$(1+\psi)(\omega^e_s)^4 - \psi[(\omega^e_{z,+})^2 + (\omega^e_{z,-})^2](\omega^e_s)^2 + \psi(\omega^e_{z,+}\omega^e_{z,-})^2 = 0 \tag{1.18}$$

Among the four roots of (1.18) we retain only the real positive root that satisfies the following condition:

$$\frac{f^o_s}{f^e_s} < \frac{f^o_{z,+}f^o_{z,-}}{f^e_{z,+}f^e_{z,-}} \tag{1.19}$$

If no solution to (1.18) that satisfied (1.19) is found, another set of $f^o_{p,-}$ and $f^o_{p,+}$ values must be chosen and equations (1.13)-(1.19) re-solved. As long as condition (1.19) is

satisfied, we can have many set of acceptable values for $f^o_{p,-}$ and $f^o_{p,+}$. However, each pair of selected $f^o_{p,-}$ and $f^o_{p,+}$ leads to different values for the D-BPF elements. Once a suitable value for ω^e_s is found, we solve for ω^e_h and ω^e_R :

$$(\omega^e_h)^2 = \frac{(\omega^e_{z,+}\omega^e_{z,-})^2}{(\omega^e_s)^2} \tag{1.20}$$

$$(\omega^e_R)^2 = (\omega^e_{z,+})^2 + (\omega^e_{z,-})^2 - (\omega^e_h)^2 - (\omega^e_s)^2 \tag{1.21}$$

and we compute $f^o_{p,+}$ and $f^o_{p,-}$ using (1.22) and (1.23).

$$\omega^e_{p,+} = 2\pi f^e_{p,+} = \sqrt{\frac{((\omega^e_h)^2 + (1+\gamma)(\omega^e_s)^2 + (\omega^e_R)^2) + \sqrt{((\omega^e_h)^2 + (1+\gamma)(\omega^e_s)^2 + (\omega^e_R)^2)^2 - 4(1+\gamma)(\omega^e_h\omega^e_s)^2}}{2(1+\gamma)}} \tag{1.22}$$

$$\omega^e_{p,-} = 2\pi f^e_{p,-} = \sqrt{\frac{(\omega^{e^2}_h + (1+\gamma)\omega^{e^2}_s + \omega^{e^2}_R) - \sqrt{(\omega^{e^2}_h + (1+\gamma)\omega^{e^2}_s + \omega^{e^2}_R)^2 - 4(1+\gamma)\omega^{e^2}_h\omega^{e^2}_s}}{2(1+\gamma)}} \tag{1.23}$$

c. Once the values of all pole and zero frequencies are computed, the third step is to compute the values of the lumped-elements. We show in Appendix B the details of how this can be carried out. Starting with $C_1 = C_2\psi$ (1.66) and given that ψ has been computed by (1.17) either C_1 or C_2 can be used as a third degree of freedom, in addition to $f^o_{p,+}$ and $f^o_{p,-}$. The choice of the C_1 or C_2 should be made according to fabrication technology in terms of realizable capacitance values, i.e., maximum value with proper SRF.

With C_1 or C_2 chosen, the remaining parameters, C_c, L_1, Lm, L_2, and Lm_2 are computed using equations (1.24) to (1.28), respectively.

$$C_C = C_1\gamma \tag{1.24}$$

$$L_1 = \frac{1}{2C_1}\left[\frac{1}{(\omega_h^e)^2} + \frac{1}{(\omega_h^o)^2}\right] \tag{1.25}$$

$$Lm_1 = \frac{1}{2C_1}\left[\frac{1}{(\omega_h^e)^2} - \frac{1}{(\omega_h^o)^2}\right] \tag{1.26}$$

$$L_2 = \frac{1}{2C_2}\left[\frac{1}{(\omega_s^e)^2} + \frac{1}{(\omega_s^o)^2}\right] \tag{1.27}$$

$$Lm_2 = \frac{1}{2C_2}\left[\frac{1}{(\omega_s^e)^2} - \frac{1}{(\omega_s^o)^2}\right] \tag{1.28}$$

The frequency response of synthesized network can now be calculated using the obtained element values and (1.29)-(1.30):

$$S_{11} = S_{22} = \frac{Y_0^2 - Y_{in}^e Y_{in}^o}{(Y_{in}^e + Y_0)(Y_{in}^o + Y_0)} \tag{1.29}$$

$$S_{21} = S_{12} = \frac{Y_0(Y_{in}^o - Y_{in}^e)}{(Y_{in}^e + Y_0)(Y_{in}^o + Y_0)} \tag{1.30}$$

The above detailed synthesis steps of the D-BPF design are summarized in Fig. 1.5 in the form of a chart. It is worth noting the following limitations on the proposed design procedure:

a. The use of lumped elements constrains the D-BPF design to frequencies less than the lowest SRF of the inductors and capacitors.

b. The feasibility of the D-BPF design depends on the realizability of the lumped element values in the technology chosen. This becomes more important for wider spacing between the passbands.

c. The two passbands can be adjusted with close spacing if the calculated values of $f_{p,-}^e$ and $f_{p,+}^e$ meet (1.7).

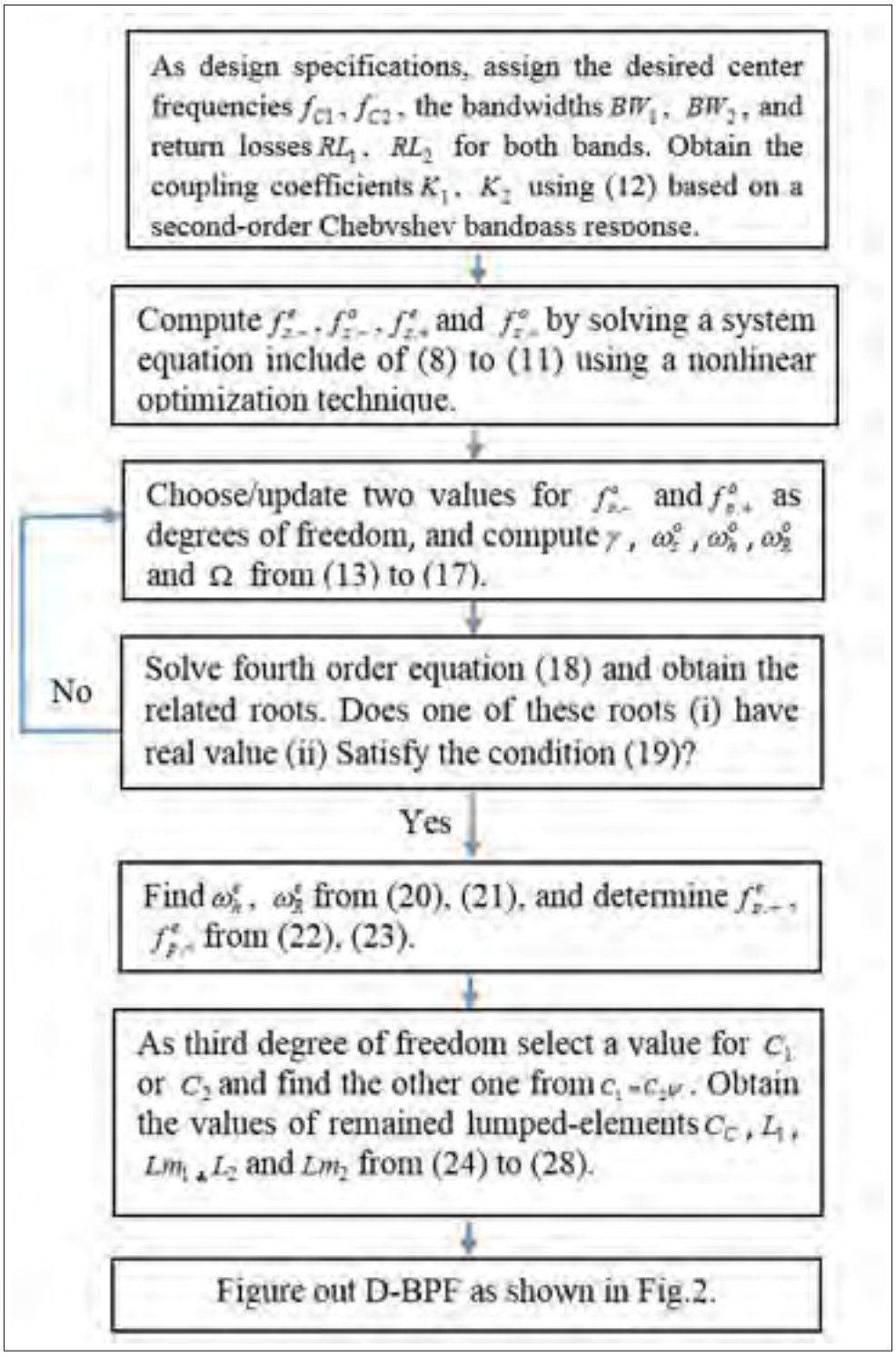

Figure 1.5 Chart of synthesis steps for D-BPF

1.3 D-BPF Design

This section illustrates the application of the proposed synthesis procedure to the design and prototyping of a dual-band second order Chebyshev ISM bandpass filter operating at 890 - 940 MHz and 2.38 - 2.52 GHz. Other design examples, not proptotyped are also given to illustrate the use of the proposed technique. Following the steps outlined above we proceed as follows:

a. Based on the desired frequency bands, we have $f_{c1} = 915$ MHz, $f_{c2} = 2450$ MHz, $BW_1 = 50$ MHz, and $BW_2 = 140$ MHz.

   In addition, by requiring a return loss of 20dB at both bands, the filter's g_i elements are found to be: $g_0 = 1$, $g_1 = 0.6923$, $g_2 = 0.5585$ and $g_3 = 1.2396$. Using these obtained values in (1.12), we find $K_1 = 0.0879$ and $K_1 = 0.0919$.

   Next, equations (1.8)-(1.11) are used in a nonlinear optimization algorithm in Matlab to compute the values of zero frequencies, which are found to be: $f^e_{z,-} = 0.875$ GHz, $f^e_{z,-} = 0.955$ GHz, $f^e_{z,+} = 2.337$ GHz and $f^e_{z,+} = 2.563$ GHz.

b. The second step consists of finding the four pole frequencies. As degrees of freedom, $f^o_{p,-}$ and $f^o_{p,+}$ are selected to be 0.8749 GHz and 2.336 GHz, which respect the conditions $f^o_{p,-} < f^e_{z,-}$ and $f^o_{z,-} < f^o_{p,+} < f^e_{z,+}$. Then, using equations (1.13)-(1.17) and solving the fourth order equation (1.18), we obtain two roots: $\omega^e_s = 10.43$ rad/s and $\omega^e_s = 5.919$ rad/s. Of these two solutions, only $\omega^e_s = 10.43$ rad/s satisfies (1.19). Using (1.20)-(1.21) we compute ω^e_h and ω^e_R which are then used in (1.22) and (1.23) to compute the two remaining poles, namely $f^e_{p,-} = 0.801$ GHz and $f^e_{p,+} = 2.129$ GHz.

c. The third step consists of computing the values of all lumped elements of the filter. As the third degree of freedom, we need to select a value for C_2 . The selection of this value should take into account the fabrication process and its limitations. Additionally, it should ensure a sufficiently high SRF frequency for the targeted design. Based on these considerations and our LTCC process characteristics, we chose the value of C_2 to be 1.8 pF. Based on (B-16), $C_1 = C_2\psi$, and the value of ψ from (1.17), C_1 is found to be 2.54 pF.

The values of the remaining elements are calculated from (1.24)-(1.28) and yield: $C_c = 1.1037$ pF, $L_1 = 6.051$ nH, $Lm_1 = 0.52$ nH, $L_2 = 4.66$ nH, and $Lm_2 = 0.434$ nH.

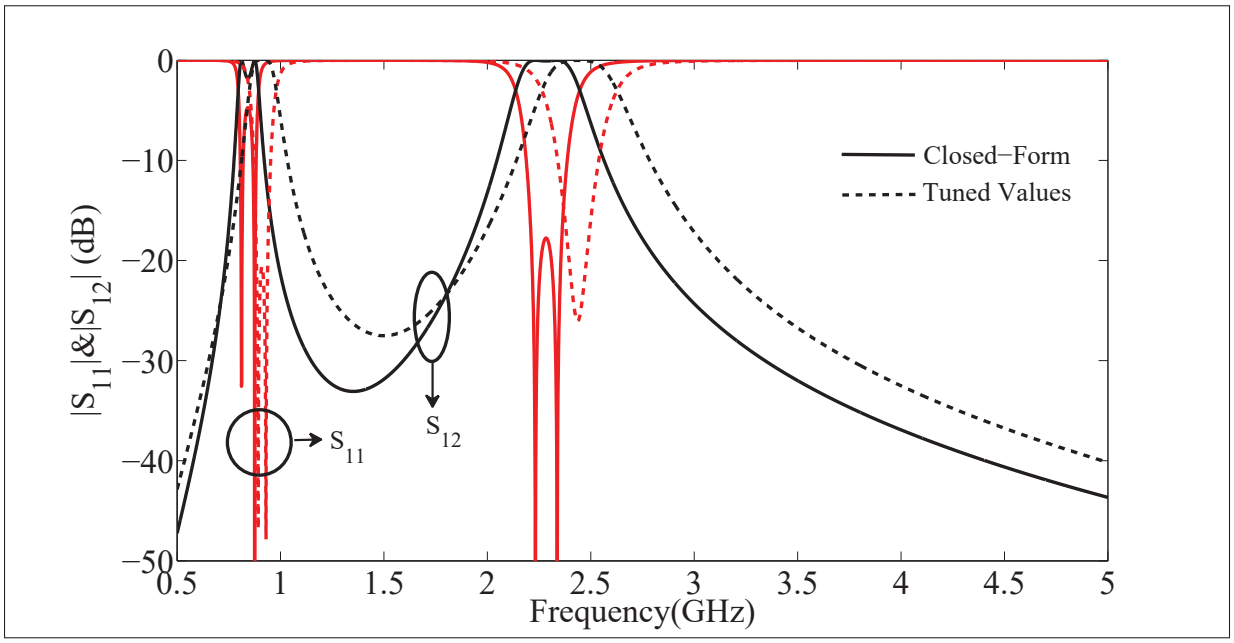

Figure 1.6 Simulated S-parameters of D-BPF, solid line: Closed-Form and dashed line: Tuned values

With the obtained element values, we can compute the frequency response using (1.29)-(1.30). Fig. 1.6 shows the computed frequency response of the synthesized D-BPF in solid lines. As can be seen, the center frequencies are slightly shifted from the desired values and the return loss is not as expected. These are due to the approximations in equations (1.8)-(1.11) and can be easily corrected with a slight tuning of the element values as shown in dashed lines in Fig. 1.6. Table 1.1 lists the original and tuned values of the filter elements.

Repeating the above procedure, two additional designs have been carried out with one for closely spaced passbands and one for widely spaced passbands. The specifications, element values and frequency responses of the both filters are shown in Table 1.2, Fig. 1.7 and Fig. 1.8, respectively.

Table 1.1 Comparison Between for the D-BPF Prototype

Network parameters	Closed-Form	Tuned values
C_2 (pF)	1.8	1.5
C_1 (pF)	2.54	2.51
L_1 (nH)	6.051	5.33
L_2 (nH)	4.66	4.56
Lm_1 (nH)	0.52	0.52
Lm_2 (nH)	0.434	0.454
C_c (pF)	1.1037	1.53

Table 1.2 Design Examples

Design Examples	1		2	
Specification	f_{c1} 2 GHz	f_{c2} 3 GHz	f_{c1} 0.5 GHz	f_{c2} 8 GHz
	FBW_1 0.1	FBW_2 0.03	FBW_1 0.07	FBW_2 0.04
	RL_1 30 dB	RL_2 17 dB	RL_1 30 dB	RL_2 15 dB
Tuned Values	C_2 0.6 pF	Lm_1 0.154 nH	C_2 3.8 pF	Lm_1 0.74 nH
	C_1 6.25 pF	Lm_2 0.176 nH	C_1 5.16 pF	Lm_2 0.028 nH
	L_1 0.8 nH	C_c 7.62 pF	L_1 3.61 nH	C_c 4.54 pF
	$L_2 = 5.71$ nH		$L_2 = 0.47$ nH	

1.4 Modified Configuration of the Proposed D-BPF

As can be seen from Fig. 1.6, the out of band rejection of the filter may not sufficient for some applications. In the order to improve this, we propose to add a parallel capacitor, C_z, to the designed filter as suggested in Yeung & Wu (2003) and shown in Fig. 1.9. By creating a feedback path, this capacitor generates four transmission zeros as can be understood from the new admittance matrix:

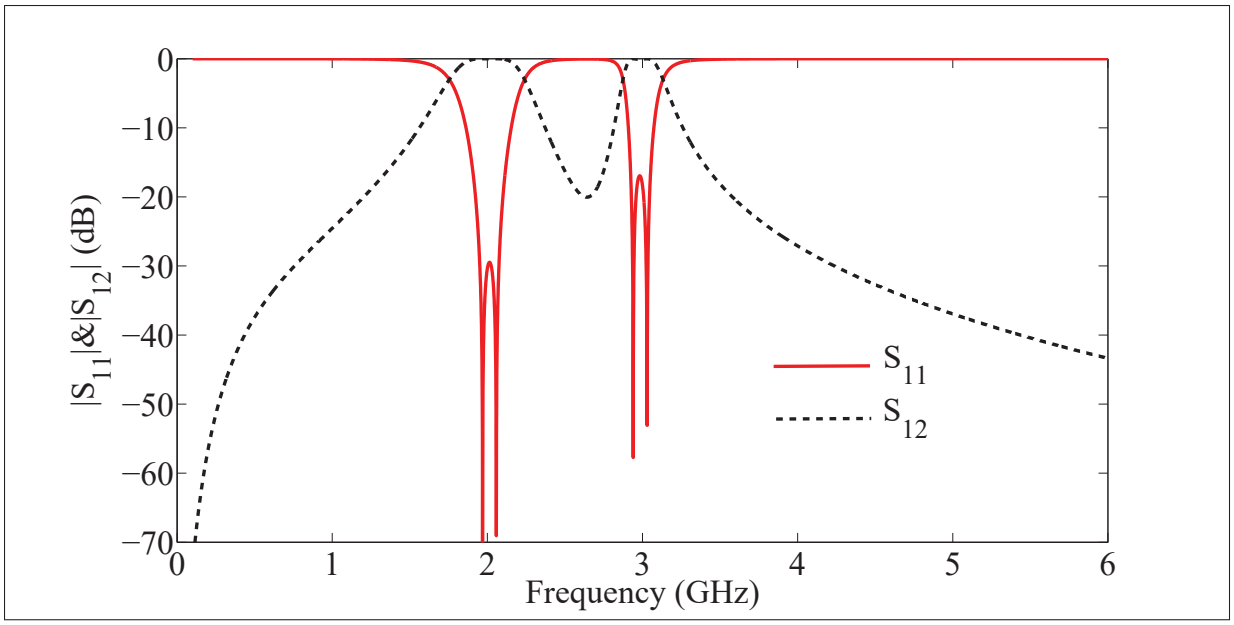

Figure 1.7 Simulated S-parameter of the design example 1

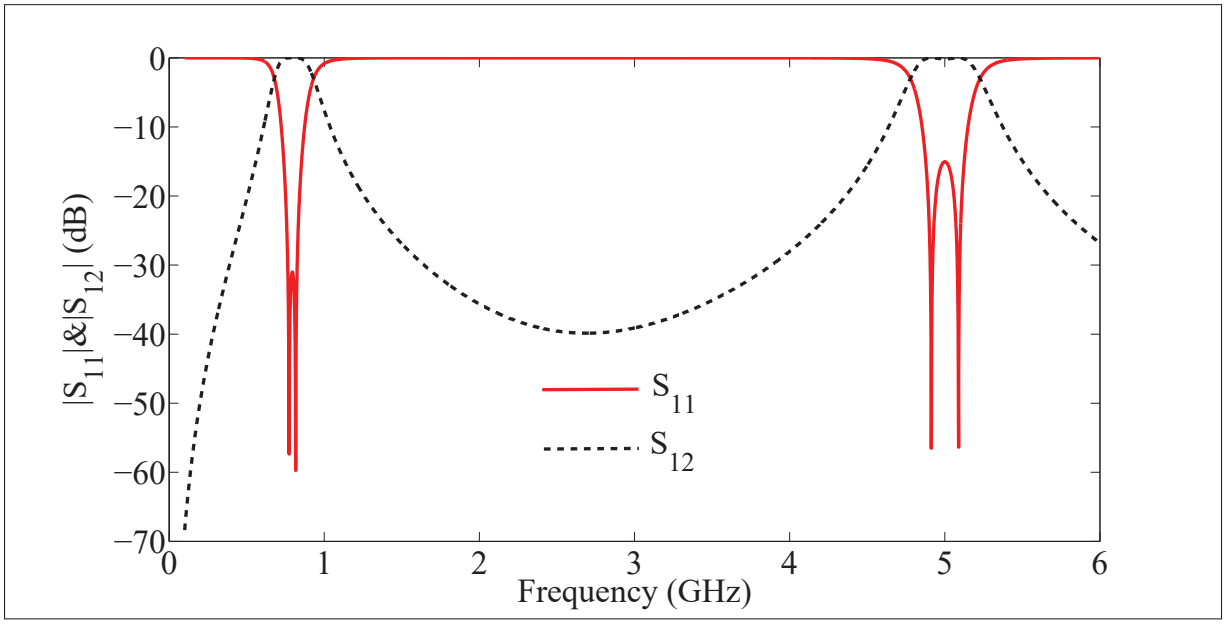

Figure 1.8 Simulated S-parameter of the design example 2

$$[Y] = \begin{pmatrix} j\omega C_Z + y_{11} & -j\omega C_Z + y_{12} \\ -j\omega C_Z + y_{21} & j\omega C_Z + y_{22} \end{pmatrix} \tag{1.31}$$

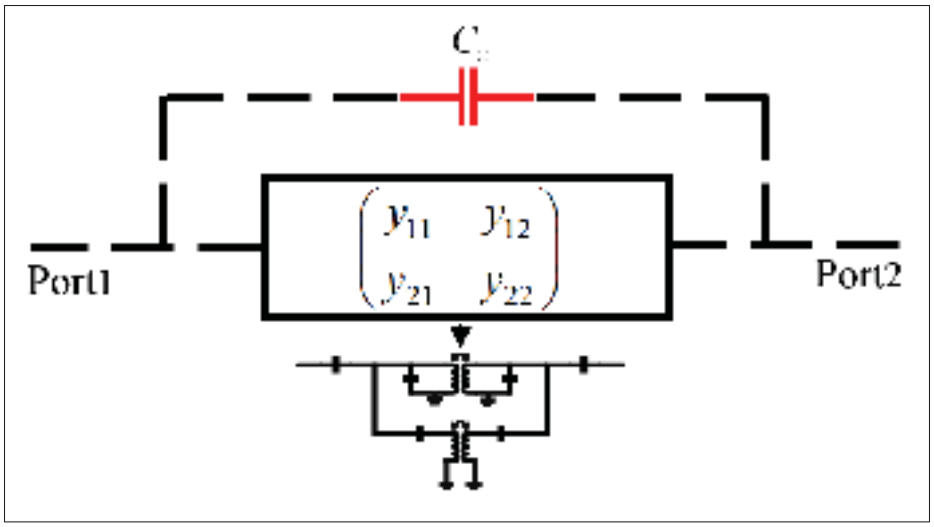

Figure 1.9 Schematic of modified D-BPF with four transmission zeros

where y_{11}, y_{12}, y_{21}, and y_{22} are the elements of admittance matrix for the tuned D-BPF as designed in the previous section. The location of transmission zeros can be obtained by solving $|y_{12}| = \omega C_Z$ graphically as shown in Fig. 1.10. The intersection points of $|y_{12}|$ curve and the straight line of ωC_Z determine the frequencies of the transmission zeros, which can be controlled by changing the value of C_Z. Using the values of the tuned filter in Table 1.1 and the procedure of Fig. 1.10, we chose $C_Z = 0.2$ pF. Fig. 1.11 shows the simulated S-parameters of the modified D-BPF showing good out of band rejection.

1.5 Electromagnetic Simulation and Fabrication Results

The realization of the synthesized D-BPF requires that the circuit model be transformed into a physical layout for the targeted fabrication technology. In this work, we use 5 layers of Dupont 9K7 LTCC with dielectric constant of 7.1 and a loss tangent of 0.001. Given the capacitance and inductance values needed, we chose to implement capacitors using multi-layer parallel plates and inductors using spirals on LTCC. The mutual inductances, (Lm_1, Lm_2), can be realized using power exchange between individual inductors Brzezina & Roy (2014) by proximity effect as represented in Fig. 1.1. This approach is viable for low coupling (low mutual inductance). Alternatively, mutual inductances can be realized using physical inductors

as represented in Fig. 1.2. This approach is more appropriate for higher coupling and larger bandwidths. It is this latter approach that we opted for in our design.

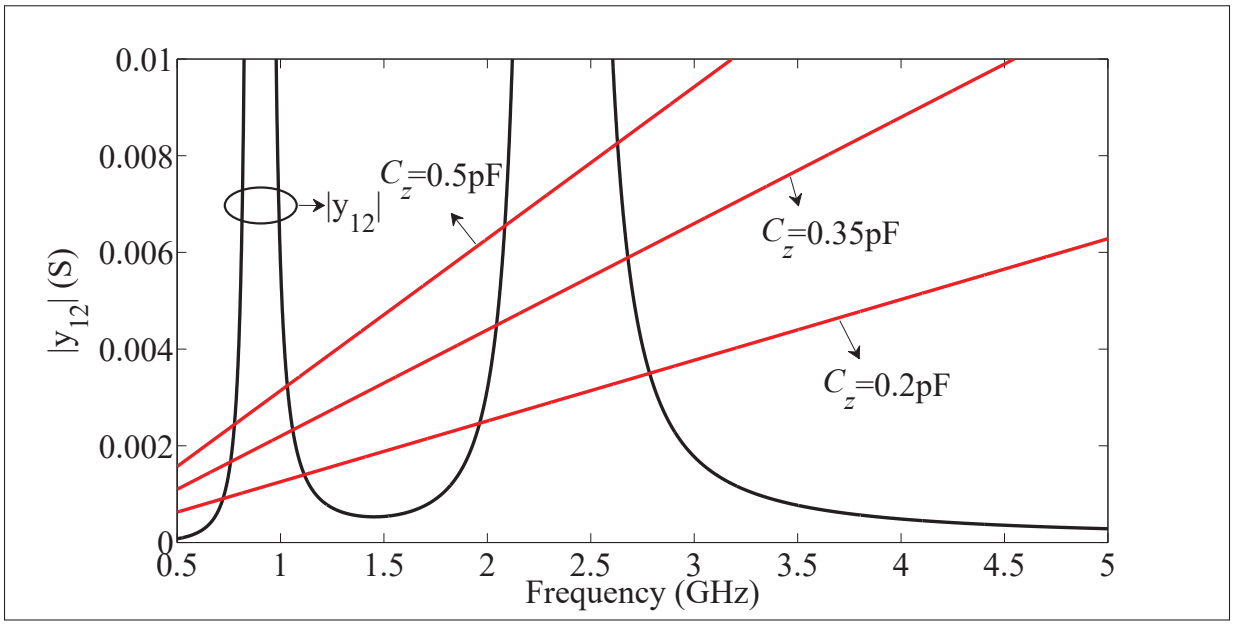

Figure 1.10 Plot of intersection between $|y_{12}|$ and the straight lines of ωC_Z

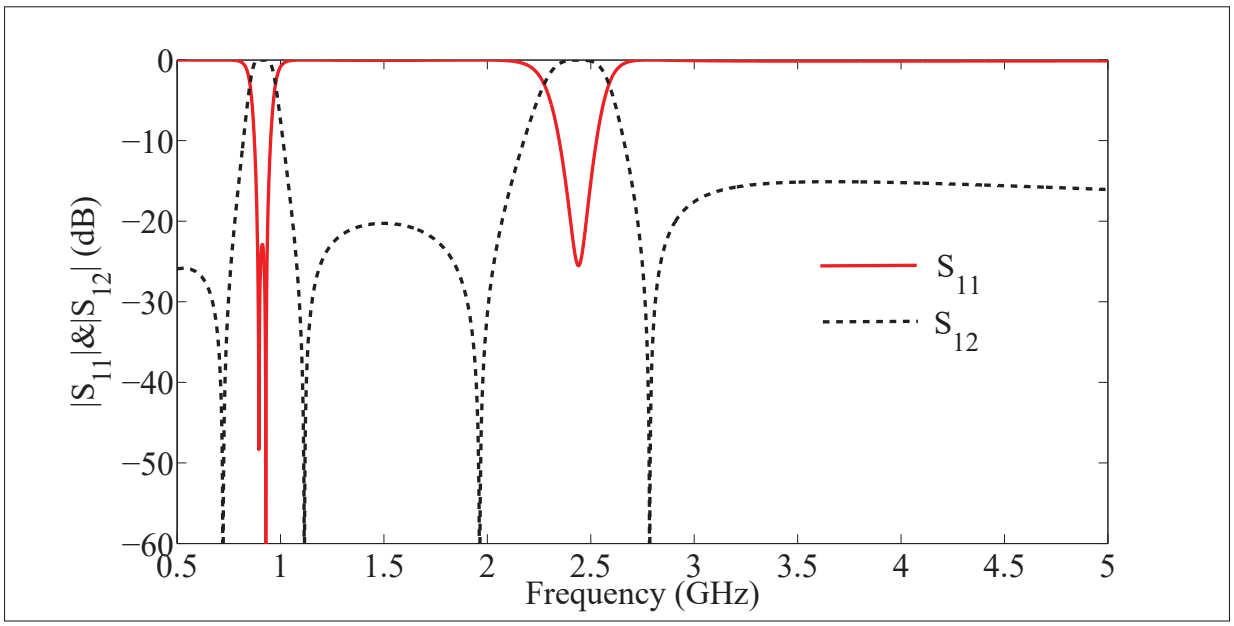

Figure 1.11 Simulated S-parameter of modified D-BPF circuit model with $C_Z = 0.2$ pF

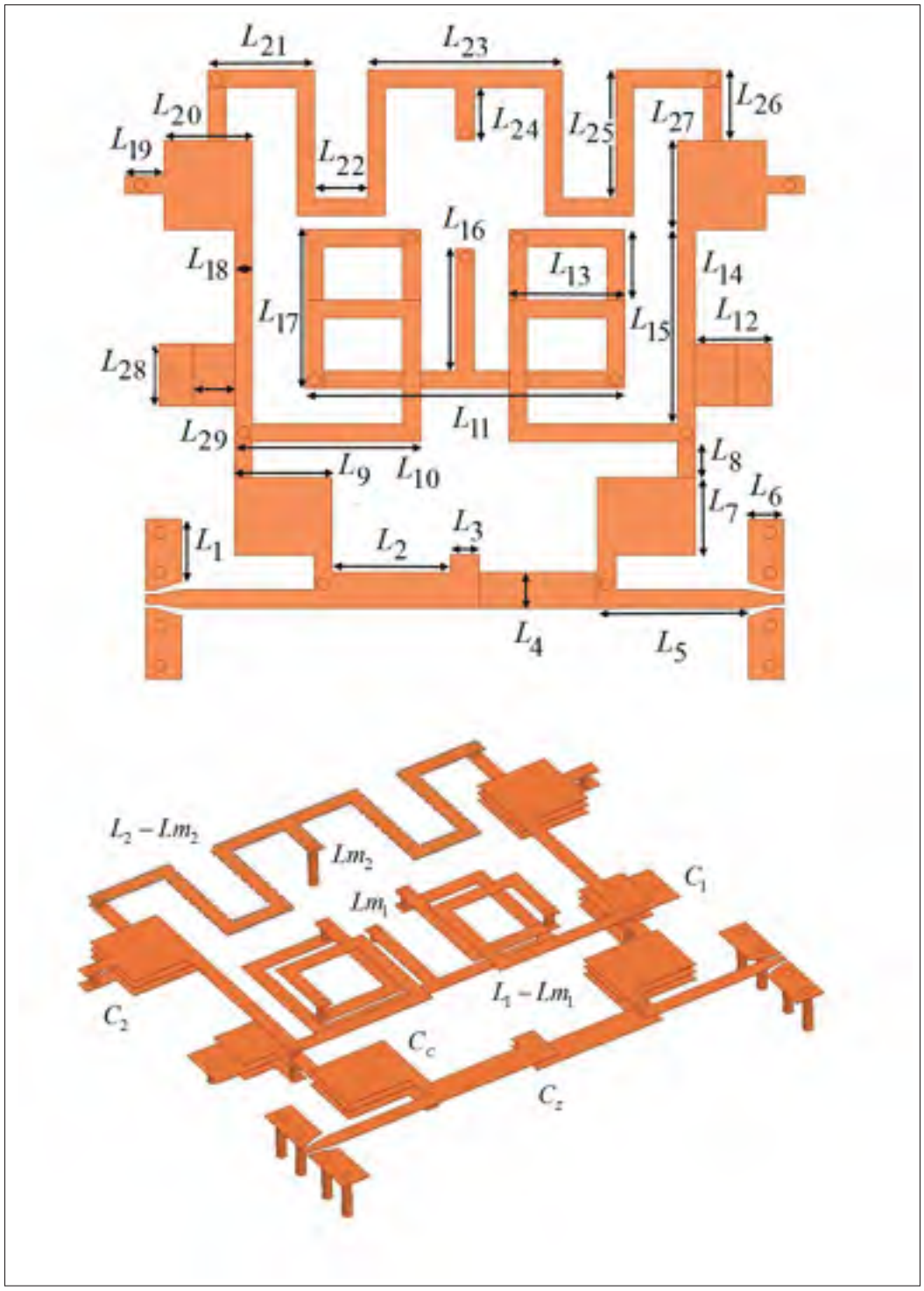

Figure 1.12 3D configuration and geometric parameters of modified D-BPF. Dimensions are all in millimeter L_1=0.7, L_2=1.34, L_3=0.33, L_4=0.4, L_5=1.5, L_6=0.4, L_7=0.88, L_8=0.6, L_9=1.1, L_{10}=2.1, L_{11}=3.6, L_{12}=1.06, L_{13}=1.3, L_{14}=2.4, L_{15}=0.8, L_{16}=1.38, L_{17}=1.4, L_{18}=0.2, L_{19}=0.4, L_{20}=1, L_{21}=1.2, L_{22}=0.6, L_{23}=2.2, L_{24}=0.6, L_{25}=1.45, L_{26}=0.8, L_{27}=1, L_{28}=0.7, L_{29}=0.66

Using the 3D field simulator HFSS, we synthesize the various elements following the technique outlined in Brzezina (2009) and then interconnect them to form the entire filter. An optimization of the overall dimension is then carried in simulation to obtain the final filter layout as shown in Fig. 1.12. This filter was fabricated using 8 µm thick silver and silver filled 136 µm diameter vias and 5 layers of green tape. Fig. 1.13 illustrates the fabricated circuit. The final dimensions of the fired filter are $7.2 \times 6.88 \times 0.56$ mm^3 with a total fired thickness of 0.56 mm.

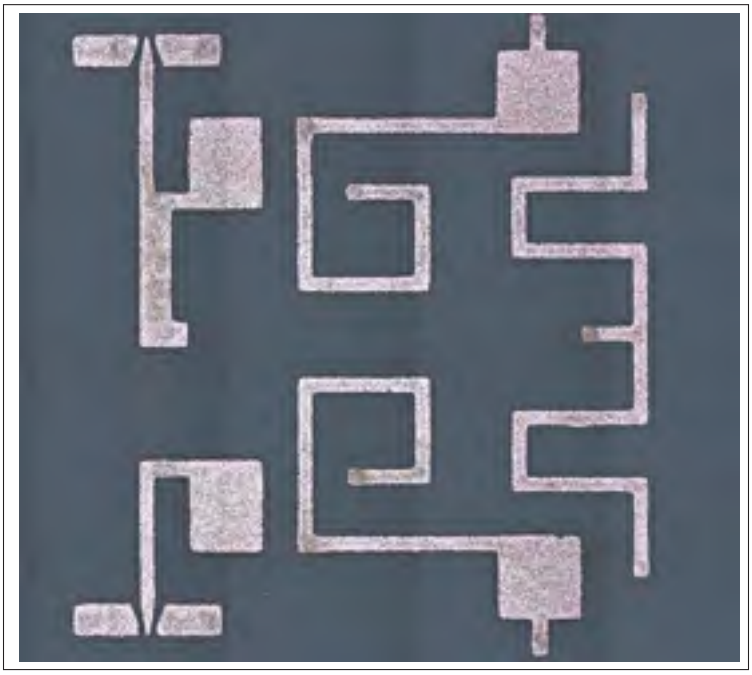

Figure 1.13 Photo of fabricated LTCC D-BPF

Fig. 1.14, shows the EM-simulated and measured S-parameters of the designed LTCC D-BPF. Excellent agreement is found between the two. The measured in-band insertion loss is less than 2 dB, for the first band, and less than 1.5 dB, for the second band. The measured return loss is better than 18 dB, for the first band, and better than 22 dB, for the second band. The fact the filter show slightly better performance at the upper band is a result of the designed lumped elements having their maximum Q-factor at the upper band frequencies. Finally, the measurements show that the four transmission zeros are located at 0.72, 1.1, 1.9 and 2.92 GHz.

Table 1.3 Performance Comparison of the Proposed Filter with Similar Published Designs

Ref	f_{c1}/f_{c2} (GHz)	RL_1/RL_2 (dB)	IL_1/IL_2 (dB)	FBW_1/FBW_2 (%)	No. of TZ	No. of elements	Closed-Form Equation	Highest Value of Elements	Structure
Miyake *et al.* (1997)	0.9/1.9	min:10	max: 2	—	2	—	No	—	Lumped-elements
Chen *et al.* (2009)	2.4/5.8	min:15	max: 3	52/18	1	—	No	—	Stepped-impedance stub
Wang *et al.* (2013)	2.45/5.2	13/20	2.2/1.2	9.8/11.9	4	—	No	—	Stepped-impedance stub
Dai *et al.* (2013)	4.02/8.2	min:16	max: 3	55/58	4	—	No	—	Coupled-resonator
Oshima *et al.* (2010)	2.5/5.27	14/14	1.4/1.8	16/10.4	3	—	Yes	—	Coupled-resonator
Zhou *et al.* (2011)	2.47/5.2	13/13	1.5/2.1	13.7/8.71	3	—	Yes	—	Coupled-resonator
Tang & You (2006)	2.4/5.22	20/16	1.4/1.1	17.5/20	3	13	Yes	10.3 nH	Lumped-elements
Lin *et al.* (2006)	2.45/5.2	12/16.8	2/2.3	12.2/5.7	4	15	Yes	6.22 pF	Lumped-elements
Joshi & Chappell (2006)	0.92/1.6	16/15.5	0.7/1.25	22.2/11.8	6	15	Yes	22.5 nH	Lumped-elements
Kapitanova *et al.* (2009)	2/3	min:18	2.3/3.6	7.5/5	1	25	Yes	—	Lumped-distributed TL
Yatsenko *et al.* (2007)	2.4/5	17/10	1.5/1.2	—	2	13	No	—	Lumped-elements
Turgaliev *et al.* (2013)	2.35/5.4	12/13	2.5/1.4	5/12.84	0	—	No	—	Cavity-CSRR
V. Turgaliev & Hein (2015)	0.746/1.793	17/16	1.4/2.1	13.4/9.5	2	—	No	—	Capacitively loaded cavity
This Work	0.9/2.45	18/22	2/1.5	5.46/5.71	4	13	Yes	5.33 nH	Lumped-elements

As it is known, physical inductors and capacitors do not operate like ideal elements at frequencies higher than their SRF. Therefore, the SRF of the D-BPF elements will determine the bandwidth of the upper stopband. Additionally, parasitic coupling due to tight integration may also impact the upper stopband.

Finally, table 1.3 including comparison performance of dual-band LTCC filters is provided.

1.6 Conclusion

In this paper, a novel second order lumped-element D-BPF was proposed, designed, fabricated and tested. The proposed filter topology provides four poles and four zeros whose sequence and placement were explained. A design procedure using closed-form equations to calculate the values of the network element for desired center frequencies and bandwidth was presented. The addition of a parallel capacitor to the original filter topology was used to increase the out of band rejection by generating four transmission zeros in the frequency response. The proposed filter topology and synthesis technique were applied to the design of a D-BPF for the two ISM bands, 0.9 and 2.45 GHz in LTCC technology. A prototype of this filter was successfully simulated and measured with excellent agreement between simulation and measurement. Other implementations based on the same circuit topology can be carried in LTCC or other fabrication technology with the possibility of realizing higher Q components.

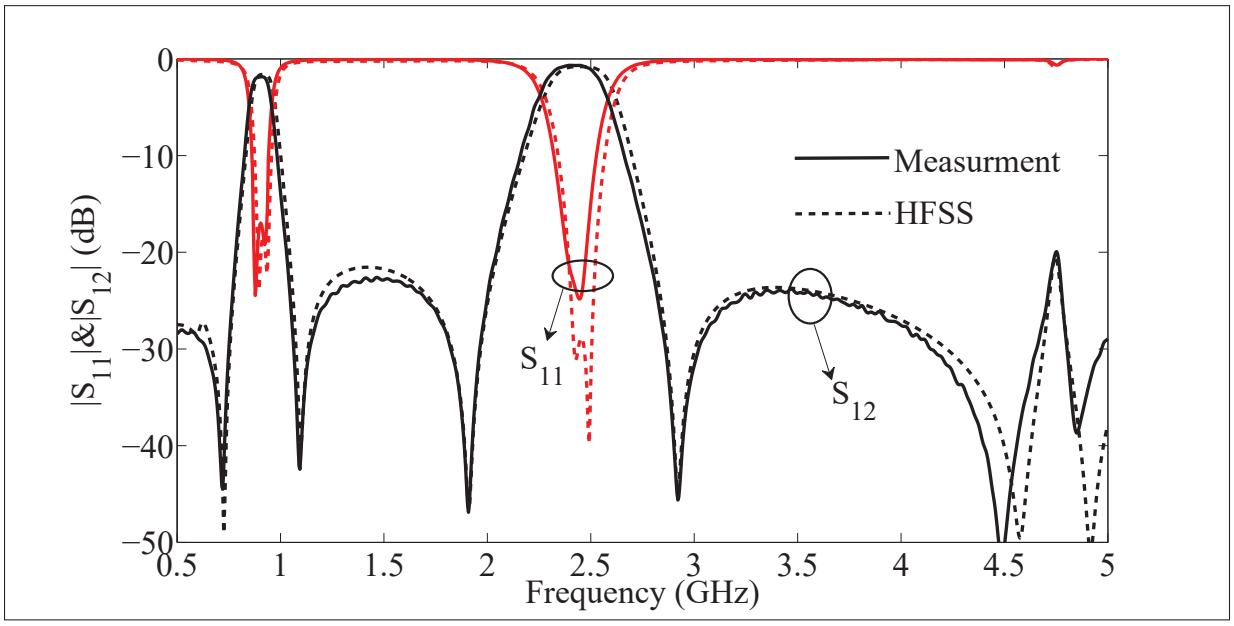

Figure 1.14 Simulated and measured frequency responses of proposed D-BPF

1.7 Appendix A

In this appendix, the mathematical proofs for the following conditions are presented: $f^o_{p,-} < f^o_{z,-} < f^o_{p,+} < f^o_{z,+}$, $f^e_{p,-} < f^e_{z,-} < f^e_{p,+} < f^e_{z,+}$, $f^e_{p,-} < f^o_{p,-}$, $f^e_{p,+} < f^o_{p,+}$, $f^e_{z,-} < f^o_{z,-}$, and $f^e_{z,+} < f^o_{z,+}$.

a. $f^o_{p,-} < f^o_{z,-} < f^o_{p,+} < f^o_{z,+}$ and $f^e_{p,-} < f^e_{z,-} < f^e_{p,+} < f^e_{z,+}$

For simplicity, the derived chain of equations (1.2), (1.3), (1.5) and (1.6), for odd/even modes, are investigated simultaneously and rewritten to (1.32) to (1.35).

$$f^i_{z,+} = \frac{1}{2\pi}\sqrt{\frac{X^i + \sqrt{X^{i2} - 4Y^i}}{2Y^i}} \tag{1.32}$$

$$f^i_{z,-} = \frac{1}{2\pi}\sqrt{\frac{X^i - \sqrt{X^{i2} - 4Y^i}}{2Y^i}} \tag{1.33}$$

where $X^i = C_2L^i_2 + C_1L^i_1 + C_2L^i_1$, $Y^i = C_1C_2L^i_1L^i_2$. The superscripts i indicates *o*/*e*. The investigation of (1.32) to (1.35) demonstrates the validity of above sequences as follow:

$$f^i_{p,+} = \frac{1}{2\pi}\sqrt{\frac{(X^i + C_CL^i_1) + \sqrt{(X^i + C_CL^i_1)^2 - 4(Y^i + C_CC_2L^i_1L^i_2)}}{2(Y^i + C_CC_2L^i_1L^i_2)}} \tag{1.34}$$

$$f^i_{p,-} = \frac{1}{2\pi}\sqrt{\frac{(X^i + C_CL^i_1) - \sqrt{(X^i + C_CL^i_1)^2 - 4(Y^i + C_CC_2L^i_1L^i_2)}}{2Y^i}} \tag{1.35}$$

a. Compare (1.32) with (1.33) and (1.34) with (1.35). Due to the positive and negative internal signs under the square roots, it is clear that $f^i_{z,-} < f^i_{z,+}$ and $f^i_{p,-} < f^i_{p,+}$.

b. The Limit of (1.35) as C_c goes to zero is $f^i_{z,-}$ and this limit as C_c goes to infinity is zero. Thus, we have $0 < f^i_{p,-} < f^i_{z,-}$.

c. The Limit of (1.34) as C_c goes to zero is $f^i_{z,+}$, and this limit as C_c goes to infinity is equal to $f^i_{p,+} = (2\pi)^{-1}(C_2L^i_2)^{-0.5}$. This shows that $f^i_{p,+}$ has a value between $f^i_{z,+}$ and $(2\pi)^{-1}(C_2L^i_2)^{-0.5}$.

Subtracting the term of $4C_1C_2(L^i_1)^2$ from $(X^i)^2 - 4Y^i$ in the right side of (1.32), leads to $(2\pi)^{-1}(C_2L^i_2)^{-0.5}$ which means that $f^i_{z,+}$ is greater than $(2\pi)^{-1}(C_2L^i_2)^{-0.5}$. See (1.36).

$$\lim_{C_C\to\infty} f^i_{p,+} = (2\pi)^{-1}(C_2L^i_2)^{-0.5} < f^i_{p,+} < \lim_{C_C\to 0} f^i_{p,+} = f^i_{z,+} \tag{1.36}$$

Also, subtracting the term of $4C_1C_2(L^i_1)^2$ from in right side of (1.33), leads to the following equation $(2\pi)^{-1}(C_2L^i_2)^{-0.5}$ which means $f^i_{z,-}$ is smaller than $f^i_{p,+}$ when C_c approaches infinity. See (1.37).

$$f^i_{z,-} < \lim_{C_C\to\infty} f^i_{p,+} = (2\pi)^{-1}(C_2L^i_2)^{-0.5} \tag{1.37}$$

From (1.36) and (1.37), we can conclude that

$$f^i_{z,-} < \lim_{C_C\to\infty} f^i_{p,+} = (2\pi)^{-1}(C_2L^i_2)^{-0.5} < f^i_{p,+} < \lim_{C_C\to 0} f^i_{p,+} = f^i_{z,+} \tag{1.38}$$

By combining the obtained results in steps 1 to 3, the following sequence $f^i_{p,-} < f^i_{z,-} < f^i_{p,+} < f^i_{z,+}$ is demonstrated.

b. $f^e_{z,-} < f^o_{z,-}$ and $f^e_{z,+} < f^o_{z,+}$

The investigation of sequences between $f^e_{z,-}$ with $f^o_{z,-}$ and $f^e_{z,+}$ with $f^o_{z,+}$ with is started by the numerators of (1.1) and (1.4) which are

$$N^o_{Yin}(\omega) = \omega^4 X^o - \omega^2 Y^o + 1 \tag{1.39}$$

$$N^e_{Yin}(\omega) = \omega^4 X^e - \omega^2 Y^e + 1 \tag{1.40}$$

where $X^o = C_1C_2L_1^oL_2^o$, $Y^o = C_2L_2^o + C_1L_1^o + C_2L_1^o$, $X^e = C_1C_2L_1^eL_2^e$, and $Y^e = C_2L_2^e + C_1L_1^e + C_2L_1^e$. (1.39) and (1.40) are converted to the standard form of a second degree function as follows:

$$N_{Yin}^o(R) = R^2X^o - RY^o + 1 \tag{1.41}$$

$$N_{Yin}^e(R) = R^2X^e - RY^e + 1 \tag{1.42}$$

where $R = \omega^2$. Each of (1.41) and (1.42) have two roots, R_1^o and R_2^o are roots of (1.41), R_1^e and R_2^e are roots of (1.42). These roots are associated with frequencies $f_{z,-}^e$, $f_{z,-}^o$, $f_{z,+}^e$, and $f_{z,+}^o$ by the formulas (1.43) to (1.46)

$$f_{z,-}^e = \frac{1}{2\pi}\sqrt{R_1^e} \tag{1.43}$$

$$f_{z,-}^o = \frac{1}{2\pi}\sqrt{R_1^o} \tag{1.44}$$

$$f_{z,+}^e = \frac{1}{2\pi}\sqrt{R_2^e} \tag{1.45}$$

$$f_{z,+}^o = \frac{1}{2\pi}\sqrt{R_2^o} \tag{1.46}$$

According to the (1.43) to (1.46), if we demonstrate $R_1^e < R_1^o$ and $R_2^e < R_2^o$, consequently the sequences $f_{z,-}^e < f_{z,-}^o$, $f_{z,+}^e < f_{z,+}^o$ are proven.

As it is known, the graph of any second order equation has general parabola shape. When N_{Yin}^o and N_{Yin}^e are plotted as a function of R, the roots R_1^e, R_1^o, R_2^e, and R_2^o pass the R-axis, see Fig. 1.15. There are two reasons why $R_1^e < R_1^o$ always is valid.

a. the R-coordinate of the vertex point in (1.41) is located at R_V^o which is:

$$R_V^o = \frac{1}{2C_1L_1^o} + \frac{1}{2C_2L_2^o} + \frac{1}{2C_1L_2^o} \tag{1.47}$$

and the R-coordinate of the vertex point in (1.42) is located at R_V^e which is

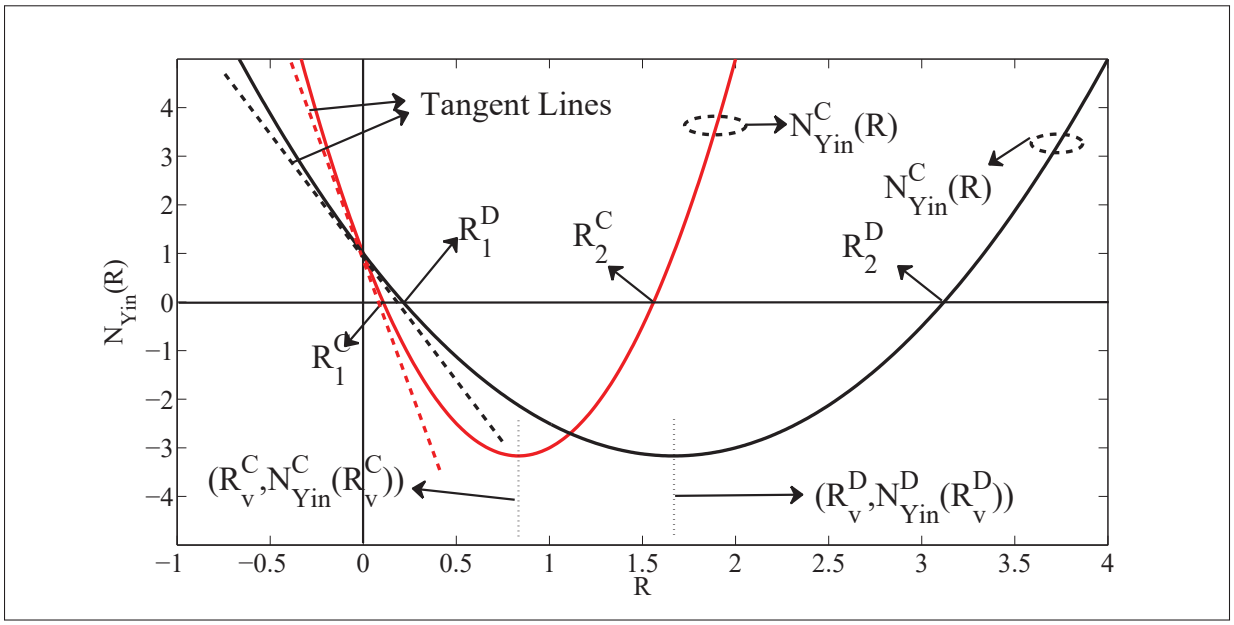

Figure 1.15 Plot of quadratic functions $N^o_{Yin}(R)$ and $N^e_{Yin}(R)$

$$R_V^e = \frac{1}{2C_1L_1^e} + \frac{1}{2C_2L_2^e} + \frac{1}{2C_1L_2^e} \tag{1.48}$$

Obviously, the value of R_V^o cannot be less than the value of R_V^e.

b. Secondly, we know that the derivative of a function at any point gives the slope of the tangent line at the same point. By taking derivative of N^o_{Yin} respect to R at point $R = 0$, the slope of N^o_{Yin} is given by

$$m^o = \frac{dN^o_{Yin}(R=0)}{dR} = -(C_2L_2^o + C_1L_1^o + C_2L_1^o) \tag{1.49}$$

Also the slope of N^e_{Yin} at $R = 0$ point is calculated by

$$m^e = \frac{dN^e_{Yin}(R=0)}{dR} = -(C_2L_2^e + C_1L_1^e + C_2L_1^e) \tag{1.50}$$

By comparing (1.49) and (1.50), the term $|m^o| < |m^e|$ is valid.

Based on the above discussion, it is clear that $R_1^e < R_1^o$ is always valid. Since the second order equation is a symmetric graph respect to vertex point, easily it is concluded that $R_2^e < R_2^o$.

c. $f_{p,-}^e < f_{p,-}^o$ and $f_{p,+}^e < f_{p,+}^o$

The above terms can be demonstrates similar to the process which has been done in the section A-2. It is mentioned that the terms $C_1 L_1^o$ and $C_1 L_1^e$ is substituted with the terms $(C_1 + C_C)L_1^o$ and $(C_1 + C_C)L_1^e$ in all equation from section A-2.

1.8 Appendix B

In this appendix the design formulas of proposed D-BPF are proved. The general form of equations (1.1) and (1.2) is expressed as (1.51). And with simple manipulation (1.51) can be converted to (1.52). Where

$$Y_{in}^i = \frac{j\omega C_C[\omega^4(C_1C_2L_1^iL_2^i) - \omega^2(C_2L_2^i + C_1L_1^i + C_2L_1^i) + 1]}{\omega^4[C_1C_2L_1^iL_2^i + C_CC_2L_1^iL_2^i] - \omega^2[C_2L_2^i + C_1L_1^i + C_2L_1^i + C_CL_1^i] + 1} \tag{1.51}$$

$$Y_{in}^i = \frac{j\omega C_C[\omega^4 - \omega^2({\omega_h^i}^2 + {\omega_s^i}^2 + {\omega_R^i}^2) + {\omega_h^i}^2{\omega_s^i}^2]}{\omega^4(1 + \frac{C_C}{C_1}) - \omega^2[{\omega_h^i}^2 + (1 + \frac{C_C}{C_1}){\omega_s^i}^2 + {\omega_R^i}^2] + {\omega_h^i}^2{\omega_s^i}^2} \tag{1.52}$$

$$\omega_s^i = 2\pi f_s^i = \frac{1}{\sqrt{C_2L_2^i}} \tag{1.53}$$

$$\omega_h^i = 2\pi f_h^i = \frac{1}{\sqrt{C_1L_1^i}} \tag{1.54}$$

$$\omega_R^i = 2\pi f_R^i = \frac{1}{\sqrt{C_1 L_2^i}} \tag{1.55}$$

$$(\omega_{z,+}^i)^2 = 2\pi(f_{z,+}^i)^2 = \frac{{\omega_h^i}^2 + {\omega_s^i}^2 + {\omega_R^i}^2 + \sqrt{\left({\omega_h^i}^2 + {\omega_s^i}^2 + {\omega_R^i}^2\right)^2 - 4{\omega_s^i}^2{\omega_h^i}^2}}{2} \tag{1.56}$$

$$(\omega_{z,-}^i)^2 = 2\pi(f_{z,-}^i)^2 = \frac{{\omega_h^i}^2 + {\omega_s^i}^2 + {\omega_R^i}^2 - \sqrt{\left({\omega_h^i}^2 + {\omega_s^i}^2 + {\omega_R^i}^2\right)^2 - 4{\omega_s^i}^2{\omega_h^i}^2}}{2} \tag{1.57}$$

$$(\omega_{p,+}^i)^2 = 2\pi(f_{p,+}^i)^2 = \frac{{\omega_h^i}^2 + (1+\frac{C_C}{C_1}){\omega_s^i}^2 + {\omega_R^i}^2 + \sqrt{\left({\omega_h^i}^2 + (1+\frac{C_C}{C_1}){\omega_s^i}^2 + {\omega_R^i}^2\right)^2 - 4(1+\frac{C_C}{C_1}){\omega_s^i}^2{\omega_h^i}^2}}{2(1+\frac{C_C}{C_1})} \tag{1.58}$$

$$(\omega_{p,-}^i)^2 = 2\pi(f_{p,-}^i)^2 = \frac{{\omega_h^i}^2 + (1+\frac{C_C}{C_1}){\omega_s^i}^2 + {\omega_R^i}^2 - \sqrt{\left({\omega_h^i}^2 + (1+\frac{C_C}{C_1}){\omega_s^i}^2 + {\omega_R^i}^2\right)^2 - 4(1+\frac{C_C}{C_1}){\omega_s^i}^2{\omega_h^i}^2}}{2(1+\frac{C_C}{C_1})} \tag{1.59}$$

The zeros and poles of (1.52) are presented in (1.56) to (1.59). Since $\omega_{z,+}^i$, $\omega_{z,-}^i$, $\omega_{p,+}^i$, and $\omega_{p,-}^i$ are the roots of a fourth order polynomial equations, the following conditions are satisfied:

$$(\omega_{z,+}^i)^2(\omega_{z,-}^i)^2 = (\omega_s^i)^2(\omega_h^i)^2 \tag{1.60}$$

$$(\omega_{z,+}^{i})^2+(\omega_{z,-}^{i})^2=(\omega_{s}^{i})^2+(\omega_{h}^{i})^2+(\omega_{R}^{i})^2 \tag{1.61}$$

$$(\omega_{p,+}^{i})^2(\omega_{p,-}^{i})^2=\frac{(\omega_{s}^{i})^2(\omega_{h}^{i})^2}{1+\gamma} \tag{1.62}$$

$$(\omega_{p,+}^{i})^2+(\omega_{p,-}^{i})^2=\frac{(\omega_{h}^{i})^2+(1+\gamma)(\omega_{s}^{i})^2+(\omega_{R}^{i})^2}{1+\gamma} \tag{1.63}$$

where γ is

$$\gamma=\frac{C_C}{C_1} \tag{1.64}$$

From (1.60) and (1.62), it is obtained

$$\gamma=\frac{\omega_{z,+}^{i^2}\omega_{z,-}^{i^2}}{\omega_{p,+}^{i^2}\omega_{p,-}^{i^2}}-1 \tag{1.65}$$

And from (1.53) and (1.55), it can be obtained

$$\psi=\frac{C_1}{C_2}=\frac{\omega_{s}^{i^2}}{\omega_{R}^{i^2}} \tag{1.66}$$

If $i=o$, from (1.61) and (1.63) we have:

$$\omega_{s}^{o^2}=\frac{(1+\gamma)(\omega_{p,+}^{o^2}+\omega_{p,-}^{o^2})-\omega_{z,+}^{o^2}-\omega_{z,-}^{o^2}}{\gamma} \tag{1.67}$$

If $i=e$, (1.60) gives

$$\omega_{s}^{e^2}=\frac{\omega_{z,+}^{e^2}\omega_{z,-}^{e^2}}{\omega_{h}^{e^2}} \tag{1.68}$$

By considering $i=e$ and substituting (1.68) in (1.61) yields

$$\omega_{R}^{e^2}=\frac{\omega_{z,+}^{e^2}\omega_{s}^{e^2}+\omega_{z,-}^{e^2}\omega_{s}^{e^2}-\omega_{s}^{e^4}-\omega_{z,+}^{e^2}\omega_{z,-}^{e^2}}{\omega_{s}^{e^2}} \tag{1.69}$$

Substituting (1.69) in (1.66) yields

$$(1+\psi)\left(\omega_s^e\right)^4-\psi\left(\left(\omega_{z,+}^e\right)^2+\left(\omega_{z,-}^e\right)^2\right)\left(\omega_s^e\right)^2+\psi\left(\omega_{z,-}^e\omega_{z,+}^e\right)^2=0 \tag{1.70}$$

the formulas (1.53) to (1.55) are rewritten when $i=e$ and $i=o$ as follows

$$\omega_s^o=2\pi f_s^o=\frac{1}{\sqrt{C_2(L_2-Lm_2)}}\omega_s^e=2\pi f_s^e=\frac{1}{\sqrt{C_2(L_2+Lm_2)}} \tag{1.71}$$

$$\omega_h^o=2\pi f_h^o=\frac{1}{\sqrt{C_1(L_1-Lm_1)}}\omega_h^e=2\pi f_h^e=\frac{1}{\sqrt{C_1(L_1+Lm_1)}} \tag{1.72}$$

$$\omega_R^o=2\pi f_R^o=\frac{1}{\sqrt{C_1(L_2-Lm_2)}}\omega_R^e=2\pi f_R^e=\frac{1}{\sqrt{C_1(L_2+Lm_2)}} \tag{1.73}$$

From (1.72), L_1 and Lm_1 can be derived as follows

$$L_1=\frac{1}{2C_1}\left[\frac{1}{\omega_h^{e2}}+\frac{1}{\omega_h^{o2}}\right] \tag{1.74}$$

$$Lm_1=\frac{1}{2C_1}\left[\frac{1}{\omega_h^{e2}}-\frac{1}{\omega_h^{o2}}\right] \tag{1.75}$$

Similarly, L_2 and Lm_2 can be obtained from (1.71)

$$L_2=\frac{1}{2C_2}\left[\frac{1}{\omega_s^{e2}}+\frac{1}{\omega_s^{o2}}\right] \tag{1.76}$$

$$Lm_2=\frac{1}{2C_2}\left[\frac{1}{\omega_s^{e2}}-\frac{1}{\omega_s^{o2}}\right] \tag{1.77}$$

Since, the network parameters are positive, by considering (1.75), the below term should be satisfied

$$\frac{f_s^o}{f_s^e}<\frac{f_{z,+}^o f_{z,-}^o}{f_{z,+}^e f_{z,-}^e} \tag{1.78}$$

CHAPTER 2

DIRECT SYNTHESIS OF LUMPED-ELEMENT SINGLE- AND DUAL- NARROW BANDPASS FILTERS IN LTCC

Aref Pourzadi[1], Mohsen Niayesh[1], Ammar Kouki[1]

[1] Département de Génie Électrique, École de Technologie Supérieure,
1100 Notre-Dame Ouest, Montréal, Québec, Canada H3C 1K3

Manuscript submitted to IEEE Transactions on Circuits and Systems I: Regular Papers in November 2019.

Abstract

In this paper, the design of a new compact second-order lumped-element narrow bandpass filter (SNBPF) with a narrow 10 dB fractional bandwidth (FBW) (less than 3%) is presented. Using even and odd mode analyses, the working mechanism of the SNBPF circuit model is explained and an analytical design procedure is provided to obtain the element values. To reject spurious signals, two transmission zeros (TZs) are generated in both sides of the center frequency. Manipulating SNBPF circuit model, a single narrow frequency response is generalized to dual-narrowband frequency responses (DNBPF). Performing the same analysis, the working mechanism and design procedure of the DNBPF topology are fully described. To demonstrate the theory of both narrow bandpass filters (NBPFs), two design examples are provided. To reach a very compact size and enough flexibility to build inductive couplings, physical layouts are realized in the form of 3-D configuration using low-temperature cofired ceramic (LTCC) technology.

Introduction

Narrowband standards such as the global positioning system (GPS)Liu *et al.* (2010), personal communication services (PCS)Kim *et al.* (1999) and wireless communication services (WCS)Chetouah *et al.* (2016) are commonly referred with respect to the industrial applications

of the single narrow bandpass filters (SNBPFs). These filters would allow narrow-bandwidth modulated signals to be extracted from multiple interfering signals and improve system signal to noise ratio (SNR). Over the past few years, several classes of narrow bandpass filters have been developed with various features. Typical reported strategies for the SNBPFs realizations include the following: substrate integrated waveguides (SIW)He *et al.* (2014), cavity resonatorsLorente *et al.* (2013), parallel coupled lines, split ring resonators and high-temperature superconductors (HTS) using planar microstrip technology Shao & Lin (2015); Liu *et al.* (2016); Li *et al.* (2006), active SNBPFs implemented in CMOSSu & Tzuang (2012) and realized lumped-element structures in LTCC Brzezina *et al.* (2009); Xu *et al.* (2016b). The properties of existing reported strategies have been summarized, as shown in table 2.1. Utilization of active SNBPFs is limited due to the power consumption. SIWs and filters using microstrip technology have a relatively bulkier size at low frequencies, which limits their integration with other blocks. Lumped-element topologies are highly recommended for filters operating at less than 5GHz in order to reach a very compact size.

Table 2.1 Properties OF The Proposed SNBPFs Design Strategies

	Size	Easy Integration	Selectivity	Power Consumption	Loss
SIW	bulky	yes	medium	no	medium
Lumped-element	compact	yes	medium	no	medium
Waveguide	bulky	poor	high	no	low
HTS	medium	yes	high	no	low
Microstrip	medium	yes	medium	no	medium
Cmos	compact	yes	medium	yes	low

Among various options for realizing lumped-elements, monolithic microwave integrated circuits (MMIC), surface mount devices (SMD) and LTCC, the last is more attractive. The 3-D layout realization in LTCC provides a very compact size, apart from other features such as low loss at high frequencies, integration capabilities in 3-D environment and low cost.

In the literature, several design methods of LTCC bandpass filters (BPFs) have been reported with various degrees of performance and FWB. In Choi *et al.* (2003), using half-wavelength coupled resonators leads to a bulky size for a designed circuit at microwave frequencies. In Deng *et al.* (2005) and Yang *et al.* (2010), the limited number of TZs degrade due to band rejection. In Xu *et al.* (2016b), the passband frequency responses are obtained based on a direct synthesis method, but the very narrow FBW is not supported by the proposed circuit. In Zhang *et al.* (2014) and Dai *et al.* (2014), the desired frequency responses cannot be precisely specified, due to the proposed optimization design methodologies.

In this paper, a new topology of a lumped-element LTCC bandpass filter for applications with small FBW is introduced. Existing three coupled inductors in the input of proposed circuit model lead to an increase in the loaded Q-factor of the circuit at the given resonant frequency which concludes narrowband frequency responses. Through an even/odd modes analysis, the proposed SNBPF is supported by a straightforward design procedure that uses closed-form synthesis equations to control even/odd mode poles. This analytical solution provides flexibility, allowing the application of the new topology in different frequencies of spectrum and, therefore, creates a narrow bandpass response of the network. To reject out-of-band spurious signals, two TZs are appointed in both sides of the passband.

Further, it is demonstrated that the single bandpass is generalized to dual-band frequency responses through manipulation of the proposed SNBPF circuit model. In the light of increasing demand for multiband wireless communication systems, some researches have been conducted on LTCC filters with dual-band frequency responses, (see Lin *et al.* (2014); Xu *et al.* (2013); Oshima *et al.* (2010); Chen *et al.* (2009); Chen (2005); Pourzadi *et al.* (2019)). Similar to the SNBPF, a direct synthesis method with closed-form equations is provided to synthesize a dual-narrow bandpass filter (DNBPF). In the new DNBPF, existing independent poles are asset, for they have independent and controllable external quality factors at both bands. The center frequencies can be adjusted, whereas wide or tight frequency separation between passbands is possible.

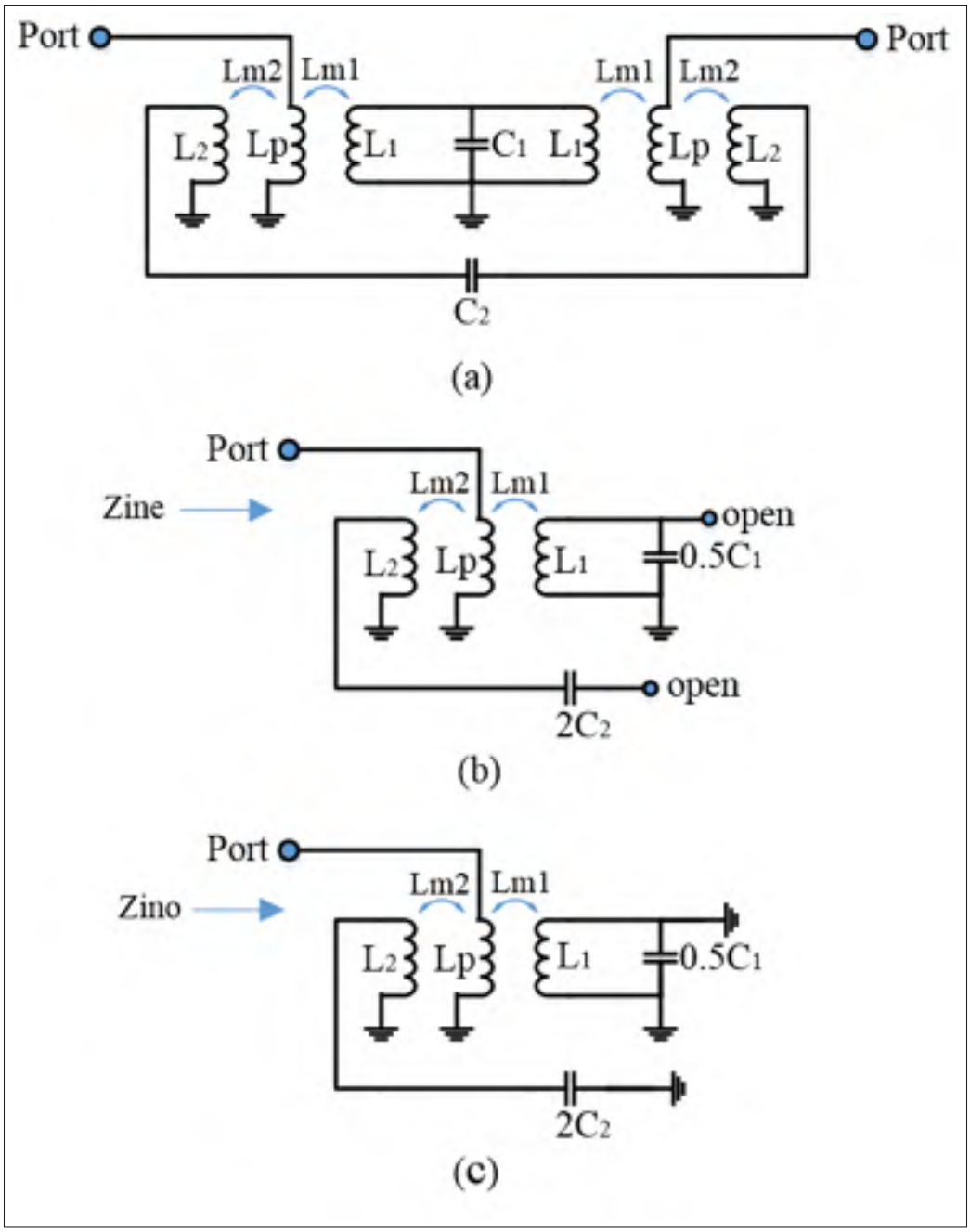

Figure 2.1 (a) Circuit model of the proposed SNBPF. (b) Circuit model of the SNBPF under even mode excitation. (c) Circuit model of the SNBPF under odd mode excitation

2.1 Design of LTCC SNBPF

2.1.1 Circuit Model of SNBPF

Fig.2.1(a) shows the circuit model of the SNBPF, which contains four major parts, namely, input inductance $[L_p]$, shunt resonator $[C_1, L_1]$, series resonator $[C_2, L_2]$ and input inductive couplings $[Lm_1, Lm_2]$. Due to the symmetry of the circuit model, even and odd mode analysis can be used. Under even/odd modes excitations, Fig.2.1(a) is decomposed into Fig.2.1(b) and Fig.2.1(c), respectively. The input impedance of the equivalent circuit under even excitation is calculated as follows:

$$Z_{ine} = \frac{j\omega\left[(Lm_1^2 - L_1L_p)C_1\omega^2 + 2L_p\right]}{2 - \omega^2 C_1 L_1} \tag{2.1}$$

The Z_{ine} resonates when $2 - \omega^2 C_1 L_1 = 0$. Equating DEN (Z_{ine}) to zero gives two poles out of which only the positive pole is considered. This pole f_e^p is equated as shown in (2.2).

$$f_e^p = \frac{1}{2\pi}\sqrt{\frac{2}{C_1 L_1}} \tag{2.2}$$

The terms p and e indicate pole and even mode. Similar to the above analysis, under odd excitation, the input impedance of the equivalent circuit can be obtained by (2.3).

$$Z_{ino} = j\omega L_p - \frac{j2\omega C_2(j\omega Lm_2)^2}{1 - 2\omega^2 C_2 L_2} - \frac{j\omega Lm_1^2}{L_1} \tag{2.3}$$

Repeatedly, Z_{ino} resonates when DEN (Z_{ino}) is equal to zero. Equating $2 - \omega^2 C_2 L_2 = 0$ gives two poles out of which the positive one is of interest. The pole f_o^p is found to be as follows:

$$f_o^p = \frac{1}{2\pi}\frac{1}{\sqrt{2C_2L_2}} \tag{2.4}$$

The term o indicates odd mode. f_e^p and f_o^p determine the nature of the frequency, response of the circuit of Fig.2.1a. Fig.2.2 illustrates a typical example for even/odd impedance curves versus frequency to show how the placements of the poles create a narrow bandpass frequency response.

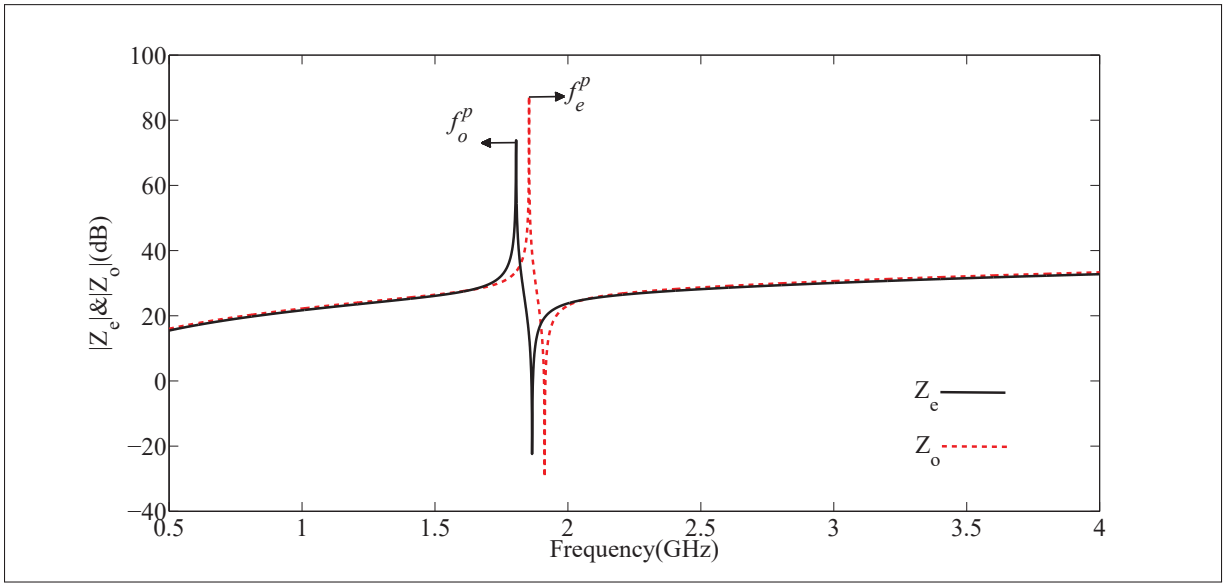

Figure 2.2 Input impedances of even and odd modes

2.1.2 Design Procedure of SNBPF

A second-order Chebyshev bandpass frequency response Dancila & Huynen (2011) is applied to calculate the two poles, f_e^p and f_o^p. We start with the assigned center frequency f_c, the desired bandwidth BW and the in-band return loss RL. The values of the coupling coefficient K_M and the external quality factor Q_e correspond to the BW, f_c and g_i elements by the following equations Dancila & Huynen (2011):

$$K_M = \frac{BW}{f_c}\sqrt{\frac{1}{g_1 g_2}} \tag{2.5}$$

and

$$Q_e = \frac{g_0 g_1 f_c}{BW} \tag{2.6}$$

f_c can be calculated by averaging the pole frequencies, as

$$f_c = \frac{f_e^p + f_o^p}{2} \tag{2.7}$$

and K_M corresponds to f_e^p and f_o^p by formula Hong & Lancaster (2004):

$$K_M = \frac{(f_e^p)^2 - (f_o^p)^2}{(f_e^p)^2 + (f_o^p)^2} \tag{2.8}$$

Using a nonlinear optimization technique for solving (2.7) and (2.8), one obtains optimal values of f_e^p and f_o^p. In equations (2.2) and (2.4), the arbitrary values of C_1 and C_2 constitutes degrees of freedom in our design procedure and, then, are used to calculate of L_1 and L_2. Noting that the values of C_1, C_2, L_1 and L_2 must be adjusted according to fabrication restrictions. To calculate the values of the remained parameters Lm_1, Lm_2 and L_p, we continue with the the frequency responses of the proposed SNBPF which are given by:

$$S_{11} = S_{22} = \frac{Z_{ine}Z_{ino} - Z_0^2}{(Z_{ine} + Z_0) + (Z_{ino} + Z_0)} \tag{2.9}$$

$$S_{12} = S_{21} = \frac{Z_0(Z_{ine} - Z_{ino})}{(Z_{ine} + Z_0) + (Z_{ino} + Z_0)} \tag{2.10}$$

where $Z_0 = 50$ is the port impedance. Solving $S_{12} = S_{21} = 0$ proves existence of two TZs, which are excited by the following equation:

$$\begin{aligned} &C_1C_2L_1^2Lm_2^2\omega^4 - \\ &2C_2(L_1Lm_2^2 + L_2Lm_1^2)\omega^2 + Lm_1^2 = 0 \end{aligned} \tag{2.11}$$

in the frequencies of

$$\omega_{1Z} = \sqrt{\frac{-b + \sqrt{b^2 - 4C_1C_2(L_1Lm_2Lm_1)^2}}{2C_1C_2L_1^2Lm_2^2}} \tag{2.12}$$

$$\omega_{2Z} = \sqrt{\frac{-b - \sqrt{b^2 - 4C_1C_2(L_1Lm_2Lm_1)^2}}{2C_1C_2L_1^2Lm_2^2}} \tag{2.13}$$

where $b = -C_2(L_1Lm_2^2 + L_2Lm_1^2)$, $\omega_{1Z} = 2\pi f_{1Z}$ and $\omega_{2Z} = 2\pi f_{2Z}$. f_{1z} and f_{2z} are corresponded to f_c as

$$f_{1z} = \frac{2f_c - \gamma}{2} \tag{2.14}$$

$$f_{2z} = \frac{2f_c + \gamma}{2} \tag{2.15}$$

where γ indicates the value of frequency spacing between TZs, f_{1z} and f_{2z} . From (2.14) and (2.15), the values of f_{1z} and f_{2z} are calculated by inserting the assigned value of γ and

then solving (2.12) and (2.13), we can find the values of Lm_1 and Lm_2. With the obtained element values and using the given Q_e for the desired passband, we can compute L_p. Q_e can be approximated by the following equationXu *et al.* (2016a):

$$Q_e \approx \frac{\pi \left[f_e^p \tau_{S11}(f_e^p) + f_o^p \tau_{S11}(f_o^p) \right]}{2} \tag{2.16}$$

where

$$\tau_{S11}(f_e^p) = -\frac{\partial \phi_{S11}(f_e^p)}{2\pi \partial f} \tag{2.17}$$

and

$$\tau_{S11}(f_o^p) = -\frac{\partial \phi_{S11}(f_o^p)}{2\pi \partial f} \tag{2.18}$$

where $\tau_{S11}(f_e^p)$ and $\tau_{S11}(f_o^p)$ are the group delays of S_{11} at the frequencies of f_e^p and f_o^p, respectively. Using a graphical solution, we sweep L_p to find a suitable value for satisfying the required Q_e. The above-detailed synthesis steps of SNBPF design are summarized in Fig.2.3, in the form of a chart.

2.1.3 Simulation and Experimental Results of SNBPF

Using the above synthesis procedure, this section illustrates the design and prototyping of a second-order Chebysheve WCS narrow bandpass filter operating at 2.2925-2.3325 GHz. Based on the desired frequency band, we have $f_c = 2.3125$ GHz and $BW = 40$ MHz. By requiring a return loss of 20 dB at Passband, the filter's g_i are found to be $g_0 = 1$, $g_1 = 0.6923$, $g_2 = 0.5585$ and $g_3 = 1.2396$. Using the values of g_i elements, f_c and BW, in (2.5) and (2.6), we obtain $K_M = 2.78\%$ and Q_e =40. Then, (2.7) and (2.8) are used in a nonlinear optimization algorithm in MATLAB to calculate the values of the pole frequencies, which are found to be $f_e^p = 2.345$ GHz and $f_o^p = 2.28$ GHz. As the degrees of freedom, the values of C_1 and C_2 are selected to

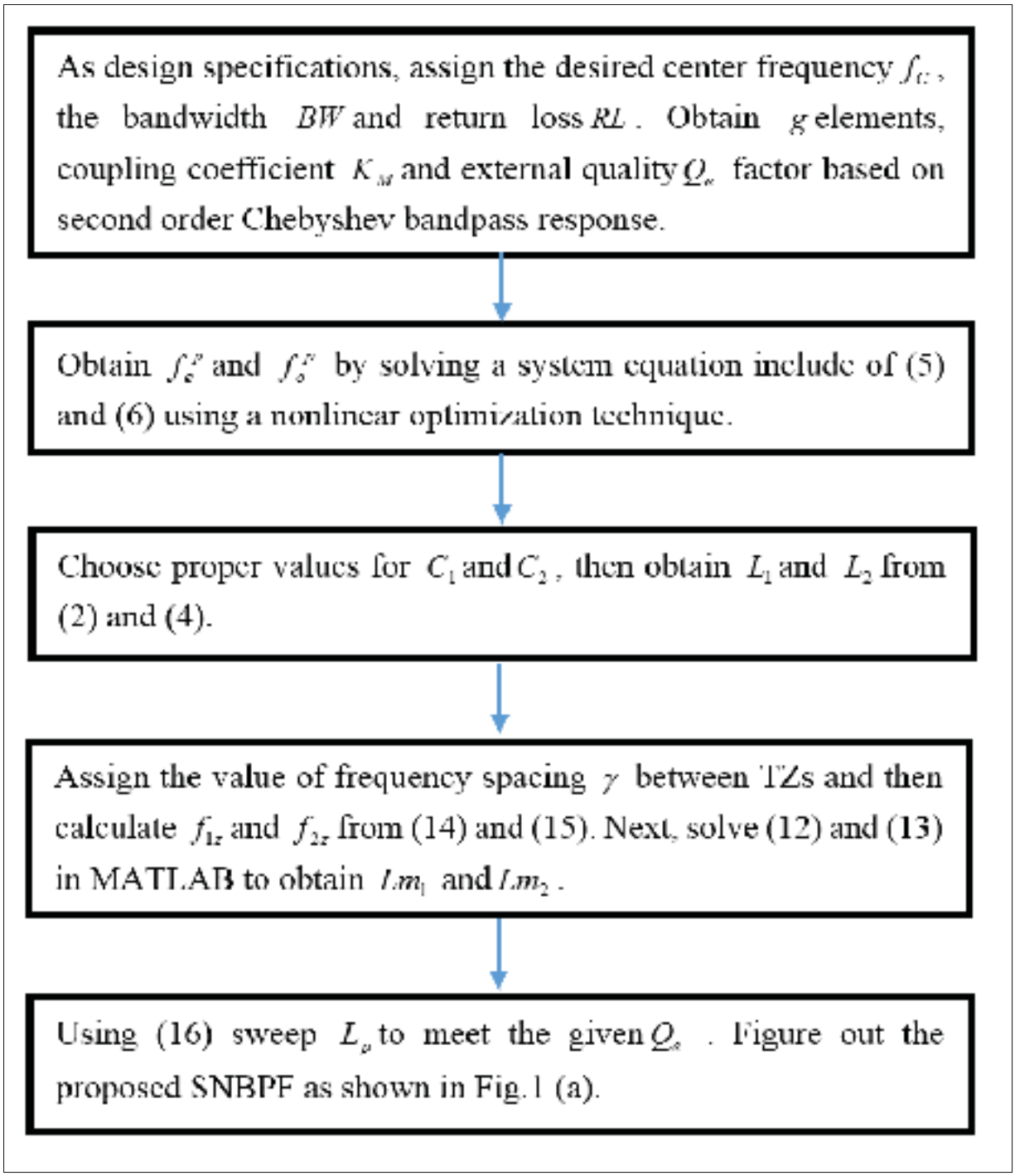

Figure 2.3 Flowchart of synthesis steps for the proposed SNBPF design

be 1.6 pF and 1.9 pF, and from (2.2) and (2.4), the values of L_1 and L_2 are calculated to be 5.76 nH and 1.28 nH, respectively. The fabrication process and it's limitations should be taken

to account for the values of these elements. In addition, high self resonance frequency (SRF) and high quality factorMousavi & Kouki (2015) should be considered for the targeted design. Selecting γ to be 520 MHz and using (2.14) and (2.15), we compute $f_{1z} = 2050$ MHz and $f_{1z} =$ 2570 MHz, which are then used in (2.12) and (2.13) to calculate the values of Lm_1 and Lm_2. Solving (2.12) and (2.13), Lm_1 and Lm_2 are found to be 0.793 nH and 0.379 nH, respectively. The remaining parameter L_p is computed through the graphical solution. As shown in Fig.2.4, L_p is swept from 0.1 to 5 nH and Q_e is calculated using (2.16). It can be realized that the ideal value of L_p is 2.5 nH to meet the given Q_e=40. Fig.2.5 plots the obtained frequency responses of the designed SNBPF circuit model. Using the 3-D field simulator HFSS, the calculated values of the lumped-elements are synthesized following the technique presented in Brzezina *et al.* (2009) and then integrated to form the entire filter on LTCC. Regarding the required capacitance and inductance values, we choose to implement capacitors based on multilayer parallel plates and inductors using curved line configurations. An optimization of the overall dimensions are performed to obtain the final physical layout, as shown in Fig.2.6. The SNBPF is fabricated on LTCC Ferro A6M, with the dielectric constant of 5.7, and the loss tangent of 0.001. The LTCC wafer is consists of seven ceramic sheets, two sheets with the thickness of 2 mil and five sheets with the thickness of 5 mil, along with three metal layers. The material of the conductors is silver with a thickness of 0.008 mm and the diameter of vias is 0.137 mm. The top view of the fabricated circuit is shown in Fig.2.7. The final dimensions of the fired filter are 6.2 mm$\times$ 4.14 mm with the total fired thickness of 0.736 mm. As shown in Fig.2.8, there is a good agreement between EM simulation and the measurement results. The insertion loss is about 2 dB and the return loss is greater than 18 dB. The two TZs appear at both sides of the passband and are located at 2 GHz and 2.71 GHz frequencies. Finally, Table 2.2 includes the comparison performances of bandpass LTCC filters with various $FWBs$.

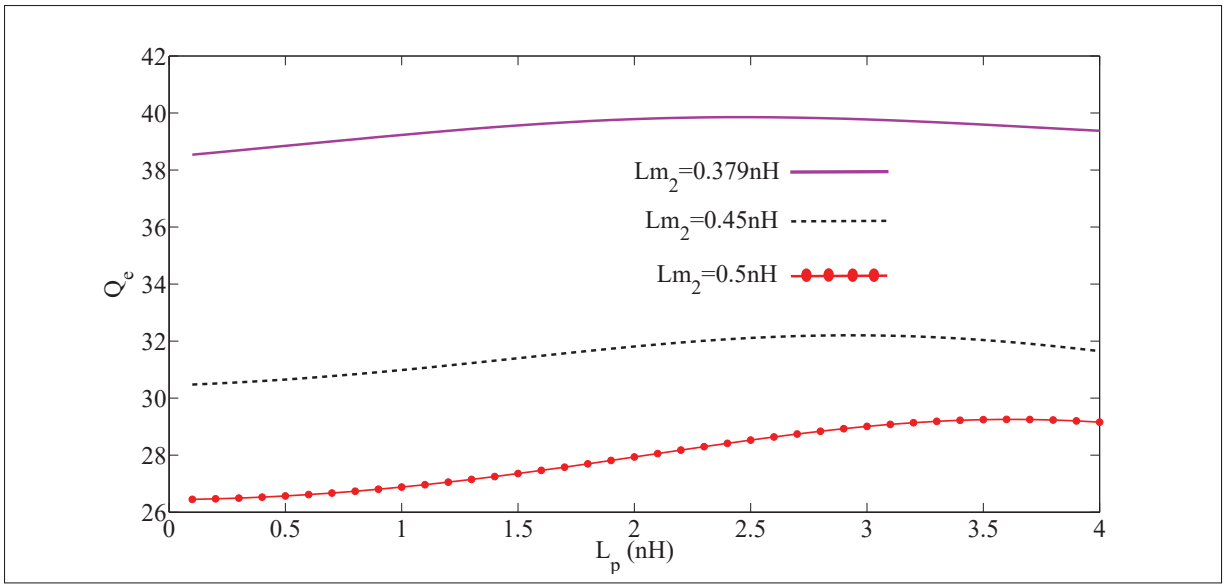

Figure 2.4 Variation of L_p versus Q_e

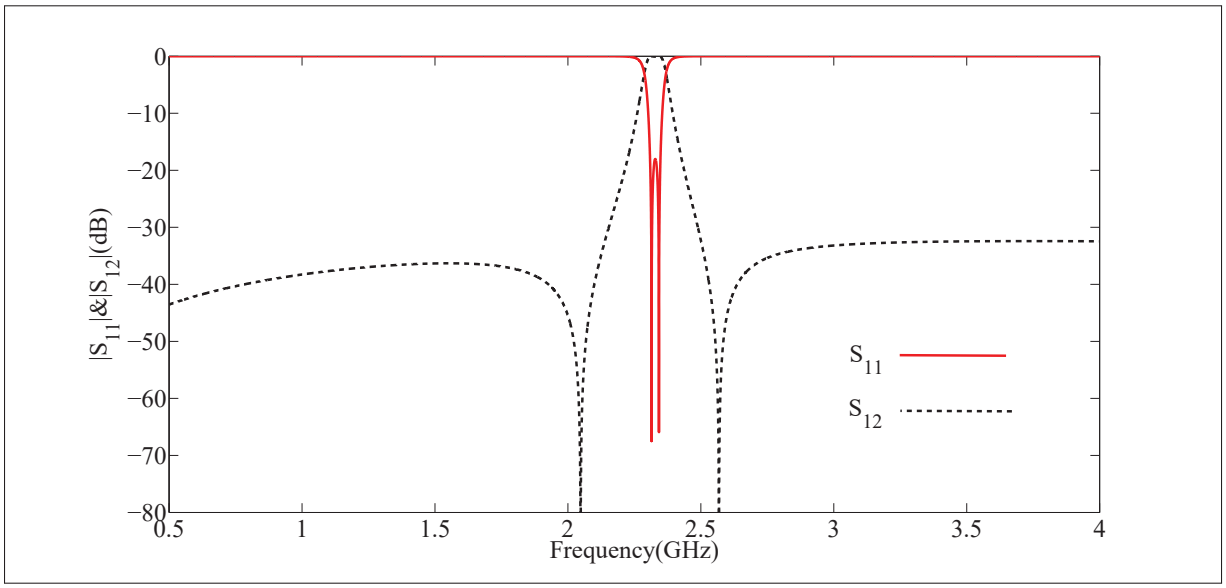

Figure 2.5 Theoretical and simulation results of the proposed SNBPF circuit model

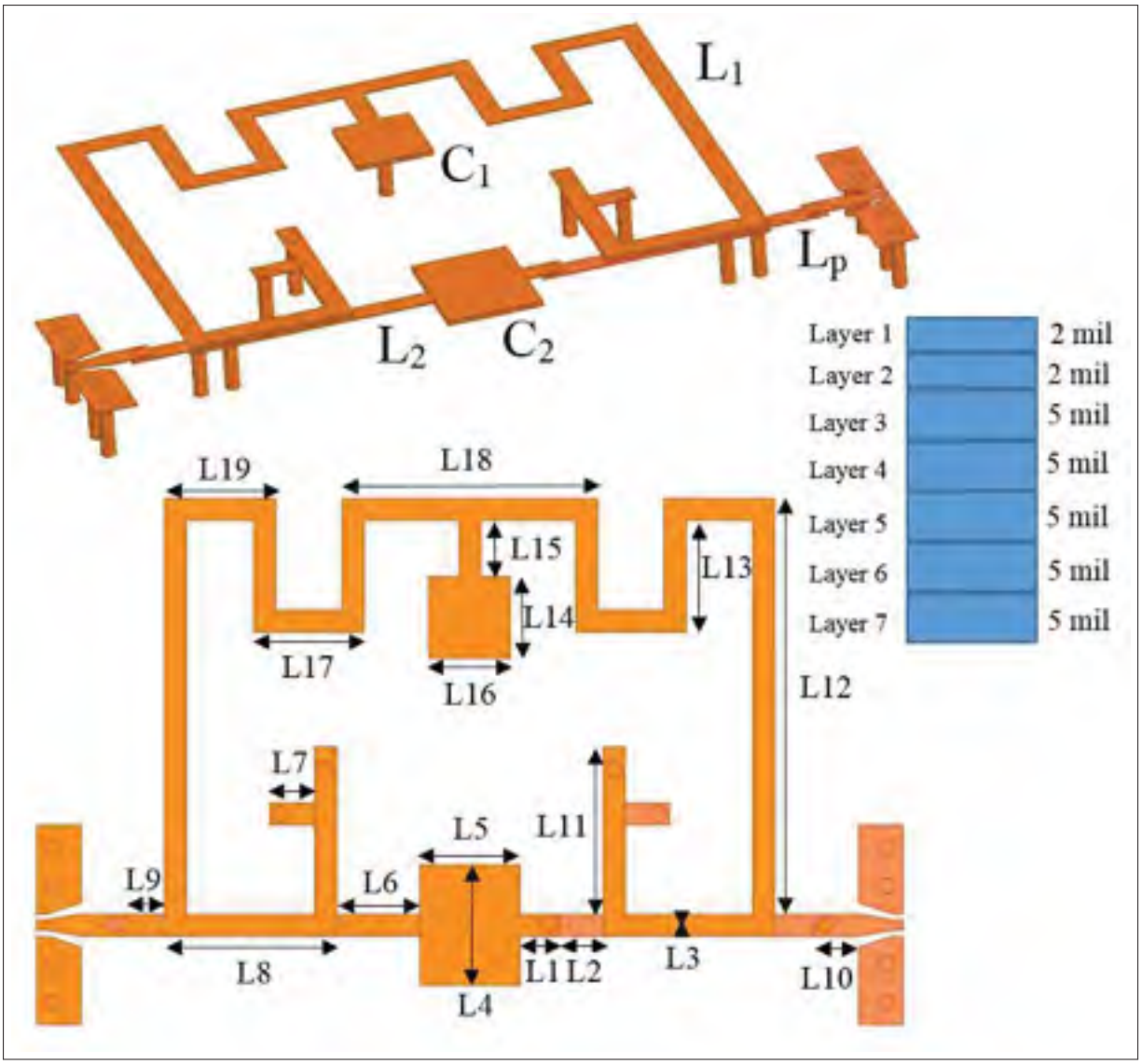

Figure 2.6 3-D view of proposed NBPF. The dimensions are determined as follows (in millimeters):L1 = 0.35, L2 = 0.6, L3 = 0.2, L4 = 1.09, L5 = 0.9, L6 = 0.75, L7 = 0.4, L8 = 1.55, L9 = 0.35, L10 = 0.4, L11 = 1.5, L12 = 3.74, L13 = 1, L14 = 0.74, L15 = 0.5, L16 = 0.73, L17 = 1, L18 = 2.3, L19 = 1

2.2 Design OF LTCC DNBPF

2.2.1 Circuit Model of DNBPF

The single narrow bandpass frequency response is generalized to the dual-band frequency response through a small manipulation in the topology of the proposed SNBPF. Schematic of

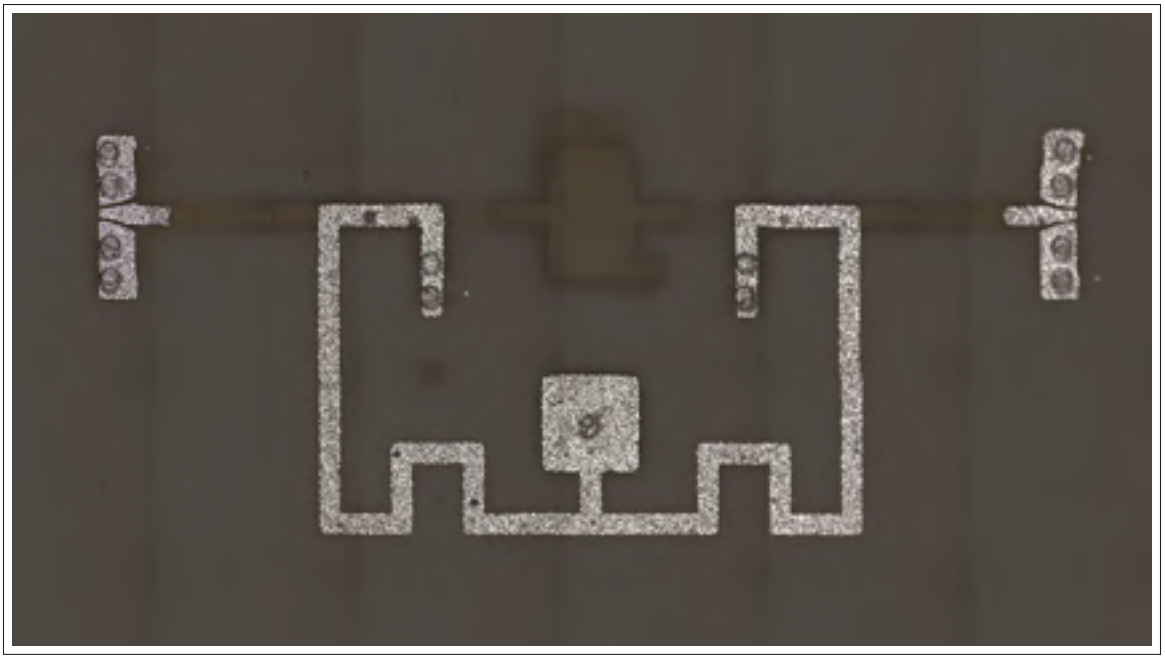

Figure 2.7 Photograph of fabricated SNBPF

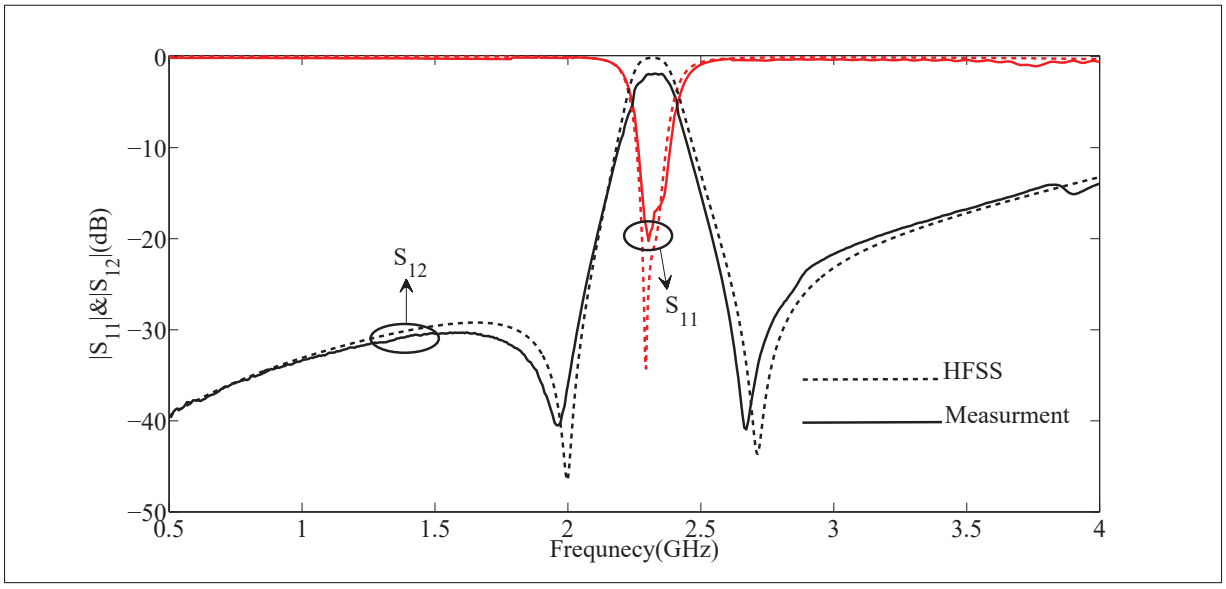

Figure 2.8 EM simulated and measured frequency responses of SNBPF

DNBPF is introduced by replacing the series capacitors C_2 of Fig.2.1(a) by a shunt grounded form. Fig.2.9(a) shows the circuit model of the DNBPF. Similar to previous designs, we use the even/odd mode excitations for analysis and working mechanism investigations. The even/odd

mode equivalent circuits of the proposed DNBPF are illustrated in Fig.2.9(b) and Fig.2.9(c). The input impedances Z_{ine} and Z_{ino} are derived as:

Table 2.2 Performance Comparison of the the SNBPF with Previous Designed LTCC Filters

Ref	Center Frequency (GHz)	Return Loss (dB)	Insertion Loss (dB)	FWB %	Number of TZ	Design Method	Size
Xu *et al.* (2016b)	2.6	-20	2.47	10.2	3	synthesis	$2\times1.7\times2mm^3$
Choi *et al.* (2003)	28.7	<-20	3	4.5	No	synthesis	$9.7\times2.2\times0.42mm^3$
Deng *et al.* (2005)	2.95	<-20	1.4	7.3	No	synthesis	$3.5\times3.5\times0.4mm^3$
Yang *et al.* (2010)	2.45	-14	2.5	8	1	optimization	$0.75\times0.76\times0.67mm^3$
Zhang *et al.* (2014)	2.4	-15	2.4	12.5	4	optimization	$2.63\times2.61\times0.5mm^3$
Dai *et al.* (2014)	2.45	-15	2.5	10.8	4	optimization	$2.48\times2.02\times0.6mm^3$
This work	2.31	-18	2	2.78	2	synthesis	$6.2\times4.14\times0.73mm^3$

$$Z_{ine} = j\omega L_p + \frac{j\omega^3 C_2 L m_2^2}{2-\omega^2 C_2 L_2} + \frac{j\omega^3 C_1 L m_1^2}{2-\omega^2 C_1 L_1} \tag{2.19}$$

$$Z_{ino} = j\omega L_p - \frac{j\omega L m_2^2}{L_2} - \frac{j\omega L m_1^2}{L_1} \tag{2.20}$$

Z_{ine} will resonate when $2-\omega^2 C_2 L_2 = 0$ and $2-\omega^2 C_1 L_1 = 0$. Therefore, the proposed NDBPF has four poles which only positives are desired. These poles are determined by

$$f_{1e}^{p} = \frac{1}{2\pi}\sqrt{\frac{2}{C_1 L_1}} \tag{2.21}$$

$$f_{2e}^{p} = \frac{1}{2\pi}\sqrt{\frac{2}{C_2 L_2}} \tag{2.22}$$

Equating S_{12} =0 in (2.8) proves that the DNBPF generates one TZ located at given frequency

$$f_z = \frac{1}{2\pi}\sqrt{\frac{2(L_1 Lm_2^2 + L_2 Lm_1^2)}{C_1 L_1^2 Lm_2^2 + C_2 L_2^2 Lm_1^2}} \tag{2.23}$$

2.2.2 Design Procedure of DNBPF

Center frequency of first passband f_{1c}, and of second passband f_{2c}, the external quality factor of first passband Q_{1e}, and of second passband Q_{2e} and transmission zero f_z are assigned as the design specifications of the DNBPF. As degrees of freedom, we select proper values for C_1 and C_2, and then using the given center frequencies and equations (2.21) and (2.22), the values of L_1 and L_2 are obtained. It should be noted that f_{1c} and f_{2c} are approximated as $f_{1c} \approx f_{1e}^{p}$ and $f_{2c} \approx f_{2e}^{p}$ in (2.21) and (2.22). The shape and selectivity of the two passbands are controlled by the values of Q_{1e} and Q_{2e}, which are calculated from Hong & Lancaster (2004).

$$Q_{1e} = \frac{f_{1C}}{\Delta f_{1C}^{3dB}} = \pi f_{1C} \tau_{S11}(f_{1C}) \tag{2.24}$$

$$Q_{1e} = \frac{f_{2C}}{\Delta f_{2C}^{3dB}} = \pi f_{2C} \tau_{S11}(f_{2C}) \tag{2.25}$$

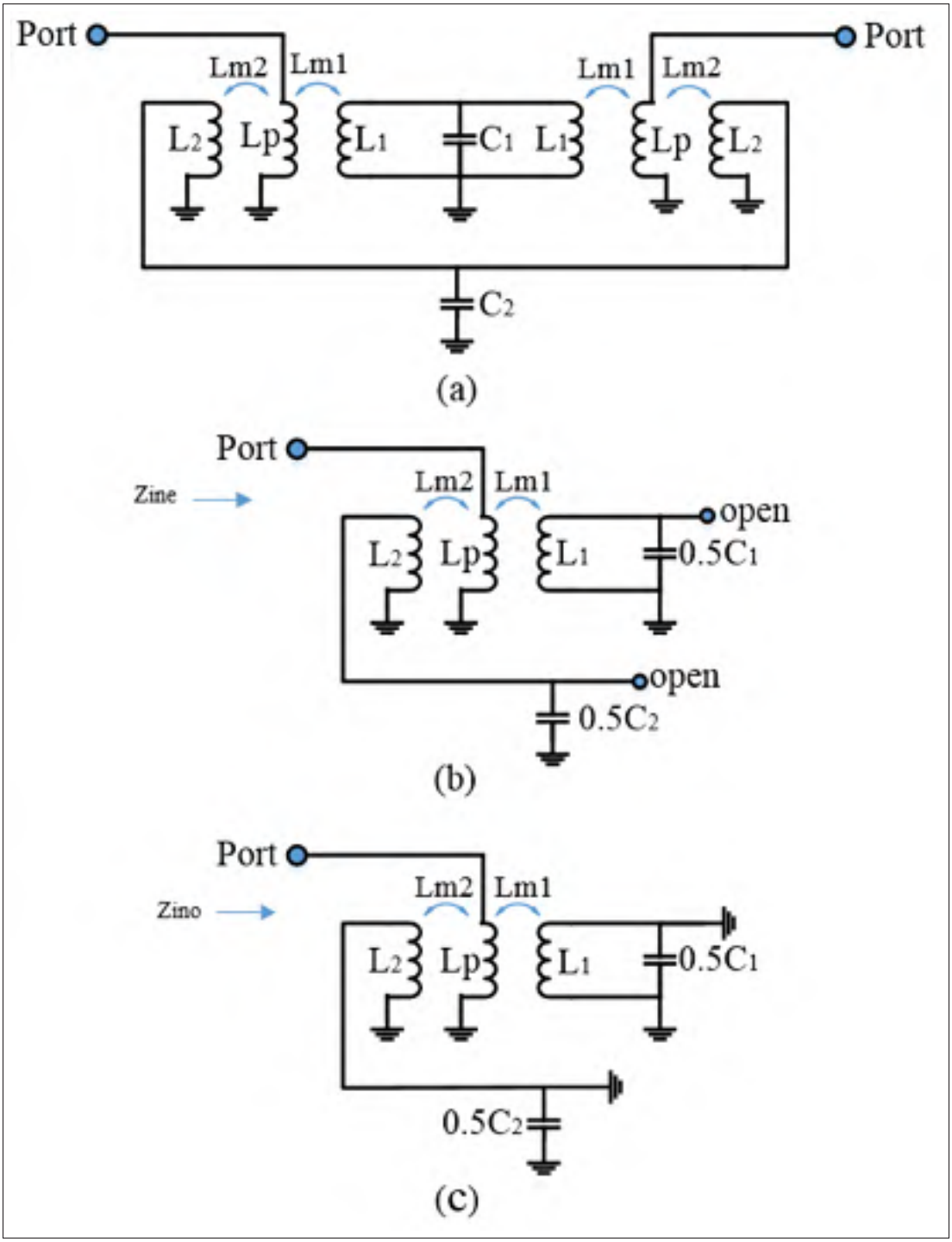

Figure 2.9 (a) Circuit model of the proposed DNBPF. (b) Circuit model of DNBPF under even mode excitation. (c) Circuit model of DNBPF under odd mode excitation

where $\tau_{S11}(f_{1C})$ and $\tau_{S11}(f_{2C})$ are the group delays of S_{11} at the center frequencies. The remaining unknown values L_p , Lm_1 and Lm_2 are calculated by solving the system equation including (2.23) to (2.25). One solution to solve this system equation is to use specific nonlinear programming solver FMINCON in MATLAB. FMINCON find the minimum of error function by fitting different values L_p , Lm_1 and Lm_2 in (2.23) to (2.25). The total error function is defined as

$$\min(e_T) = e_1 + e_2 + e_3 \tag{2.26}$$

where

$$e_1 = |given(Q_{1e}) - calculated(Q_{1e})| \tag{2.27}$$

and

$$e_2 = |given(Q_{2e}) - calculated(Q_{2e})| \tag{2.28}$$

and

$$e_3 = |given(Q_{3e}) - calculated(Q_{3e})| \tag{2.29}$$

Note that due to approximations $f_{1c} \approx f_{1e}^{p}$ and $f_{2c} \approx f_{2e}^{p}$ in the proposed design procedure, a central slight shifting is expected in the center frequencies. With small tuning of C_1 and C_2 values, both bands can be adjusted at the desired frequencies, but the nonlinear solving process is affected by the new values of C_1 and C_2. Furthermore, one has to recalculate L_p, Lm_1 and Lm_2 using updated C_1 and C_2 to meet the given values of Q_{1e} and Q_{2e}. The synthesis steps of the DNBPF design procedure are summarized in Fig.2.10, in the form of a chart.

2.2.3 Simulation and Experimental Results of DNBPF

This section illustrates a designed and prototyped of DNBPF operating at PCS(1.905-1.910) GHz / WCS(2.305-2.320) GHz to validate the theory explained in the previous section. Based on the desired frequencies and the given external quality factors, we have $f_{1c} = 1.9075$ GHz, $f_{2c} = 2.3125$ GHz, $Q_{1e} = 18$, $Q_{2e} = 22$ and TZ is assigned to be 2.1 GHz. To follow the design procedure, we need to select the values of C_1 and C_2. Selecting $C_1 = 2.6$ pF and $C_2 = 4.7$ pF and using (2.21) and (2.22), then L_1 and L_2 are calculated to be 5.36 nH and 2.02 nH. By solving the

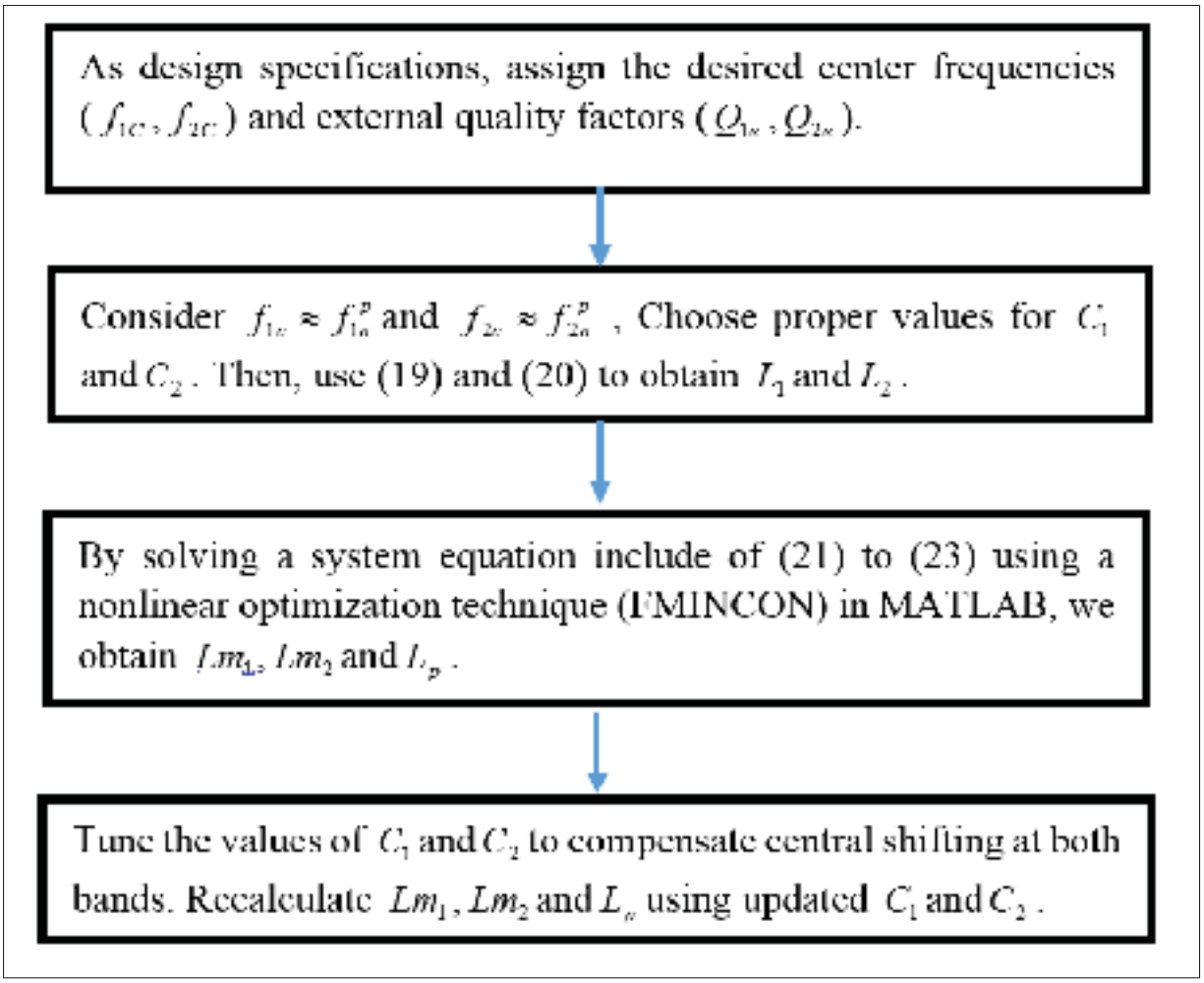

Figure 2.10 Flowchart of synthesis steps for DNBPF design

system equation including (2.23) to (2.25) in MATLAB, the remaining parameters are obtained $L_p = 2.96$ nH, $Lm_1 = 1.121$ nH and $Lm_2 = 0.562$ nH. With the obtained element values, we can compute the frequency responses using (2.9) and (2.10). Dashed lines in Fig.2.11 illustrate the frequency response of the DNBPF circuit model. As can be seen, there is a slight shifting at center frequencies and they are not displayed as expected. These are due to the approximations $f_{1c} \approx f_{1e}^{p}$ and $f_{2c} \approx f_{2e}^{p}$ and can be easily corrected with a slight tuning of the element values C_1= 2.67 pF and C_2= 4.81 pF. The values of L_p, Lm_1 and Lm_2 need to be recalculated to meet the given external quality factors due to updated capacitors. The frequency responses are computed with the updated element values: C_1= 2.67 pF, C_2= 4.81 pF, L_1= 5.36 nH, L_2= 2.02 nH, L_p= 2.564 nH, Lm_1= 1.32 nH and Lm_2= 0.613 nH, as shown in solid lines in Fig.2.11.

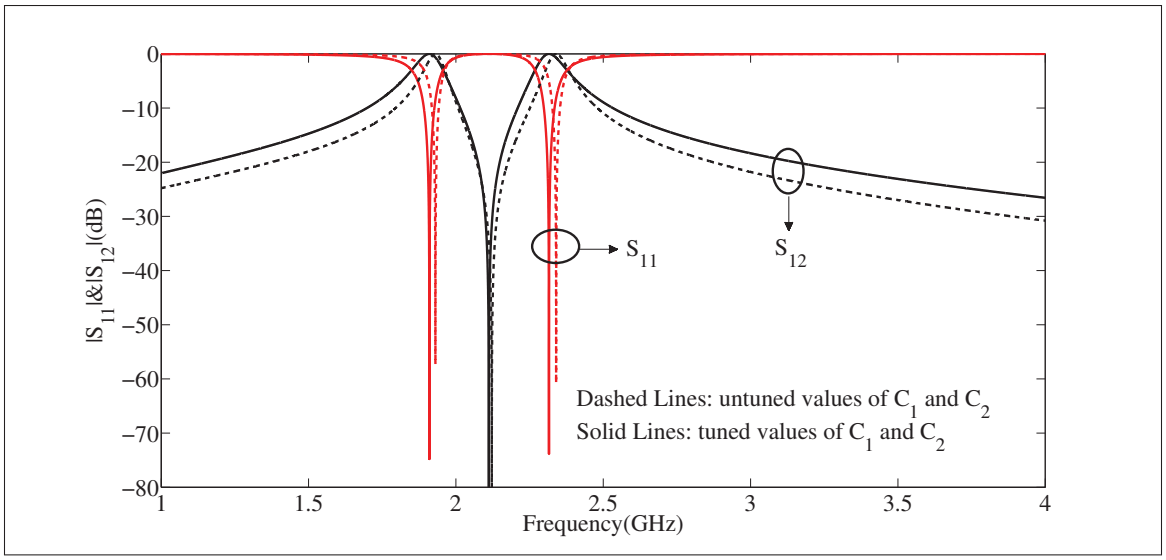

Figure 2.11 Simulated frequency responses of DNBPF circuit model

Table 2.3 Performance Comparison of the DNBPF with Previous Designed dual-band LTCC Filters

Reference	Center Frequency (GHz) f_{1c}/f_{2c}	Return Loss (dB) RL_1/RL_2	Insertion Loss (dB) IL_1/IL_2	FWB_1/FWB_2 %	Number of TZ	Design Method	Size
Lin *et al.* (2014)	2.45/5.25	-12/-16.8	2/2.3	12.2/5.7	2	synthesis	2mm × 1.25mm × 0.9mm
Xu *et al.* (2013)	59.78/61.56	-15/-15	3.6/3.55	2.1/2.2	2	synthesis	——
Oshima *et al.* (2010)	3.96/7.92	<-12	2.5	40/40	3	synthesis	7.5mm × 3.8mm × 0.386mm
Chen *et al.* (2009)	30.3/39.3	-17	4.8	6/6	4	synthesis	4.12mm × 3.92mm × 0.832mm
Chen (2005)	2.4	2.47/5.22	3.15/3.9	8.1/5.7	2	synthesis	2.69mm × 1.77mm × 0.13mm
Pourzadi *et al.* (2019)	0.915/2.45	-18/-22	2/1.5	5.46/5.71	4	synthesis	7.2mm × 6.88mm × 0.56mm
This work	1.9075/2.3125	<-17	1.8	0.26/0.64	1	synthesis	9.3mm × 4.16mm × 0.736mm

Fig.2.12 illustrates a 3-D view of the simulated DNBPF in the HFSS. The thicknesses and numbers of LTCC sheets are the same as those we have used for the design of SNBPF. Fig.2.13 shows the photograph of the fabricated circuit. The final dimensions of the fired filter are 9.3 mm × 4.16 mm × 0.736 mm. The results of the EM simulations and the measurements, are depicted in Fig.2.14. The dashed and solid lines demonstrate the frequency responses of the EM simulations and measurements respectively. The measured insertion losses are around 1.8

dB and the return losses are better than 17dB at both bands. Finally, the measurements show that the transmission zero is located at 2.12 GHz. Finally, in Table 2.3, the performances of several designed dual-band LTCC filters are compared.

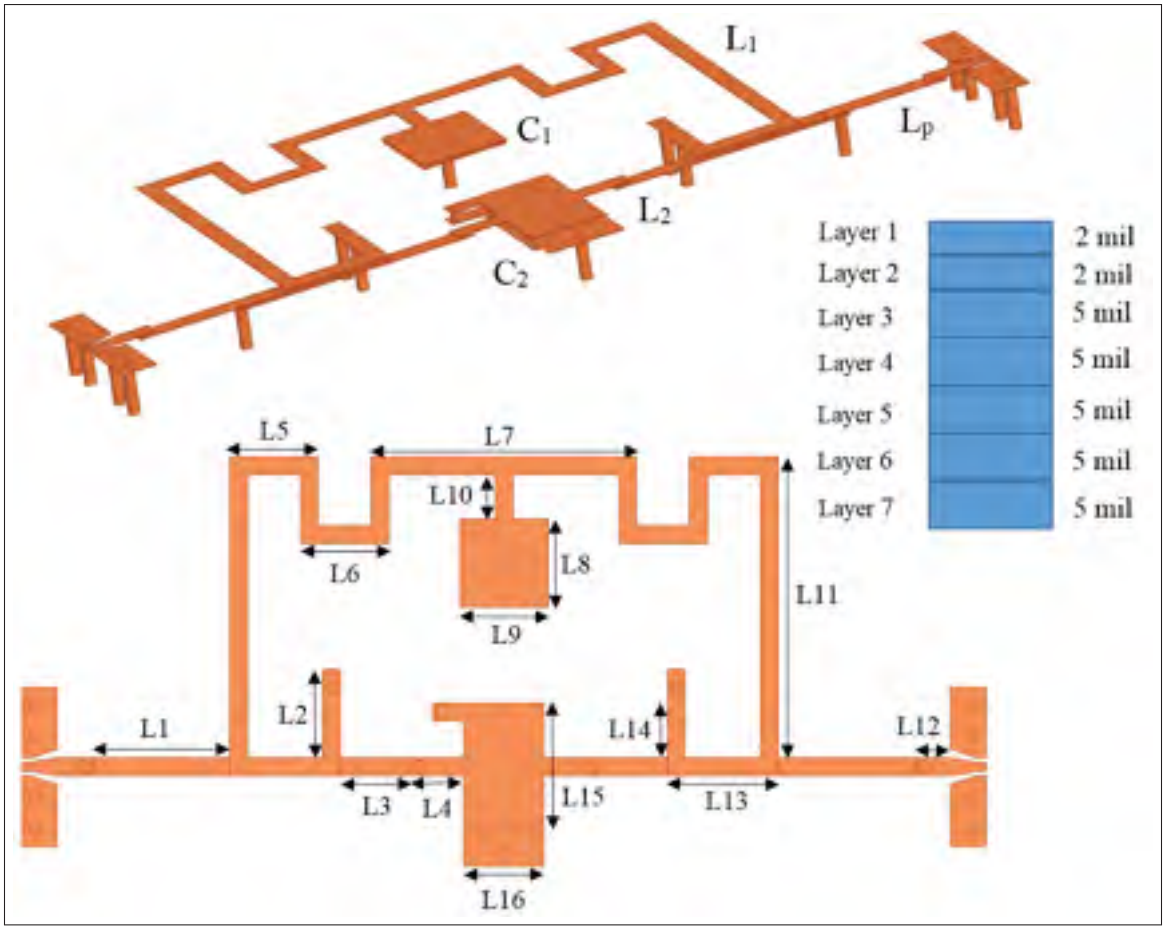

Figure 2.12 3-D view of proposed DNBPF. The dimensions are determined as follows (in millimeter):L1 = 1.55, L2 = 1, L3 = 0.8, L4 = 0.6, L5 = 1, L6 = 1, L7 = 3, L8 = 1, L9 = 1, L10 = 0.5, L11 = 3.14, L12 = 0.4, L13 = 1.25, L14 = 0.5, L15 = 1.44, L16 = 0.9

Conclusion

In this paper, direct synthesis of new single- and dual-band bandpass filters with small FWBs was presented. Using even and odd modes analysis, the nature of frequency responses and the working mechanisms for both topologies were explained. The design procedures used closed-

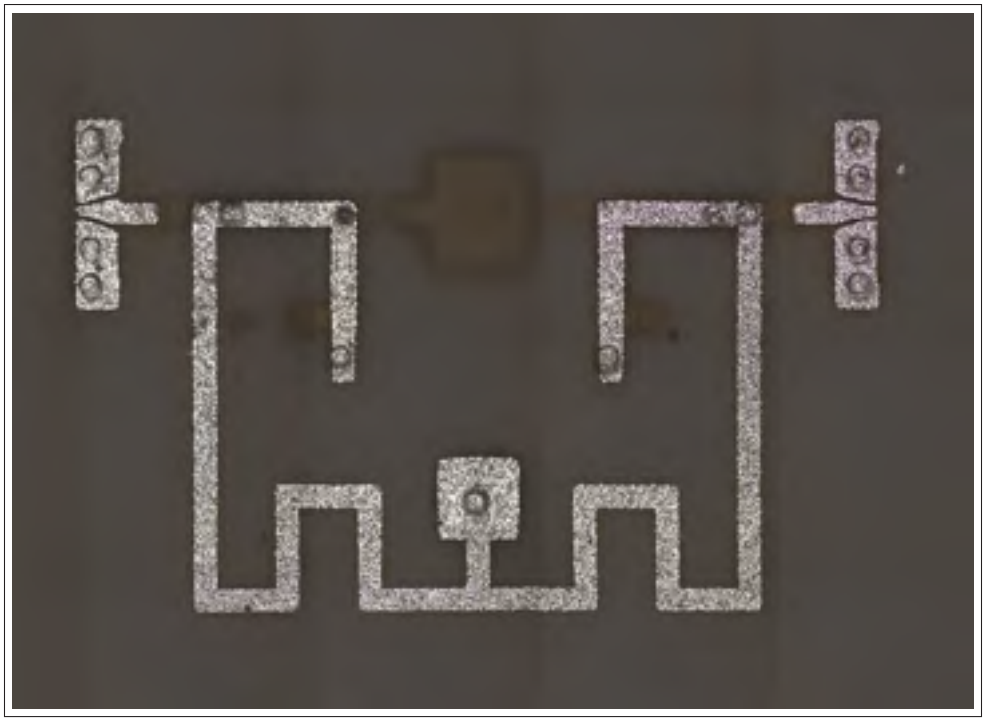

Figure 2.13 Photograph of fabricated DNBPF

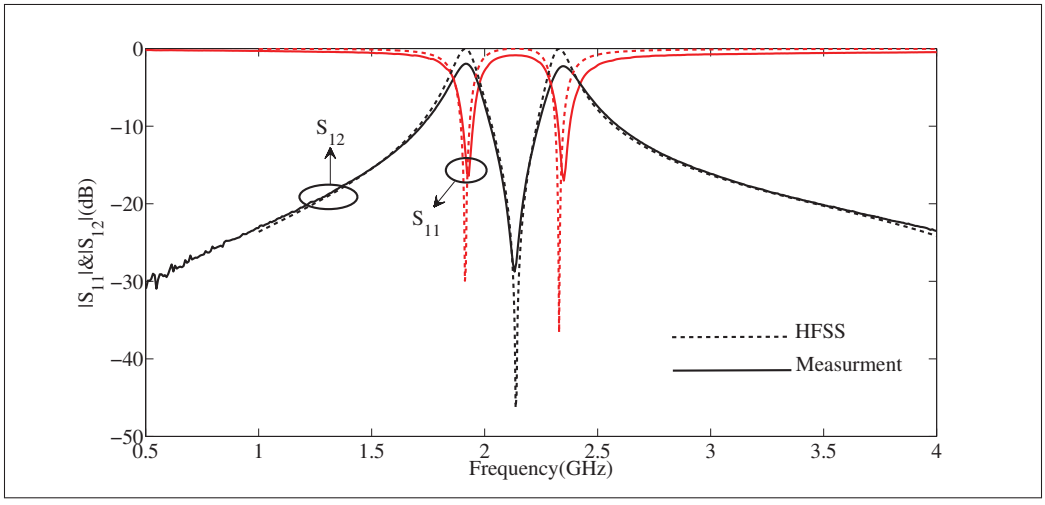

Figure 2.14 EM simulated and measured frequency responses of DNBPF

form equations to calculate the values of network elements for the given center frequencies and bandwidth. The proposed filter topologies and synthesis techniques were applied to the design of an SNBPF and a DNBPF using LTCC technology. The prototypes of these filters

were successfully simulated and measured with excellent agreement between the simulation results and the measurement results.

CHAPTER 3

A FAST TECHNIQUE FOR REALIZATION OF LUMPED-ELEMENTS VALUES INTO 3D PHYSICAL LAYOUT ON LTCC

Aref Pourzadi[1], Arash Adibi[1], Ammar Kouki[1]

[1] Département de Génie Électrique, École de Technologie Supérieure,
1100 Notre-Dame Ouest, Montréal, Québec, Canada H3C 1K3

Manuscript submitted to IEEE Transactions on Components, Packaging and Manufacturing Technology in November 2019.

Abstract

We propose a methodology for the fast translation of ideal lumped-element values to the form of a 3D physical layout using low-temperature co-fired ceramic (LTCC) dielectric. we explain how this approach is implemented without requiring complex formulas and use a simulation-based process which leads to consume less optimization/tuning processing time. The proposed methodology is applied to the design of a dual-band bandpass filter (D-BPF) operating at center frequencies 2.4 GHz, and 5.2 GHz and its layout is realized in the form of 3D physical layout. The two commercial simulators, advanced design systems (ADS) and high-frequency structure simulator (HFSS), are used to simulate ideal lumped-element schematics and perform electromagnetic (EM) simulations on the LTCC layout, respectively.

Introduction

In radio frequency engineering, the physical realization of microwave devices are selected based on features such as operating frequency, size, cost, bandwidth, and loss. Circuits such as filter, couplers, and baluns, can be structured according to one of three commonly used approaches, including distributed transmission lines Zhu & Abbosh (2016); Pourzadi *et al.* (2012), cavities Zhou *et al.* (2018); Shen *et al.* (2013), and lumped-elements Tang (2007); Feng *et al.* (2017). The major drawback of transmission lines and cavities is their bulkiness at lower

frequencies, which creates difficulties in size reduction and integration. Lumped-elements are recommended especially when they are realized in a 3D configuration of low-temperature co-fired ceramics (LTCC) technology. This technology offers a good platform for designing very compact sized devices and multichip modules (McM).

As reported in the literature, many successful lumped-element designs Shafique & Robertson (2011); Shen *et al.* (2009); Mousavi & Kouki (2015); Brzezina *et al.* (2009); Brzezina & Roy (2014); Zheng & Sheng (2017); Zhou *et al.* (2016); Lee *et al.* (2012); Brzezina & Roy (2014) have been fabricated in LTCC. In these references, ideal schematics are analyzed, working mechanisms investigated and then element values are transformed into the physical layouts using an electromagnetic (EM) solver. In the conventional methodology for physical realization, each lumped-element, is designed individually in an EM simulator software. The designed physical elements are combined to form the entire 3D LTCC layout of the proposed circuit, and then the overall dimensions are optimized to obtain the expected frequency responses in the EM simulator. In Brzezina *et al.* (2009), an improved methodology was introduced, which is a hybrid of 3D physical and ideal circuit elements. Hybrid technique is more time-efficient than conventional approach but still includes guesswork in parametric tuning steps. Depending on circuit complexity, the number of elements and operating frequency, tuning steps in both implementation strategies (conventional and hybrid) can be very time-consuming, due to compensation of parasitic effects and mutual coupling between elements. In fact, parasitic effects and mutual couplings can change the inductance and capacitance values of elements, or in the worst case scenario, they can add redundant elements to the proposed ideal model. Also, existing elements with dependent values to each other in the schematic, such as coupled inductors, generate more implementation difficulties Brzezina & Roy (2014).

In this paper, we present a direct methodology by using a correlation strategy between HFSS and ADS simulator softwares. In this technique, the processing time of physical realization is reduced significantly due to the elimination of dimension tuning the steps. This facilitates a better understanding of the existing parasitic effects and provides less efforts to obtain the desired experimental results that are much closer to the ideal model. The usefulness of the proposed

technique is demonstrated through a practical design example, which is a recently published schematic of a lumped-element Dual-Band bandpass filter (D-BPF) Pourzadi *et al.* (2019). To prove the validity of this technique, a physical prototype operating at center frequencies 2.4-5.2 GHz is fabricated in LTCC.

This remainder of the paper is be organized as follows: section 1 describes details of the proposed technique. In, section 2, a design study is defined and the implementation steps related to transforming element values to physical layout are explained using HFSS and ADS simulators. The final simulation and fabrication results are presented in section 3. Concluding remarks are given in section 4.

3.1 Proposed Physical Realization Methodology of Lumped-Elements In LTCC

Fig.3.1 compares the three realization methodologies of LTCC physical layouts in the form of charts, including (a) conventional approach, (b) hybrid methodology and (c) the proposed strategy in this paper, the correlation between HFSS and ADS. As shown in Fig. 3.1, the highlighted steps, the simulation of the ideal schematic and the design of each lumped-element individually are common in the three techniques. In the conventional approach, each lumped-element is designed in an EM simulator and sized based on the given inductance or capacitance values, the high Q-factor and the self-resonance frequency (SRF). The designed physical elements are integrated into one structure to form the complete 3D LTCC layout, and then EM simulations are performed on the structure. The final LTCC layout needs time-consuming parametric tunings on dimensions to obtain the desired results. This approach works for structures with a small number of elements. For the hybrid method, the first two steps are similar to those of the conventional approach. In the integrated layout, some of the physical elements are replaced with ideal values and then the EM parametric tuning is performed on the hybrid layout to adjust the dimension of the physical elements. Once the response is as expected, the ideal element models are replaced with their physical prototypes and a second round of EM physical tuning is performed on the entire 3D LTCC layout. Hybrid method reduces the overall time spent

optimizing rather than the conventional approach, but the increasing number of elements, (see Mousavi & Kouki (2014)) still degrades the functionality of this method.

In our proposed methodology, tuning steps are eliminated. Hence, the time spent in the transformation into physical layout and the efforts required to have a perfect response are both reduced significantly. Also, it provides more convenience and flexibility with respect to implementation of lumped-elements with dependent values, such as coupled inductors. The parasitic effects and mutual couplings are compensated during the simulation steps and accounted in the final results. The outlined steps of the flowchart are explained as follows:

a. The ideal schematic, which we name as schematic I, is simulated in ADS and the S-parameters simulation results are obtained.

b. Each lumped capacitor and inductor is modeled individually in the HFSS, and the variation curves of L, C and Q-factor versus frequency are obtained using equations 3.1 to 3.3 Brzezina *et al.* (2009).

$$L = \frac{Im(Z_{11})}{\omega} \tag{3.1}$$

$$C = \frac{Im(Y_{11})}{\omega} \tag{3.2}$$

$$Q = \frac{Im(Z_{11})}{Re(Z_{11})} \tag{3.3}$$

The elements are sized physically to meet the given inductance or capacitance values at the operating frequency while simultaneously providing the maximum value of the Q-factor and a high SRF. High Q-factor is demanded in circuit design as it has a substantial influence on the in-band insertion loss.

c. Interconnect the designed physical elements with their initial dimensions to form the entire 3D LTCC layout in the HFSS. It is required to have a preliminary idea about number of stack layers and the placement configuration of elements. With the completion of the first round of EM simulation in the HFSS, as we had expected, there are dissimilarities between the obtained EM and the ideal model (schematic I) S-parameters in the ADS.

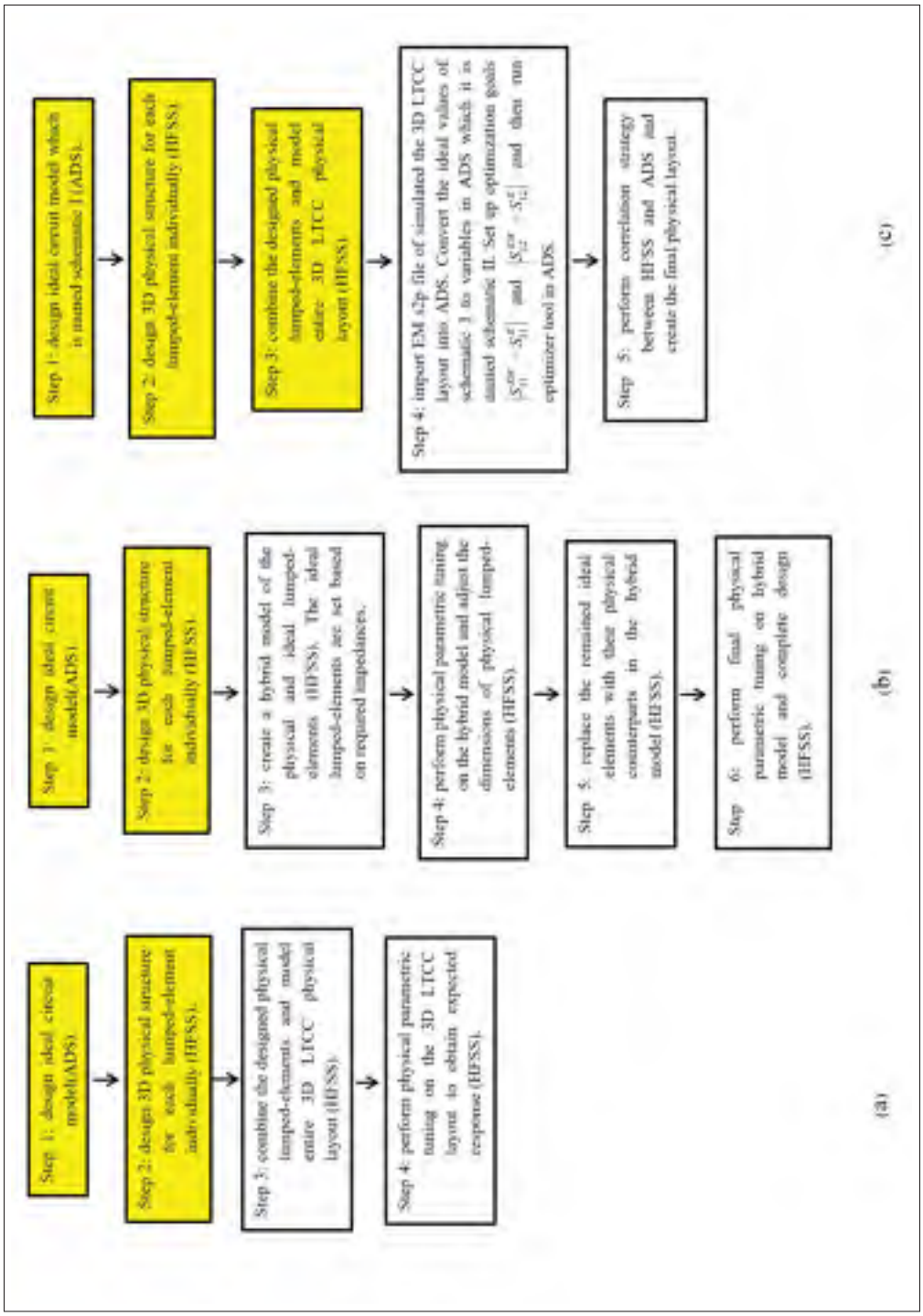

Figure 3.1 Flow charts of three realization strategies including: (a) conventional approach (b) hybrid methodology (c) proposed correlation strategy between HFSS and ADS

d. This step entails finding the values of elements which are corresponded to the initial 3D LTCC layout. Fig .3.2 illustrates the simulation procedures for this step in the ADS environment. The obtained EM s-parameters S_{11} and S_{12} (in previous step) are imported into the ADS in the form of an S2P file. The elements of the ideal model (schematic I) are replaced with the variable elements and the new network is named schematic II. Then, using Optim and Goal tools, the optimization process is set up. In the Optim window, the type of optimizer and the number of iterations are selected. In the Goal window, we define two expressions as final targets, which are $|S_{11}^{EM} - S_{11}^{II}|$ and $|S_{12}^{EM} - S_{12}^{II}|$, and add limit criteria 0 for both expressions to stop the solver. The superscripts EM and II indicate imported EM and schematic II S-parameters, respectively. Running the optimization solver, the optimizer computes element variables in each iteration to meet the limit criteria of the defined expressions in the Goal windows. The optimizer compares the obtained frequency responses of schematic II with the imported S2P file and then modifies the values of elements in next iteration to minimize the design goal errors. Note that assigning reasonable concentrations on element values would reduce the convergence time of the optimizer.

e. In the previous step, the values of schematic II were computed such that the frequency responses of the network was matched perfectly with the EM frequency responses of the initial 3D LTCC layout. In this step, the target is to modify the values of schematic II elements and, consequently, the physical dimensions of elements of the initial 3D LTCC layout to meet the frequency responses of schematic I. We proceed with this approach with the following strategy. In the ADS environment, we select one of the elements of schematic II and replace its value with the value of the same element from schematic I. Then, s-parameter simulation is performed on the modified schematic II. Note that in the modified network, the rest of elements are the same as we had computed in the step 4. Next, in the HFSS, the dimensions of corresponding element are resized such that the EM frequency responses follow the frequency responses of the modified schematic II. Repeating the above mentioned details, all the remaining elements of modified schematic II are replaced with the values of schematic I, in turn. Consequently the physical elements

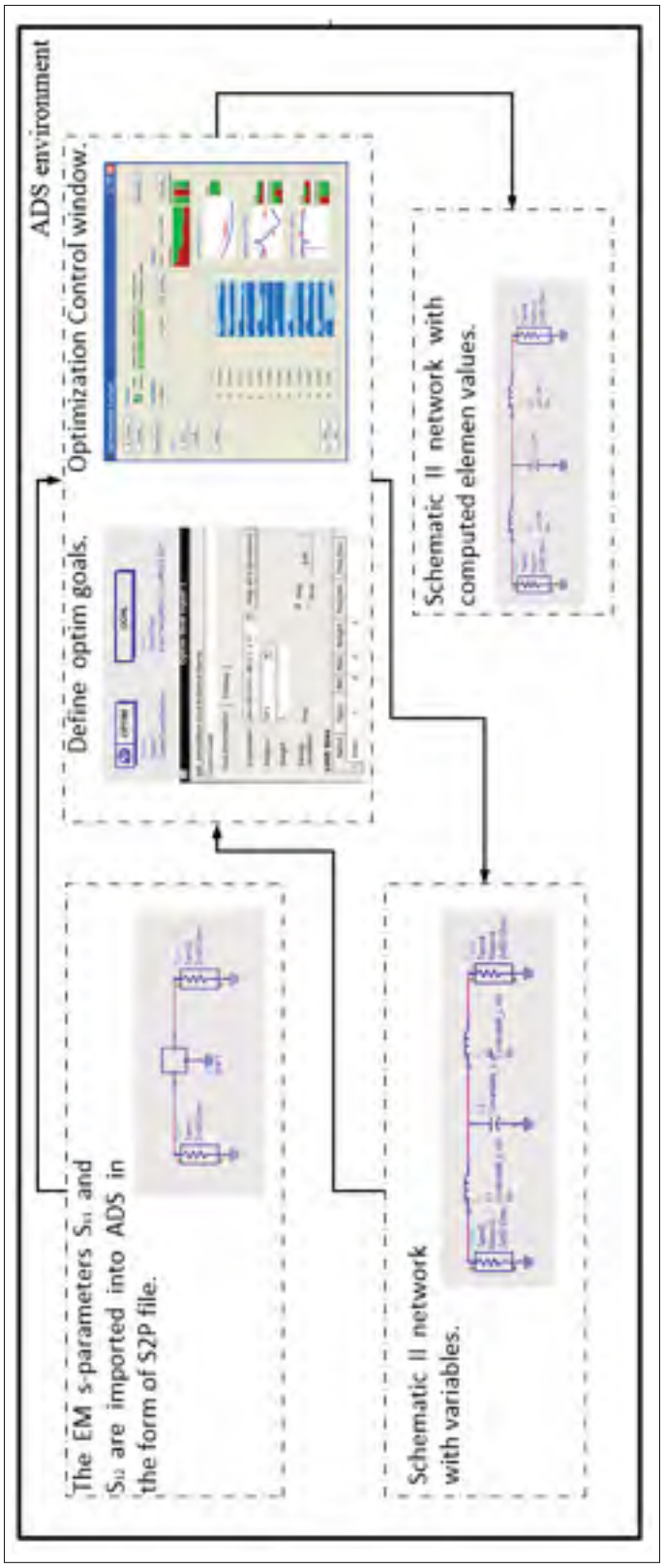

Figure 3.2 Simulation procedures in step 4

of the 3D LTCC layout are resized, which leads to an excellent agreement between the simulation results of layout and schematic I.

3.2 Circuit Realization Example

This section illustrates the application of the proposed methodology to the transformation of an ideal circuit model of a dual-band bandpass filter (D-BPF), presented in reference Pourzadi *et al.* (2019), into a 3D LTCC layout. Using the synthesis procedure of Pourzadi *et al.* (2019), the element values of the circuit model are computed to design and create a prototype D-BPF operating at center frequencies 2.45 GHz and 5.2 GHz. Following the steps outlined in the previous section, we proceed to realize the element values into a physical layout in LTCC, as follows.

a. Fig.3.3a shows the schematic (schematic I) of the D-BPF, which consists of 13 elements with the computed values of $C_c = 0.68$ pF, $C_z = 0.2$ pF, $C_1 = 1.69$ pF, $C_2 = 1$ pF, $L_1 - Lm_1 = 1.04$ nH, $L_2 - Lm_2 = 1.5$ nH, $Lm_1 = 0.02$ nH, $Lm_2 = 0.29$ nH. Fig. 3.3b illustrates the simulated s-parameters of the Schematic I in the ADS.

b. Using HFSS, each of the elements are individually sized to meet given inductance or capacitance at 2.4GHz frequency. At this point, we have no idea about the final configuration of the D-BPF including number of dielectric sheets and placement of the elements in the layout. Thus, simplest forms of realizations are selected to find initial physical dimensions. We chose to realize capacitors and inductors using multilayer parallel plates and straight lines respectively. The elements are simulated using two sheets of LTCC Ferro A6M dielectric, with the thickness of each 93.98 um, dielectric constant of 5.9 and the loss tangent of 0.002. Figs. 3.4 shows the characteristic variations of the elements versus frequency, simulated in the HFSS, and Table 3.1 lists the physical dimensions, the Q-factor and the SRF values. It should be noted that the simulation characteristics of the element Lm_1 are not provided, due to its small value (0.02 nH) and are physically realized by a single via.

c. We interconnect the elements designed in step 2 to form the entire D-BPF in the HFSS, as shown in Fig.3.5. The filter is simulated using five layers of green tapes with an overall thickness of 469.9 um, 8-um thick silver and silver-filled 136-um-diameter vias. First round of EM simulation are performed on the layout and the S-parameters are obtained. Solid lines in Fig. 3.6 illustrates the frequency responses of the proposed D-BPF layout, with initial physical dimensions. Note that, the interconnections between elements which are not included in the ideal schematic, generate parasitic effects and unwanted mutual couplings. In addition to these negative impacts, the dielectric and conductor losses cause disagreements between the frequency responses of the final LTCC layout and the ideal circuit model.

Table 3.1 List of designed elements and their characteristics.

Element	$L_1 - Lm_1$ = 1.04 nH	$L_2 - Lm_2$ = 1.5 nH	Lm_2 = 0.29 nH	C_1 = 1.69 pF	C_2 = 1 pF	C_z = 0.2 pF	C_c = 0.68 pF
SRF (GHz)	13.4	9.33	51	6.61	8.64	44.61	10.68
Q-Factor	106	102	97	50	55	63.7	58
Dimension (mm)	$l_{L1} = 2.6$	$l_{L2} = 3.7$	$l_{Lm2} =$ 0.75	$l_{C1} = 1.4$	$l_{C2} = 1.1$	$l_{Cz} = 0.5$	$l_{Cc} = 0.9$
	$W_L = 0.2$	$W_L = 0.2$	$W_L = 0.2$	$W_{C1} =$ 1.4	$W_{C2} =$ 1.1	$W_{Cz} =$ 0.5	$W_{Cc} =$ 0.9

Table 3.2 Comparison table of Schematic I and Schematic II element values.

Elements	$L_1 - Lm_1$ (nH)	$L_2 - Lm_2$ (nH)	Lm_2 (nH)	Lm_1 (nH)	C_1 (pF)	C_2 (pF)	C_z (pF)	C_c (pF)
Schematic I	1.04	1.5	0.29	0.02	1.69	1	0.2	0.68
Schematic II	0.63	1.87	0.41	0.038	4.15	0.94	0.39	1.06

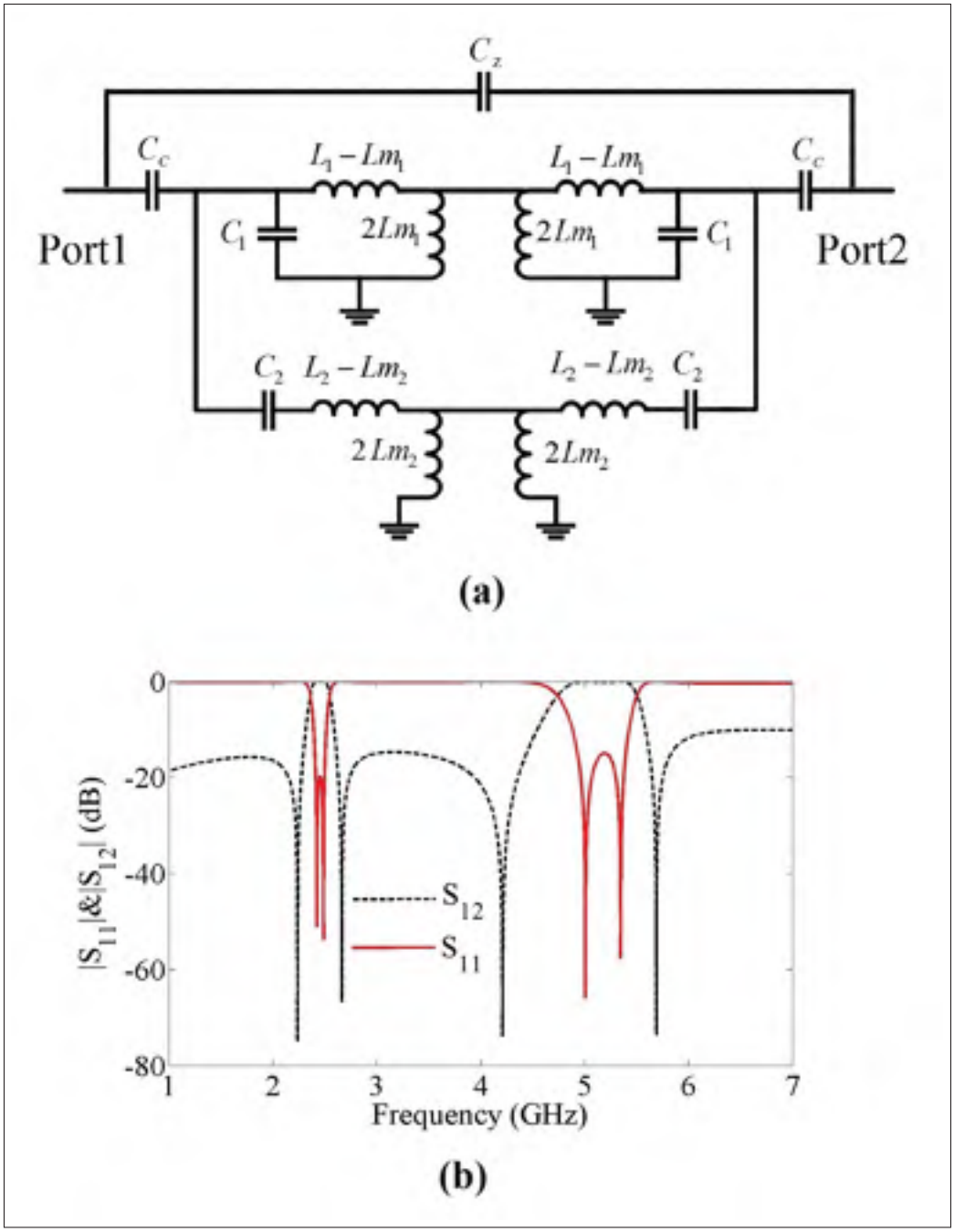

Figure 3.3 a) Schematic I Pourzadi *et al.* (2019) b) Simulated frequency responses of Schematic I in ADS

d. Performing EM simulation on the initial D-BPF layout in the HFSS, the obtained s-parameters S_{11}^{EM} and S_{12}^{EM} are extracted in the form of touchstone file. Then, we select two port s-parameter item in the ADS and import the touchstone data. Next, in the ADS

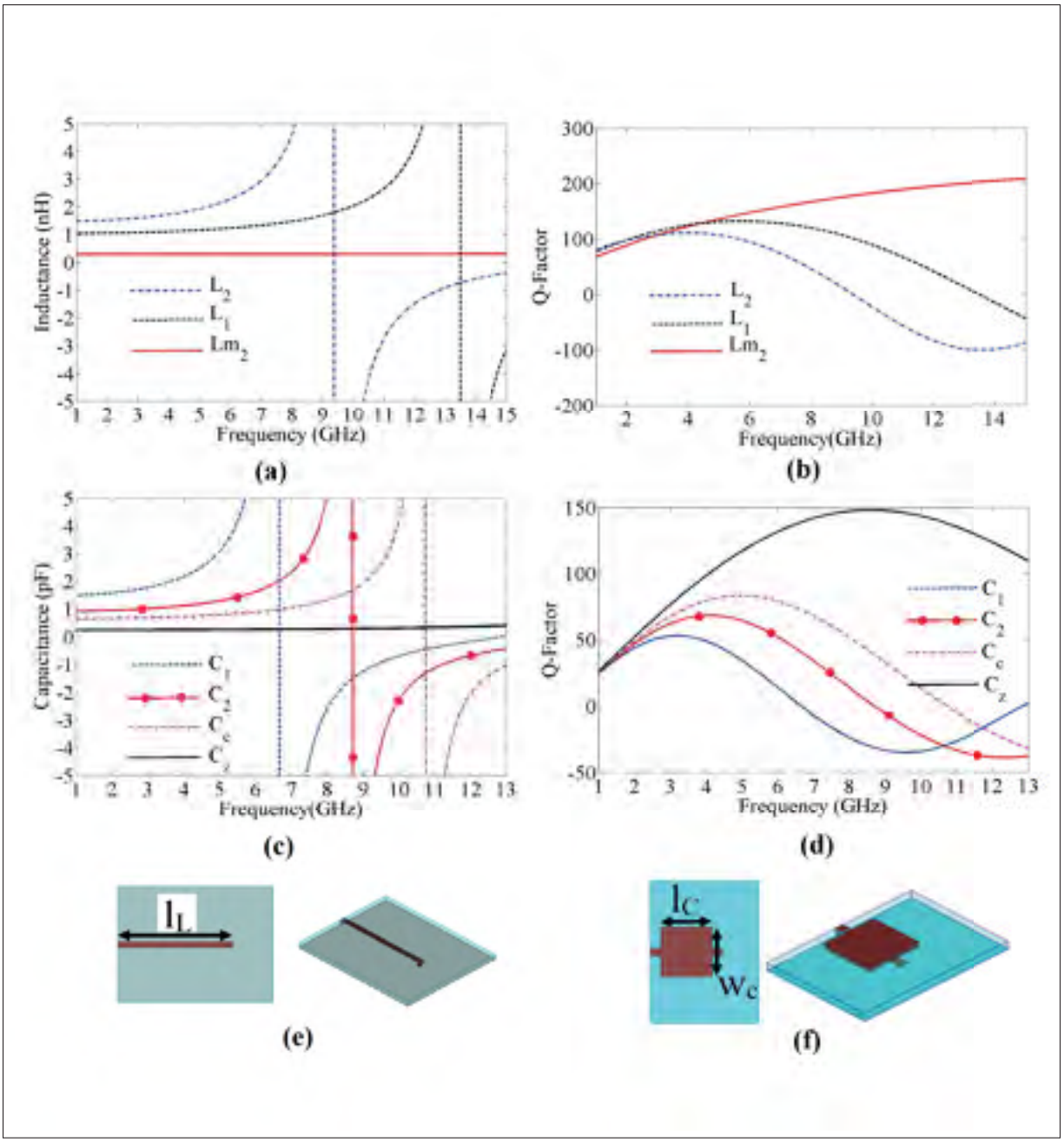

Figure 3.4 Simulated characteristics of elements in the HFSS a) simulated inductances of L_1, L_2 and Lm_2 versus frequency b) simulated Q-factors of L_1, L_2 and Lm_2 versus frequency c) simulated capacitances of C_1, C_2, C_z and C_c versus frequency d) simulated Q-factors of C_1, C_2, C_z and C_c versus frequency e) top view and 3D view of straight line inductor f) top view and 3D view of parallel plate capacitor

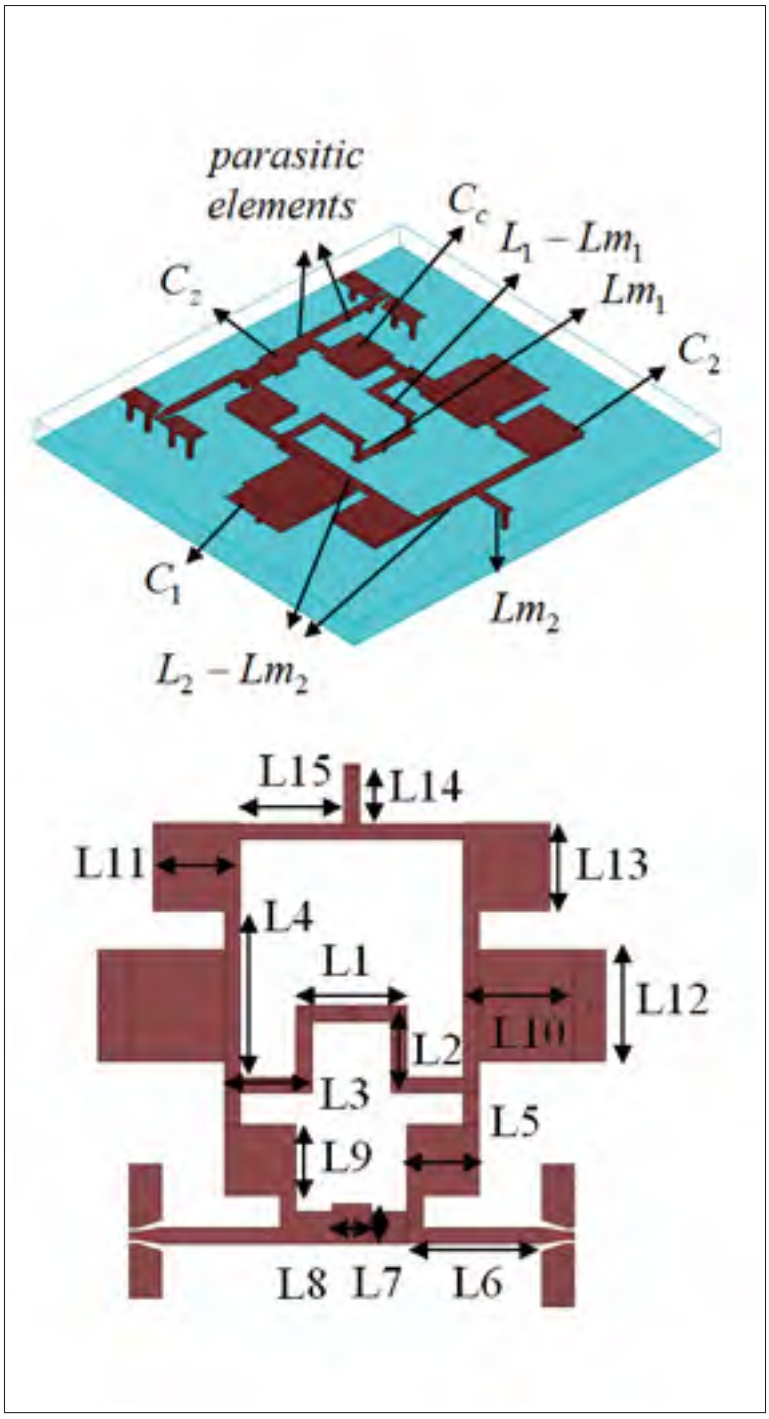

Figure 3.5 3D and top views of structured initial EM circuit in HFSS. Dimensions are in millimeters, L1=1.4, L2=1.1, L3=1.1, L4=2.3, L5=0.9, L6=1.5, L7=0.5, L8=0.5, L9=0.9, L10=1.4, L11=1.1, L12=1.4, L13=1.1, L14=0.75, L15=1.3, width of lines=0.2

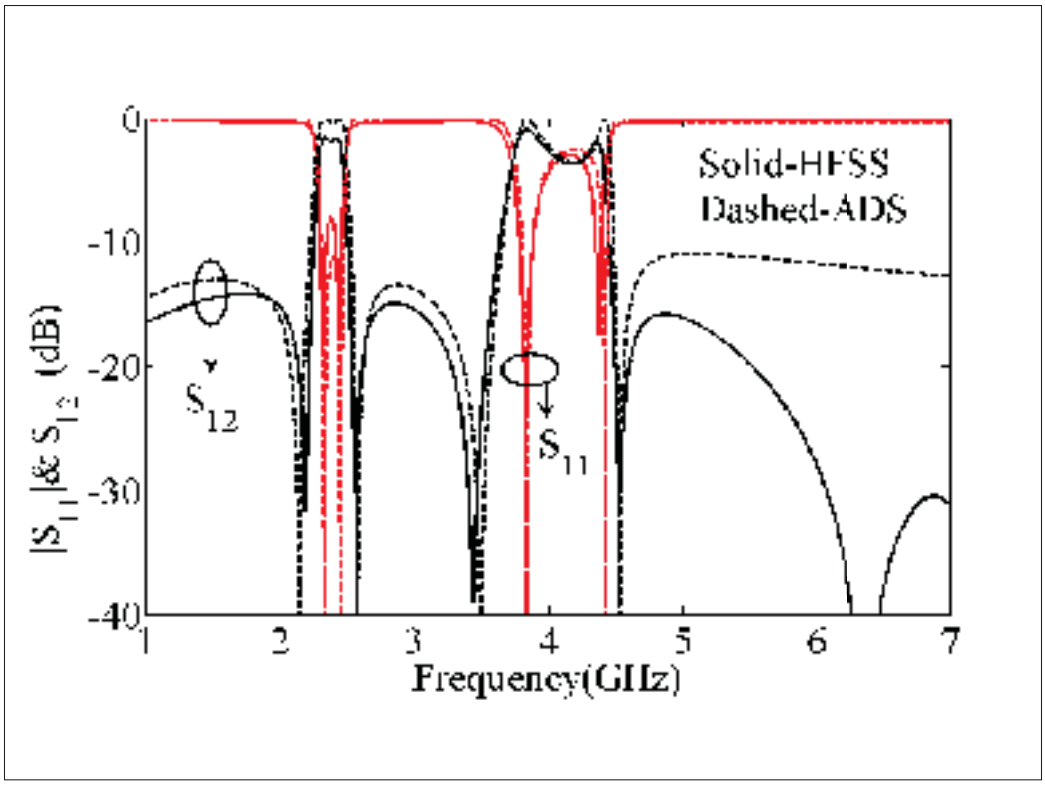

Figure 3.6 Simulated frequency responses, solid line: initial EM circuit and Dashed line: Schematic II

environment we set up the optimization controller, select type of optimizer to gradient with maximum 6000 iterations, and define goal expressions $|S_{11}^{EM} - S_{11}^{II}|$ and $|S_{12}^{EM} - S_{12}^{II}|$. The optimizer starts calculation process of Schematic II elements and provides an error criterion in the form of number for estimation of differences between the computed frequency responses of Schematic II and touchstone file. In this D-BPF layout realization, the optimization process is converged to the minimum value of error number 25 after 6000 iterations. Fig.3.6 shows an excellent agreement between the S-parameters of Schematic II and D-BPF LTCC layout which demonstrates the Schematic II is an accurate circuit model for the initial layout. Table 3.2 lists the element values of Schematic I and II. It should be mentioned that due to existing mutual couplings, loss effects and interconnections, the optimizer cannot provide error number close to 0 but convergence to small values guarantees good agreement between the final results.

e. In this step, the target is to modify the dimensions of the elements of D-BPF to obtain the final filter layout. To proceed with this approach, HFSS and ADS are used simultaneously. As shown in Fig.3.7a, C_1 in the schematic II is replaced with the corresponding element from Schematic I, to 1.69 pF. S-parameter simulation on the Schematic II is then carried in ADS, whereas the values of the other elements remain as detailed in Table 2.2. Dashed lines in Fig.3.7b illustrate the frequency responses of modified Schematic II. In the HFSS, the physical dimensions of element relevant with C_1 is resized such that the EM S-parameters, solid lines, follow the simulated frequency responses of the modified Schematic II (dashed lines, as shown in Fig. 3.7b). Next, we fix the value of C_1 in the Schematic II to 1.69pF and replace the second element $L_1 - Lm_1$ to 1.04 nH, as depicted in Fig.3.8a. Fig.3.8b compares the S-parameters between the two EM-simulated and modified network. The same trend is repeated, in turn, for the all elements of Schematic II and the simulation results are provided, (see Figs.3.9 to 3.13). Finally, this approach leads to an excellent agreement in the frequency responses between the D-BPF layout and Schematic I, as shown in Fig. 3.13b.

3.3 Fabrication and Simulation Results

This section presents prototyping of synthesized D-BPF in the targeted fabrication technology, LTCC Ferro A6M. Fig.3.14 shows the D-BPF layout with the modified dimensions of elements modeled in the HFSS, and a photograph of the fabricated D-BPF layout is shown in Fig.3.15. The final dimensions of the fired filter are 2.5mm $\times$ 3.5mm $\times$ 2.5mm. Fig.3.16 shows the EM-simulated and measured S-parameters of the LTCC D-BPF. The agreement between the two is found to be excellent. The D-BPF displays a 2 dB measured insertion loss for the first band, 1 dB insertion loss for the second band and more than -15 dB return loss for both bands. As can be seen in the Fig.3.16, the center frequencies as well as the transmission zeros are slightly shifted from the desired values due to fabrication tolerance. The filter shows less insertion loss at the second passband, which is a result of a higher value of the Q-factor for the lumped-elements at upper frequencies. It is worth noting that the physical capacitors and

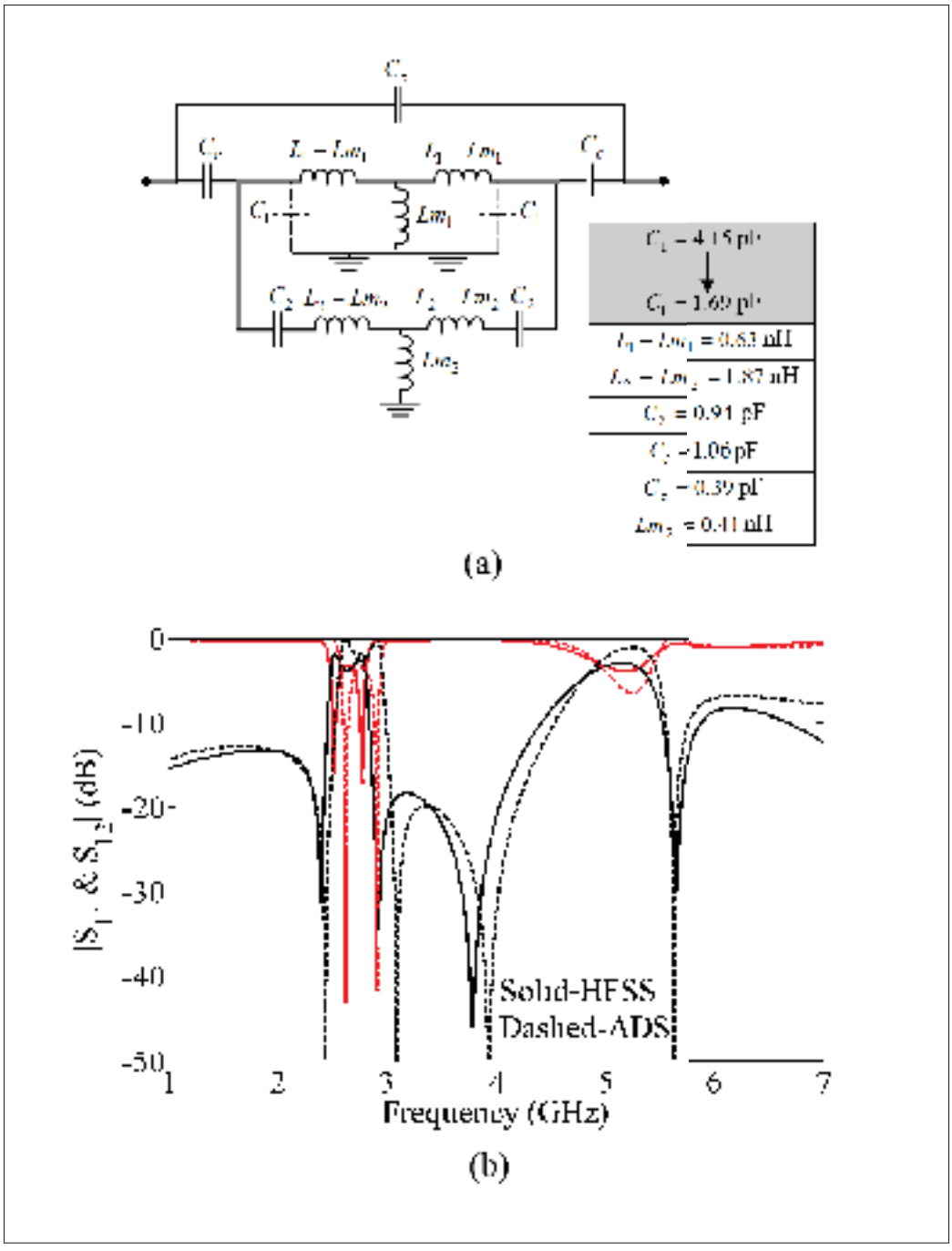

Figure 3.7 a) The value of C_1 from Schematic II is replaced with the corresponding value from schematic I; b) Simulated frequency responses in the HFSS and ADS

inductors do not operate like ideal lumped-elements at frequencies higher than their SRF. Thus,

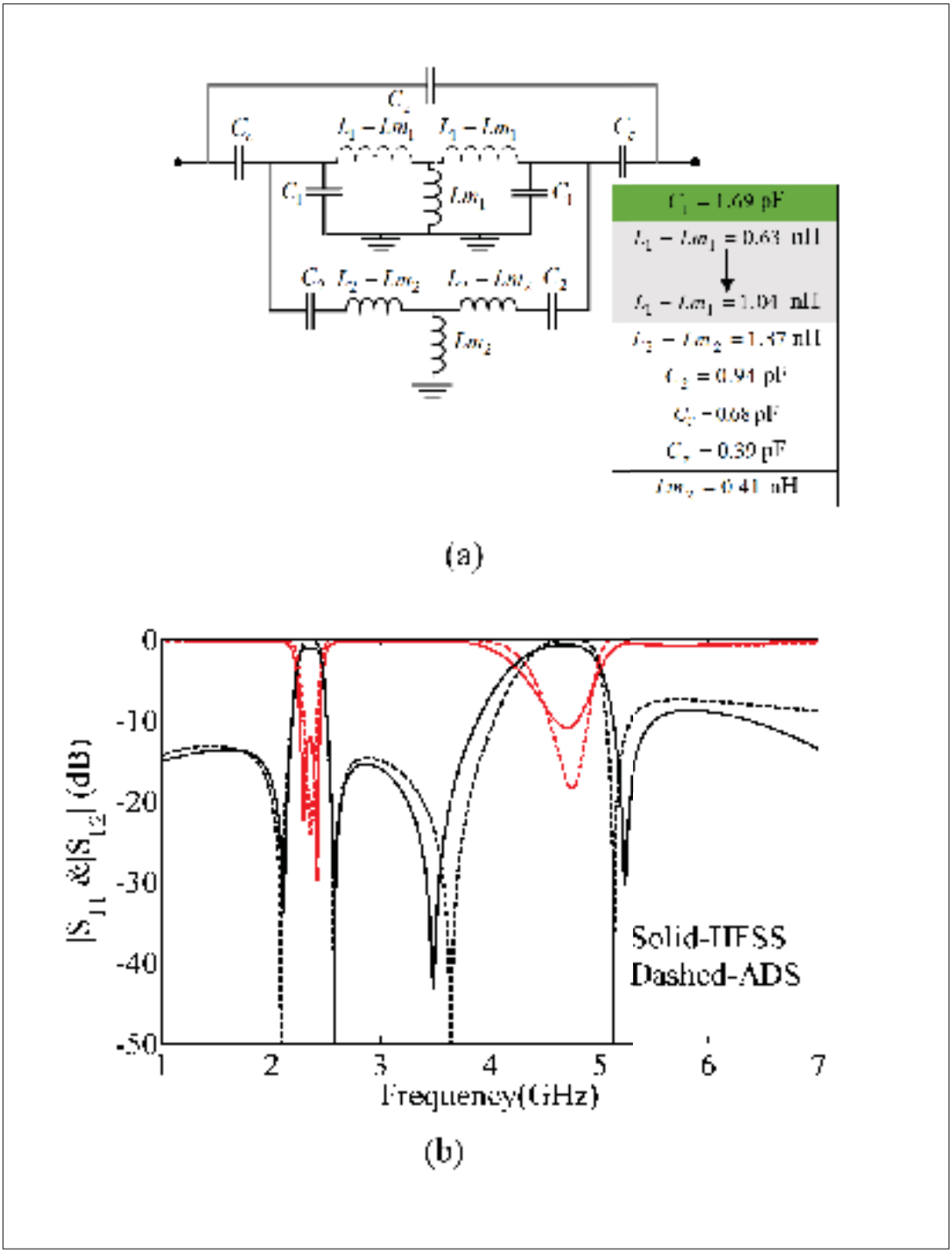

Figure 3.8 a) The values of C_1 and $L_1 - Lm_1$ from Schematic II are replaced with the corresponding values from Schematic I; b) Simulated frequency responses in the HFSS and ADS

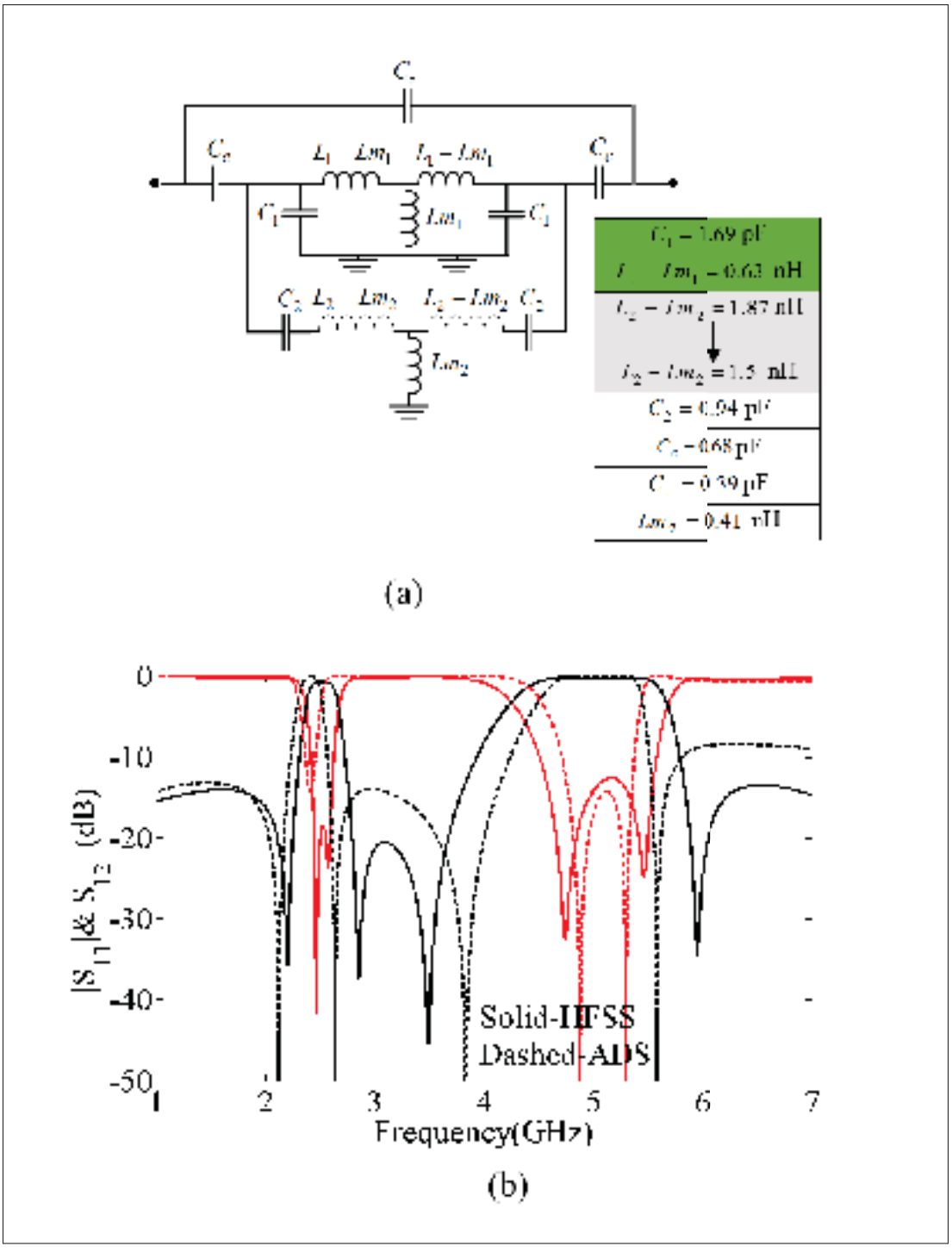

Figure 3.9 a) The values of C_1, $L_1 - Lm_1$ and $L_2 - Lm_2$ from Schematic II are replaced with the corresponding values from Schematic I; b) Simulated frequency responses in the HFSS and ADS

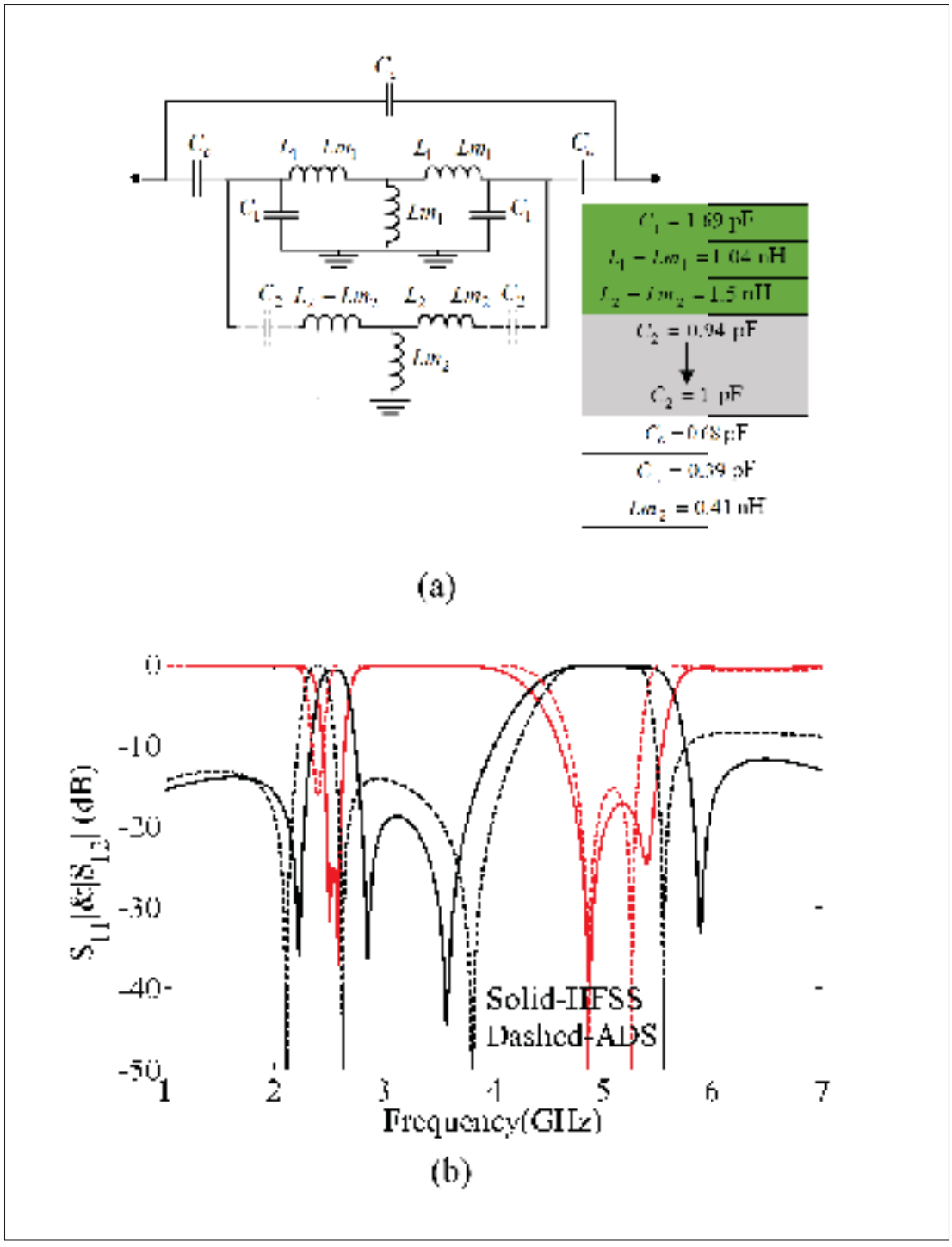

Figure 3.10 a) The values of C_1, $L_1 - Lm_1$, $L_2 - Lm_2$ and C_2 from Schematic II are replaced with the corresponding values from Schematic I; b) Simulated frequency responses in the HFSS and ADS

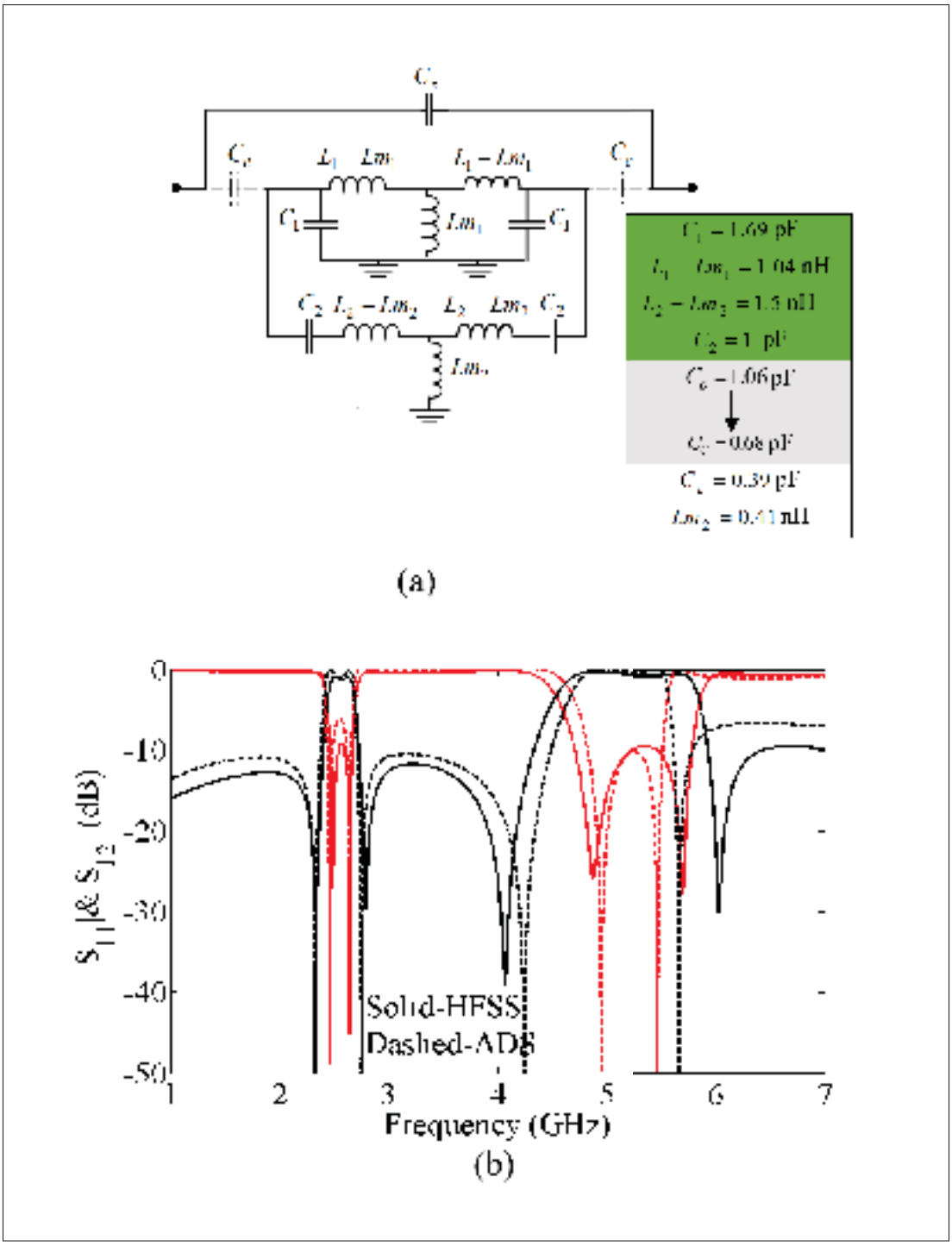

Figure 3.11 a) The values of C_1, $L_1 - Lm_1$, $L_2 - Lm_2$, C_2 and C_c from schematic II are replaced with the corresponding values from Schematic I; b) Simulated frequency responses in the HFSS and ADS

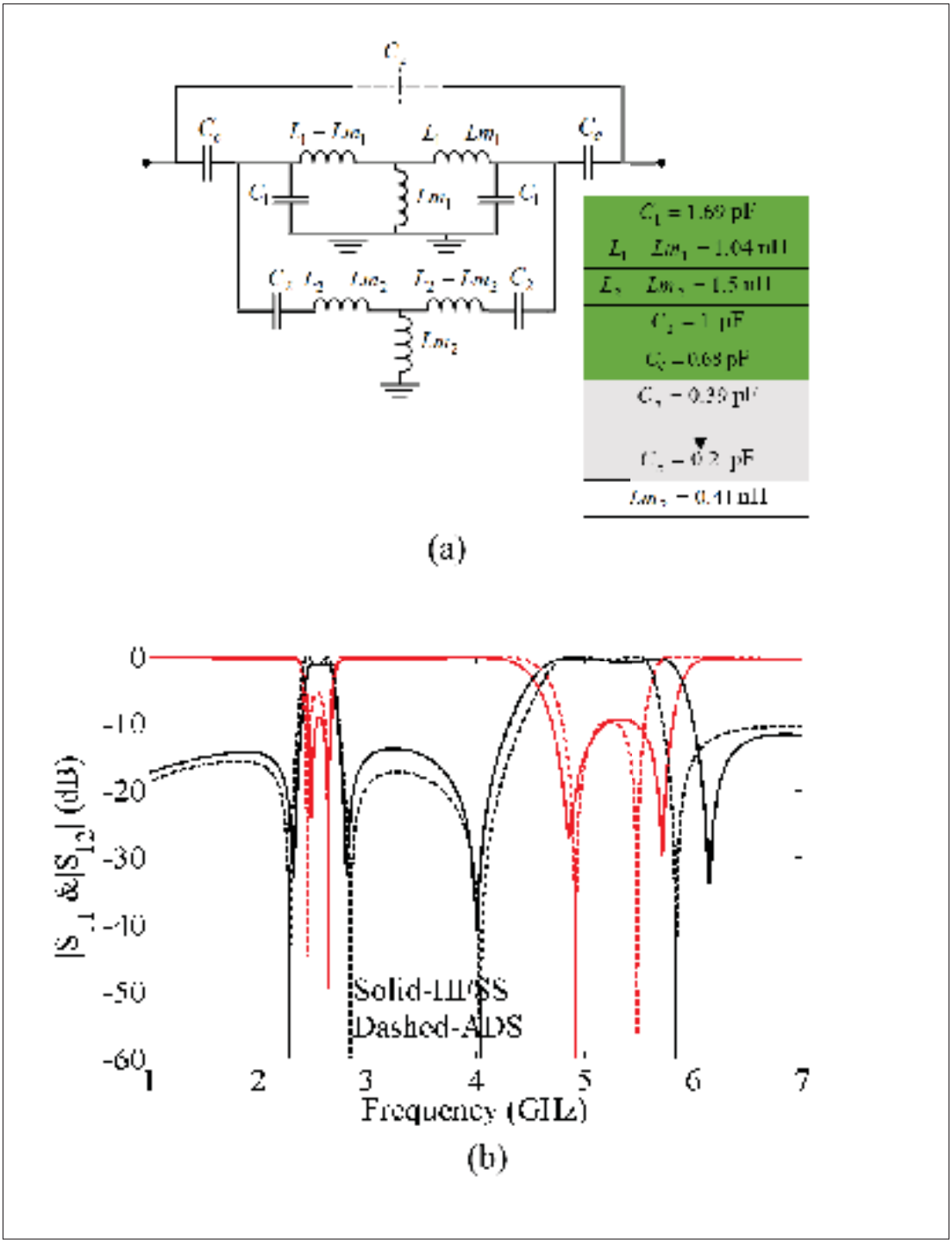

Figure 3.12 a) The value of C_1, $L_1 - Lm_1$, $L_2 - Lm_2$, C_2, C_c and C_z from Schematic II are replaced with the corresponding values from Schematic I; b) Simulated frequency responses in the HFSS and ADS

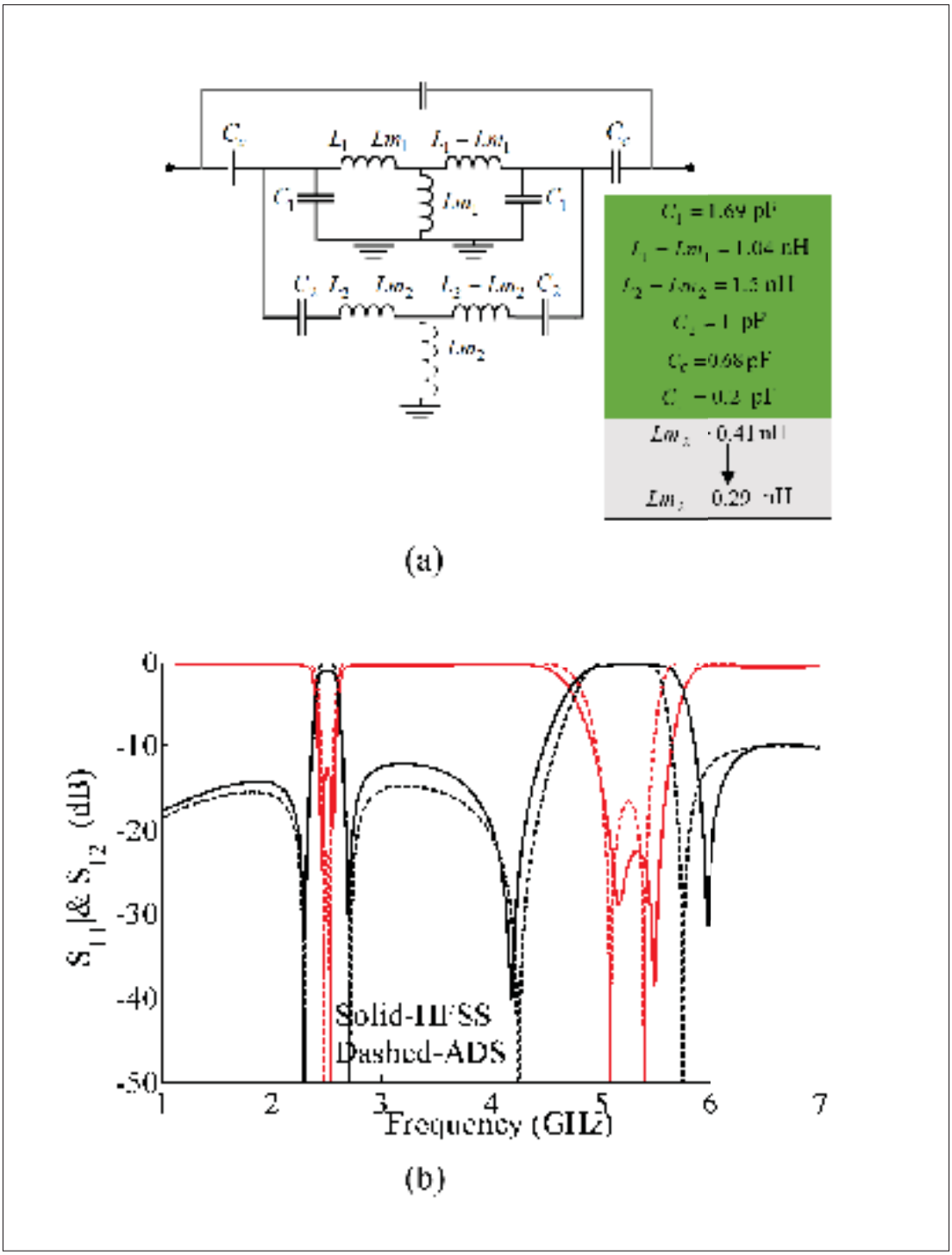

Figure 3.13 a) The value of C_1, $L_1 - Lm_1$, $L_2 - Lm_2$, C_2,C_c, C_z and Lm_2 from Schematic II are replaced with the corresponding values from Schematic I; b) Simulated frequency responses in the HFSS and ADS

the simulated s-parameters of layout do not follow the same pattern of those curves which are obtained from ideal schematic simulations.

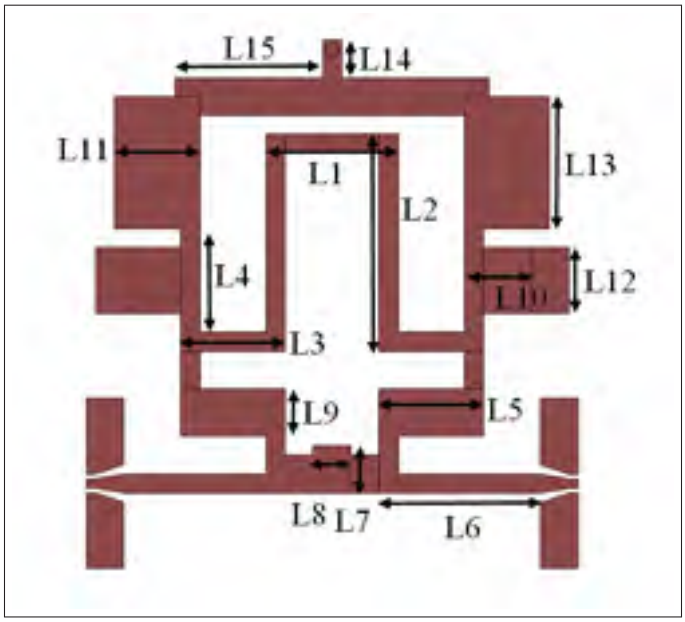

Figure 3.14 Top view of modified D-BPF layout, dimensions are in millimeter, L1=1.4, L2=2.3, L3=1.1, L4=1.3, L5=1.1, L6=1.7, L7=0.5, L8=0.4, L9=0.5, L10=0.7, L11=0.9, L12=0.7, L13=1.4, L14=0.4, L15=1.56, width of lines=0.2

3.4 Conclusion

This paper has presented a fast realization methodology for transforming ideal lumped-elements into a physical 3D LTCC layout. The entire physical realization process is explained in five steps, which eventually leads to an excellent agreement between the S-parameters of the ideal schematic and the layout. In this methodology, elements are designed individually and combined entirely in the HFSS, and then, using a correlation strategy between HFSS and ADS the final sizes are obtained. The main advantage of this technique is elimination of optimization and the dimension tuning of physical elements, which reduces the time of layout realization significantly. The proposed methodology is validated through a practical example. Schematic of a dual-band bandpass filter operating at center frequencies of 2.4-5.2 GHz was layouted and fabricated on an LTCC ferro A6M dielectric. LTCC was selected as a good platform for cir-

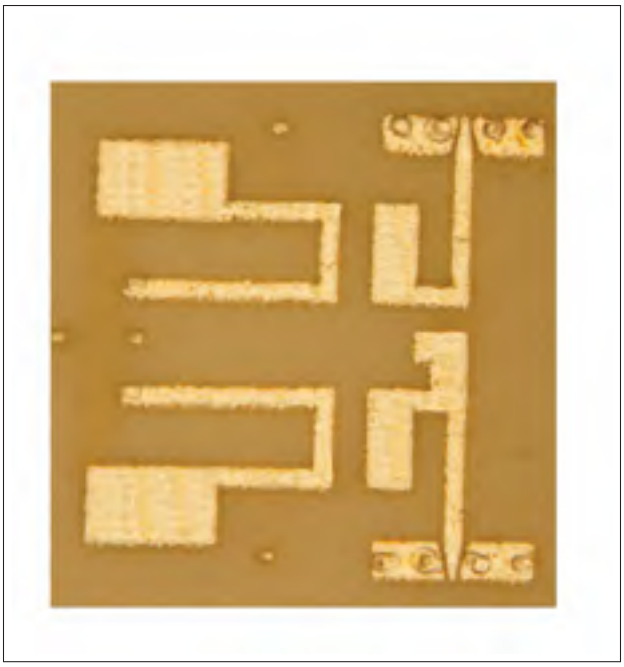

Figure 3.15 Photo of fabricated D-BPF

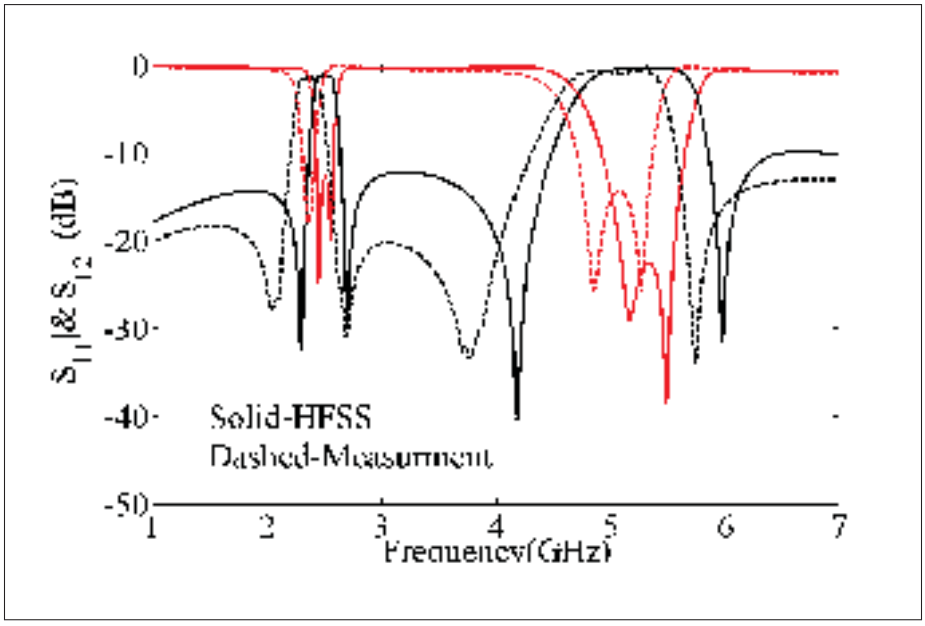

Figure 3.16 Simulated and measured frequency responses of designed D-BPF

cuit realization due to its significant properties. The EM-simulated and measured s-parameter results validates the proposed technique.

CONCLUSION AND RECOMMENDATIONS

The size of filters and dual-band functionality can make a significant impact on dual-band wireless communication by replacing bulky conventional and two parallel single filters. Also, existence of synthesis procedures make easier physical circuit realizations for various demanded microwave applications. Some features like low in-band insertion loss, good out of band rejections and acceptable return loss must be included as design considerations.

In response to the above needs, we developed novel miniaturized dual-band second order and narrowband filter architectures in the context of lumped-element LTCC bandpass filters. In addition to high performance, we investigated the circuit realization methodologies and presented the relevant design closed-form equations.

In the first part of this research, a novel topology of lumped-element dual-band bandpass filter was introduced. The working mechanism and nature of existing dual-band response were explained mathematically. With the aid of developed design procedure and closed-form equations, three design example operating at frequencies 0.9-2.4GHz, 2-3GHz and 0.8-5 GHz were presented and the values of elements calculated. The design procedure was validated by fabricating 0.9-2.4GHz prototype in 5 layers LTCC dielectric. The simulation and measurement results were provided and compared. The measured in-band insertion loss was less than 2 dB, for the first band, and less than 1.5 dB, for the second band. The measured return loss was better than 18dB, for the first band, and better than 22 dB, for the second band. Good out of band rejection were obtained due to the presence of four transmission zeros located at 0.72, 1.1, 1.9 and 2.92 GHz.

In the second part, we introduced the new schematics of single- and dual-band bandpass filters for narrowband applications, realized in LTCC. Similar to the first part, the design procedures were provided for various filtering specifications. The single- and dual-band filters improve out of band rejection by generating two and one transmission zeros respectively. A design

example of single bandpass filter operating at frequency 2.2925-2.3325 GHz were provided and fabricated in 7 layers LTCC dielectric. The filter shows 2 dB in-band insertion loss and return loss better than 18 dB. The two transmission zeros appear at both sides of passband and located at 2 and 2.71 GHz frequencies. A design prototype of dual-narrow bandpass filter was designed whereas the passbands were centered at 1.905-1.910 GHz and 2.305-2.320 GHz and realized in 7 layers LTCC dielectric respectively. The measured insertion losses are around 1.8 dB and return losses are better than 17dB at both bands. The filter generates one transmission zeros between two passband at 2.1GHz frequency.

In the third part, a methodology was presented for transforming of lumped-element values from schematics into physical layouts. The methodology eliminated time consuming electromagnetic simulations- optimizations and provided a fast solution for obtaining the final results. The methodology was started by designing elements individually, and then the elements were interconnected in the final layout, and was terminated using a correlation strategy between HFSS and ADS simulation softwares.

For the future works, we can find some research opportunities to extend this thesis. More investigations on the presented schematics are recommended whether they can be expanded and applied to higher order dual-band filters. Another interesting research field is design of switchable dual-band bandpass filter . Also, some research works are recommended intensively whether the structure of proposed schematics can be re-designed for tunable filtering applications with two independently passband frequencies. The performance of lumped-elements networks are limited by SRF and low Q-factor at higher frequencies. Exploring possible techniques to increase SRF values and Q-factor of lumed-element components can be considered as one interesting research area.

BIBLIOGRAPHY

Avrillon, S., Pele, I., Chousseaud, A. & Toutain, S. (2003). Dual-band power divider based on semiloop stepped-impedance resonators. *IEEE Transactions on Microwave Theory and Techniques*, 51(4), 1269–1273.

Brzezina, G. & Roy, L. (2014). Miniaturized 180°Hybrid Coupler in LTCC for L-Band Applications. *IEEE Microwave and Wireless Components Letters*, 24(5), 336-338.

Brzezina, G., Roy, L. & MacEachern, L. (2009). Design enhancement of miniature lumped-element LTCC bandpass filters. *IEEE Transactions on Microwave Theory and Techniques*, 57, 815-823.

Brzezina, G. & Roy, L. (2014). Miniaturized, Lumped-Element Filters for Customized System-on-Package L-Band Receivers. *IEEE Transactions on Components, Packaging and Manufacturing Technology*, 4(1), 26–36.

Brzezina,G., R. L. M. L. (2009). Design Enhancement of Miniature Lumped-Element LTCC Bandpass Filters. *IEEE Transactions on Microwave Theory and Techniques*, 57(4), 815-823.

Cao, H., Yi, M., Chen, H., Liu, J., Liang, J. & Cai, W. (2014, Dec). Design of an ultra-compact dual-band bandpass filter with CRLH resonator. *2014 International Symposium on Antennas and Propagation Conference Proceedings*, pp. 53-54.

Chen, B. J., Shen, T. M. & Wu, R. B. (2009). Dual-Band Vertically Stacked Laminated Waveguide Filter Design in LTCC Technology. *IEEE Transactions on Microwave Theory and Techniques*, 57(6), 1554-1562.

Chen, C. C. (2005). Dual-band bandpass filter using coupled resonator pairs. *IEEE Microwave and wireless components letters*, 15, 259-261.

Chen, J. X., Zhan, Y. & Xue, Q. (2015). Novel LTCC distributed-element wideband bandpass filter based on the dual-mode stepped-impedance resonator. *IEEE Transactions on Components, Packaging and Manufacturing Technology*, 5, 372-380.

Chetouah, F., Bouzit, N., Messaoudene, I., Aidel, S., Belazzoug, M. & Hammache, B. (2016, Nov). Miniaturized rectangular dielectric resonator antenna for WCS standards. *2016 12th International Conference on Innovations in Information Technology (IIT)*, pp. 1-4.

Chin, K., Hung, J., Huang, C., Fu, J., Chen, B. & Chen, T. (2010). LTCC dual-band stepped-impedance-stub filter constructed with vertically folded structure. *Electronics Letters*, 46(23), 1554.

Choi, B. G., Stubbs, M. G. & Park, C. S. (2003). A Ka-band narrow bandpass filter using LTCC technology. *IEEE Microwave and Wireless Components Letters*, 13(9), 388-389.

Chu, H., Guo, Y. & Shi, X. (2011). 60 GHz LTCC 3D cavity bandpass filter with two finite transmission zeros. *Electronics Letters*, 47, 324-326.

Dai, X., Zhang, X. Y., Kao, H. L., Wei, B. H., Xu, J. X. & Li, X. (2014). LTCC bandpass filter with wide stopband based on electric and magnetic coupling cancellation. *IEEE Transactions on Components, Packaging and Manufacturing Technology*, 4, 1705-1713.

Dai, X., Zhang, X. Y. & Cai, Z. Y. (2013, July). Compact LTCC dual-band bandpass filter using stepped impedance resonators. *2013 Cross Strait Quad-Regional Radio Science and Wireless Technology Conference*, pp. 109-112.

Dancila,D., R. X. T. H. A. C. D. W. & Huynen, I. (2011). 57-64 GHz seven-pole bandpass filter Substrate Integrated Waveguide (SIW) in LTCC. *2011 IEEE MTT-S International Microwave Workshop Series on Millimeter Wave Integration Technologies*, pp. 200–203.

Deng, J., Wang, B. Z. & Gan, T. (2005, July). A compact narrow bandpass filter using LTCC technology. *2005 IEEE Antennas and Propagation Society International Symposium*, 1B, 602-605 vol. 1B.

Feng, W., Gao, X., Che, W., Yang, W. & Xue, Q. (2017). LTCC Wideband Bandpass Filters With High Performance Using Coupled Lines With Open/Shorted Stubs. *IEEE Transactions on Components, Packaging and Manufacturing Technology*, 7(4), 602-609.

He, Z., Shao, Z., You, C. J., Jiang, D. & Li, X. (2014). Design of planar narrow band millimetre-wave filter with wide stop-band. *Communication Problem-Solving (ICCP)*, pp. 672-674.

Hong, J. S. G. & Lancaster, M. J. (2004). *Microstrip filters for RF/microwave applications*. SJohn Wiley & Sons.

Hosseini, S. E., Attari, A. R. & Pourzadi, A. (2013). A Multiband PIFA with a Slot on the Ground Plane for Wireless Applications. *International Journal of Information and Electronics Engineering*, 3, 349.

Imanaka, Y. (2005). *Multilayered low temperature cofired ceramics LTCC technology*. Springer Science & Business Media.

Jia Sheng Hong,Lancaster, M. (1996). Couplings of microstrip square open-loop resonators for cross-coupled planar microwave filters. *IEEE Transactions on Microwave Theory and Techniques*, 44(11), 2099–2109.

Joshi, H. & Chappell, W. J. (2006). Dual-Band Lumped-Element Bandpass Filter. *IEEE Transactions on Microwave Theory and Techniques*, 54(12), 4169–4177.

Kapitanova, P., Kholodnyak, D., Humbla, S., Perrone, R., Mueller, J., Hein, M. A. & Vendik, I. (2009). Right- and left-handed transmission line resonators and filters for dual-band applications. *Microwave and Optical Technology Letters*, 51(3), 629-633.

Kim, H. T., Min, B. C., Choi, Y. H., Moon, S. H., Lee, S. M., Oh, B., Lee, J. T., Park, I. & Shin, C. C. (1999). A compact narrowband HTS microstrip filter for PCS applications. *IEEE Transactions on Applied Superconductivity*, 9(2), 3909-3912.

Lee, J., Lee, T. C. & Chappell, W. J. (2012). Lumped-Element Realization of Absorptive Bandstop Filter With Anomalously High Spectral Isolation. *IEEE Transactions on Microwave Theory and Techniques*, 60(8), 2424-2430.

Li, C., Zhang, Q., Meng, Q., Sun, L., Huang, J. & Wang, Y. (2006). et al., "A high-performance ultra-narrow bandpass HTS filter and its application in a wind-profiler radar system," Superconductor Science and Technology, vol. 19, p. *S*, 398.

Lin, K. C., Chang, C. F., Wu, M. C. & Jong, C. S. (2006). Dual-bandpass filters with serial configuration using LTCC technology. *IEEE Transactions on Microwave Theory and Techniques*, 54(6), 2321–2328.

Lin, Y. C., Horng, T. S. & Huang, H. H. (2014). Synthesizing a Multiband LTCC Bandpass Filter With Specified Transmission- and Reflection-Zero Frequencies. *IEEE Transactions on Microwave Theory and Techniques*, 62(12), 3351–3361.

Liu, S., Xu, J. & Xu, Z. T. (2016). Compact dual-band bandpass filters using complementary split-ring resonators with closely spaced passbands. *Electronics Letters*, 52, 1312-1314.

Liu, X., Katehi, L. P. B. & Peroulis, D. (2010). Novel Dual-Band Microwave Filter Using Dual-Capacitively-Loaded Cavity Resonators. *IEEE Microwave and Wireless Components Letters*, 20(11), 610–612.

Liu, Y., Chen, Y., Miao, X., Cui, C. & Tang, Y. (2015). Synthesis method of lumped dual-band filters with controllable bandwidths. *International Journal of RF and Microwave Computer-Aided Engineering*, 25(1), 75-80.

Lorente, J. A., Ernst, C. & Melcon, A. A. (2013). Rigorous derivation of lossy equivalent circuit for narrowband waveguide direct-coupled-cavity filters. *IET Microwaves, Antennas & Propagation*, 7, 251-258.

Matthaei, G. L. (1980). Microwave filters. *Impedance-Marching Networks, and Coupling Structure*, 4.

Miyake, H., Kitazawa, S., Ishizaki, T., Yamada, T. & Nagatomi, Y. (1997). A miniaturized monolithic dual band filter using ceramic lamination technique for dual mode portable telephones. *1997 IEEE MTT-S International Microwave Symposium Digest*, 2, 789-792.

Mousavi, S. H. & Kouki, A. B. (2015). High-SRF VHF/UHF Lumped Elements in LTCC. *IEEE Microwave and Wireless Components Letters*, 25, 25-27.

Mousavi, S. H. & Kouki, A. B. (2014, jun). A highly compact VHF/UHF dual-band LTCC coupler for avionic systems. *2014 IEEE MTT-S International Microwave Symposium (IMS2014)*, pp. 1–4.

Oshima, S., Wada, K., Murata, R. & Shimakata, Y. (2010). Multilayer Dual-Band Bandpass Filter in Low-Temperature Co-Fired Ceramic Substrate for Ultra-Wideband Applications. *IEEE Transactions on Microwave Theory and Techniques*, 58(3), 614–623.

Pourzadi, A., Attari, A. R. & Majedi, M. S. (2012). A Directivity-Enhanced Directional Coupler Using Epsilon Negative Transmission Line. *IEEE Transactions on Microwave Theory and Techniques*, 60(11), 3395-3402.

Pourzadi, A., Isapour, A. & Kouki, A. (2019). Design of Compact Dual-Band LTCC Second-Order Chebyshev Bandpass Filters Using a Direct Synthesis Approach. *IEEE Transactions on Microwave Theory and Techniques*, 67(4), 1441-1451.

Rezaee, M. & Attari, A. R. (2014, oct). A novel dual mode dual band SIW filter. *2014 44th European Microwave Conference*, pp. 853–856.

Schindler, M. J. & Tajima, Y. (1989). A novel MMIC active filter with lumped and transversal elements. *IEEE Transactions on Microwave Theory and Techniques*, 37(12), 2148-2153.

Shafique, M. F. & Robertson, I. D. (2011). Laser prototyping of multilayer LTCC microwave components for system-in-package applications. *IET Microwaves, Antennas Propagation*, 5(8), 864-869.

Shao, J. Y. & Lin, Y. S. (2015). Narrowband coupled-line bandstop filter with absorptive stopband. *IEEE Transactions on Microwave Theory and Techniques*, 63, 3469-3478.

Shen, T., Chen, C., Huang, T. & Wu, R. (2009, Dec). Design of lumped rat-race coupler in multilayer LTCC. *2009 Asia Pacific Microwave Conference*, pp. 2120-2123. doi: 10.1109/APMC.2009.5385258.

Shen, W., Yin, W., Sun, X. & Wu, L. (2013). Substrate-Integrated Waveguide Bandpass Filters With Planar Resonators for System-on-Package. *IEEE Transactions on Components, Packaging and Manufacturing Technology*, 3(2), 253-261.

Su, L. & Tzuang, C. K. C. (2012). A narrowband CMOS ring resonator dual-mode active bandpass filter with edge periphery of 2% free-space wavelength. *IEEE Transactions on Microwave Theory and Techniques*, 60, 1605-1616.

TAMURA, M., ISHIZAKI, T., HASHEMI, M. R. M. & ITOH, T. (2010). Approach of Metamaterial-Based Quarter-Wave Resonator and Its Application to Very Compact LTCC Bandpass Filter. *IEICE Transactions on Electronics*, E93.C(7), 1078-1088.

Tamura, M., Yang, T. & Itoh, T. (2011). Very Compact and Low-Profile LTCC Unbalanced-to-Balanced Filters With Hybrid Resonators. *IEEE Transactions on Microwave Theory and Techniques*, 59(8), 1925-1936.

Tang, C. W. & You, S. F. (2006). Using the technology of low temperature co-fired ceramic to design the dual-band bandpass filter. *IEEE Microwave and Wireless Components Letters*, 16(7), 407-409.

Tang, C. W., You, S. F. & Liu, C. (2006). Design of a dual-band bandpass filter with low-temperature co-fired ceramic technology. *IEEE Transactions on Microwave Theory and Techniques*, 54(8), 3327-3332.

Tang, C. (2007). Development of LTCC bandpass filters with transmission zeros. *Electronics Letters*, 43(21), 1149-1150.

Turgaliev, V., Kholodnyak, D. & Vendik, I. (2013). Small-size dual-band filters on capacitively loaded cavities. *2013 European Microwave Conference*, pp. 660-663.

V. Turgaliev,D. Kholodnyak, J. M. & Hein, M. (2015). Small-size low-loss bandpass filters on substrate-integrated waveguide capacitively loaded cavities embedded in low temperature co-fired ceramics. *Journal of Ceramic Science and Technology*, 6(4), 305-314.

Wang, J., Xu, X. & Zhang, G. (2013). 60 GHz dual-band bandpass filter using LTCC. *Electronics Letters*, 49(16), 1001–1002.

Xu, J., Wu, W. & Wei, G. (2016a). Novel dual-band bandpass filter and reconfigurable filters using lumped-element dual-resonance resonators. *IEEE Transactions on Microwave Theory and Techniques*, 64, 1496-1507.

Xu, J. X., Zhang, X. Y., Zhao, X. L. & Xue, Q. (2016b). Synthesis and implementation of LTCC bandpass filter with harmonic suppression. *IEEE Transactions on Components, Packaging and Manufacturing Technology*, 6, 596-604.

Xu, J., Wu, W. & Wei, G. (2016c). Novel Dual-Band Bandpass Filter and Reconfigurable Filters Using Lumped-Element Dual-Resonance Resonators. *IEEE Transactions on Microwave Theory and Techniques*, 64(5), 1496–1507.

Xu, X., Wang, J. & Zhang, G. (2013). 60 GHz dual-band bandpass filter using LTCC. *Electronics Letters*, 49, 1001-1002.

Yang, T., Tamura, M. & Itoh, T. (2010). Super Compact Low-Temperature Co-Fired Ceramic Bandpass Filters Using the Hybrid Resonator. *IEEE Transactions on Microwave Theory and Techniques*, 58(11), 2896–2907.

Yatsenko, A., Orlenko, D., Sakhnenko, S., Sevskiy, G. & Heide, P. (2007). A Small-Size High-Rejection LTCC Diplexer for WLAN Applications Based on a New Dual-Band Bandpass Filter. *2007 IEEE/MTT-S International Microwave Symposium*, pp. 2113-2116.

Yeung, L. K. & Wu, K. L. (2003). A compact second-order LTCC bandpass filter with two finite transmission zeros. *IEEE Transactions on Microwave Theory and Techniques*, 51(2), 337-341.

Zhang, X. Y., Dai, X., Kao, H. L., Wei, B. H., Cai, Z. Y. & Xue, Q. (2014). Compact LTCC bandpass filter with wide stopband using discriminating coupling. *IEEE Transactions on Components, Packaging and Manufacturing Technology*, 4, 656-663.

Zheng, S. Y., Yongle Wu,Yuanxin Li, Y. L. & Long, Y. (2014). Dual-Band Hybrid Coupler With Arbitrary Power Division Ratios Over the Two Bands. *IEEE Transactions on Components, Packaging and Manufacturing Technology*, 4(8), 1347–1358.

Zheng, Y. & Sheng, W. (2017). Compact Lumped-Element LTCC Bandpass Filter for Low-Loss VHF-Band Applications. *IEEE Microwave and Wireless Components Letters*, 27(12), 1074-1076.

Zhou, B., Cheng, C., Yan, L., Zhou, N., Cao, Y., Tang, Q., Li, Q., Ma, Q., Song, Z., Li, S., Wang, Z. & Hu, S. (2016, Oct). Miniaturized lumped-element LTCC quadrature hybrid with harmonics suppression. *2016 IEEE International Conference on Ubiquitous Wireless Broadband (ICUWB)*, pp. 1-3.

Zhou, C., Guo, Y., Yan, S. & Wang, Z. (2011). Dual-band UWB filter with LTCC technology. *Electronics Letters*, 47(22), 1230.

Zhou, K., Zhou, C. & Wu, W. (2018). Substrate-Integrated Waveguide Dual-Band Filters With Closely Spaced Passbands and Flexibly Allocated Bandwidths. *IEEE Transactions on Components, Packaging and Manufacturing Technology*, 8(3), 465-472.

Zhu, H. & Abbosh, A. M. (2016). Single- and Dual-Band Bandpass Filters Using Coupled Stepped-Impedance Resonators With Embedded Coupled-Lines. *IEEE Microwave and Wireless Components Letters*, 26(9), 675-677.